Dissertation

submitted to the
Combined Faculties for the Natural Sciences and for Mathematics
of the Ruperto-Carola University of Heidelberg, Germany
for the degree of
Doctor of Natural Sciences

presented by

Diplom-Physicist Gerhard Mühlbauer
born in Furth im Wald

Oral examination: 29th October 2003

Stellar Dynamics in the Outer Galactic Disk under the Influence of a Central Bar

Referees: Prof. Dr. Hans-Walter Rix
Prof. Dr. Roland Wielen

Abstract

In this work, we investigate the possible influence of a central bar in a disk galaxy on the velocity distribution in the outer stellar disk, which is thought to arise mostly via resonant phenomena. For this, we numerically integrate orbits of a large number of sample points in a 2D model potential consisting of a rotating bar component in an axisymmetric background. Central to our analysis is the construction of the first and second moments of the velocity distribution in their spatial variability. From these, other important quantities like Oort constants, dispersion axis ratio and vertex deviation can be deduced. For the latter, we predict non-vanishing values for a large number of kinematical configurations. Regarding the axis ratio, we are able to obtain values smaller than $1/2$, in agreement with observations in the solar neighbourhood which are hitherto unexplained by theory. All our results are consistent with a proposed position of the Sun lying shortly outside of the co-rotation radius and lagging behind the bar by $\sim 30°$.

We repeat part of our analysis for model potentials including spiral structure, in order to estimate how much our results will be affected by this. It turns out that in many cases our bar-induced features continue to prevail, whereas the extent of the spiral effects is seen to depend particularly on pitch angle, which for the case of the Milky Way is very poorly constrained.

Zusammenfassung

In dieser Arbeit wird der mögliche Einfluß eines zentralen Balkens einer Scheibengalaxie auf die Geschwindigkeitsverteilung der Sterne in den äußeren Bereichen der Scheibe untersucht, wie er insbesondere durch Resonanzphänomene zustande kommen sollte. Dazu führen wir numerische Orbit-Integrationen einer großen Zahl von Testteilchen in einem zweidimensionalen Potentialmodell durch, das aus einer rotierenden Balkenkomponente und einem axialsymmetrischen Hintergrundpotential besteht. Mittelpunkt unserer Analyse ist die Konstruktion der ersten und zweiten Momente der Geschwindigkeitsverteilung in ihrer örtlichen Abhängigkeit. Daraus können andere wichtige Größen wie die Oort-Konstanten, das Achsenverhältnis der Geschwindigkeitsdispersion und die Vertex-Deviation bestimmt werden. Für die letztere ergeben sich in einer Vielzahl von kinematischen Konfigurationen nichtverschwindende Werte. Bezüglich des Dispersions-Achsenverhältnisses können wir in geeigneten Fällen auch Werte kleiner als $1/2$ erhalten, wie sie aus Beobachtungen in der Sonnenumgebung erschlossen wurden, bisher aber von der Theorie nicht erklärt werden können. Unsere Ergebnisse sind stets verträglich mit der vermuteten relativen Lage der Sonne zum Balken, dass diese nämlich sich knapp außerhalb des Korotationsradius befinde und etwa $30°$ hinter dem Balken her laufe.

Teile unserer Untersuchungen werden wiederholt für Potentialmodelle, die auch ein Spiralmuster einschließen, um eine Einschätzung dafür zu gewinnen, wie weit unsere Ergebnisse davon modifiziert werden. Es zeigt sich, dass zwar in vielen Fällen die von uns gefundenen Balken-Effekte vorherrschend bleiben, dass aber die Auswirkungen des Spiralpotentials vor allem von dessen Anstellwinkel abhängen. Dieser ist im Falle der Milchstraße nur sehr ungenau bekannt.

Man weiß eigentlich nur, wenn man wenig weiß; so wie man mehr erfährt, stellt sich nach und nach der Zweifel ein.

J. W. v. Goethe

Contents

Chapter 1

Introduction

Reconstructing the shape of the Milky Way is a difficult task. This is due to our unique point of view on this galaxy: sitting right in the middle, we see a lot of local detail and can make observations which will never be possible for external galaxies. But we cannot easily get a view of the big picture. In particular, our sight is hampered by dust obscuration, and we are confronted with the crucial problem of distance determination.

There are two possible ways to overcome this difficulty: one is to turn to such observational options which allow a wider view nonetheless, e.g. the infrared. The other possibility is to try to draw conclusions on the global structure from local observations. Stellar kinematics seems to be especially useful in this respect, since the collisionless nature of stellar dynamics ensures that it is dominated by large-scale properties.

In the last decades, there has been major progress on either side. A large part of this progress is due to the advances in infrared astronomy, which allows to look into the dust-obscured central parts of the Milky Way. Especially the DIRBE experiment on board the COBE satellite produced extensive sky maps in the near and far infrared which can be used for modelling Galactic structure. IR surveys like the recently completed 2MASS will allow further investigations of this kind.

On the other hand, determining the local stellar kinematics means measuring positions and spatial velocities of large numbers of stars. Up to now, this has only been possible in the near vicinity of the Sun. The greatest progress in this field has been brought about by the HIPPARCOS mission. This astrometric satellite was flown from 1989 to 1993, data were published till 1997. Amongst a plethora of other things, it allowed for the first time a reconstruction of the stellar velocity distribution in the solar neighbourhood. These data allow conclusions on Galactic structure already today. However, a golden era for Galactic structure studies will be opened up with the GAIA mission, which will measure positions and velocities of around one billion stars, or about 1% of the Galactic stellar population. However, we have to wait at least until the year 2020, when the GAIA data become available.

One important mechanism of how global Galactic properties might be traceable in local kinematics is through orbital resonances. Orbital resonances have been seen to be of relevance in a variety of topics, from solar system studies and planetary disks to the kinematics ot galactic disks. We will argue that they also play a decisive role in the solar neighbourhood.

Deviations from axisymmetry, and in particular a central bar, are the Galactic features which interest us most. The existence of a bar in the Milky Way is largely established today, and bars are generally considered to constitute a major component of a galaxy's mass distribution, so they could easily have kinematical influences, especially if we think of orbital resonances again. Thus, the central questions at the beginning of this thesis were the following: Can the presence ot the bar of the Milky Way be felt in the solar neighbourhood? Does it influence the kinematics of the outer stellar disk? What form does this influence take? What constraints on the global bar properties can be drawn from the measurement of local velocity distributions? The idea was to approach this questions by theoretically modelling a galactic disk with a central bar, and to analyse the resulting velocity distributions.

Outline of the thesis

In section 2 we give an introduction to some of the relevant topics. After some words about disk galaxies in general and the Milky Way in particular, we shortly review the principles of stellar dynamics, where we put the emphasis already on kinematic influences of bar. We will touch on resonances and the theory of orbits in a rotating bar potential. Finally we review what is known about the local velocity field in the solar neighbourhood.

The central aim of the thesis is to investigate the extent to which a bar might influence the outer regions of a stellar disk. Section 3 is an adapted and slightly extended version of a paper published in A&A (Mühlbauer & Dehnen 2003 [66]). It describes the numerical simulations we have done using a two-dimensional model of a barred galaxy and analysing the velocity distribution in the outer disk via its angular moments.

Section 4 contains some further studies we did using our model, which did not find the way into a refereed paper. In particular, we take a short look at the asymmetric drift, we investigate in some detail the velocity dispersion ellipsoid axis ratio, and we look into what our model has to say about the Oort constants.

In this first set of simulations, we did not include any perturbation other than the bar. This is clearly a very rude approximation to reality, since the Galaxy obviously has a number of deviations from axisymmetry. We tried to extend our simulations to include some kind of spiral structure. This work is descibed in section 5.

Section 6 gives conclusions and outlook. In particular, we consider the capabilities of the future astrometric satellite mission GAIA on clarifying the kinematic state of the Galactic disk.

Chapter 2

Some General Aspects of Disk Galaxy Dynamics

2.1 Disk galaxies and the Milky Way

Since the time of Hubble, galaxies are classified according to the tuning-fork diagramm (Fig. 2.1). On the one hand, there are elliptical ("early-type") galaxies, consisting of a more or less flattened spheroid and appearing as an ellipse on the sky. On the other hand ("late-type"), we have two series of disk galaxies, which consist of a flat disk surrounding a small spheroidal bulge. The disk always possesses spiral arms, though these may be of very different length and prominence. One distinguishes subtypes Sa, Sb and Sc, in which the spiral arm pattern is increasingly more tightly wound and the relative extension of the central bulge is decreasing.

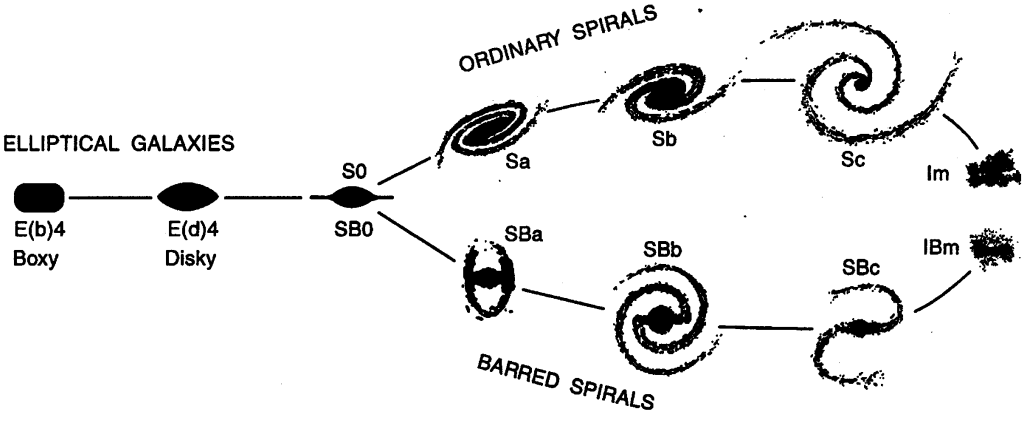

Figure 2.1: Classification of galaxies after E. P. Hubble

Some spiral galaxies exhibit a more or less rectangular-shaped central structure, which is called a bar. In Hubble's diagram, these form a second series of disks called SBa, SBb, SBc, thereby causing the tuning-fork form.

At the junction point of the tuning fork, there is a galaxy type called lenticular, denoted S0 or SB0. Finally, on the far end of the late-type side, there are irregular forms.

2.1.1 Structure of disk galaxies

The surface brightness of the disk component usually obeys an exponential law (Freeman 1970 [43])

$$\Sigma(R) \propto e^{-R/R_\Sigma} \tag{2.1}$$

with a scale length R_Σ in the range $\sim$ 3 kpc. The vertical structure likewise is most often described as an exponential, or more smoothly as $\propto$ sech(z/h). The scale-height h here usually is some hundred pc.

The exponential law (2.1) ceases to hold beyond about 3 – 4 scale lengths R_Σ, where most galactic disks seem to be truncated, i.e. their density drops rapidly (van der Kruit & Searle 1981/82 [94, 95]). This applies to the stellar component of the disk, the gas part may reach out farther, and often shows some warping in its outer parts.

Disk galaxies show a continuous and ongoing star formation, in contrast to ellipticals, where star formation concentrated in the early epochs of their history. Primary sites of this ongoing star formation are the spiral arms, where HII regions are located, and it is the blue light of young O- and B-stars which cause the prominent visibility of the spiral arms.

Apart from a section very close to the center, toward which it drops to zero, the rotation velocity v_c of galactic disks is usually more or less constant, so that the angular velocity ω falls as $1/R$. This indicates a homogeneous mass distribution. It has come as a big surprise that rotation curves seem to be flat for the outer regions of galactic disks, too, since it implies that there is a large amount of mass surrounding the visible disk. This is one of the points which call for the existence of large amounts of dark matter in the universe, here suggesting that disk galaxies are embedded in large dark matter halos.

2.1.2 Bars in galaxies

Nearly every third spiral galaxy is conspicuously barred. The fraction of spirals with very small bars could be still higher, so that bars could be a very common phenomenon. For a review on barred galaxies see e.g. Sellwood & Wilkinson 1993 [87].

The question whether there are distinct bulge and bar components is unresolved (Kuijken 1996 [59]). Concerning the edge-on view of bars, it is unclear whether, as might be hypothesized, bars would correspond to particularly boxy bulges. It is possible that bars are flat as thin disks. At least, the percentage of edge-on disk galaxies showing no sign of central bulges is comparable to the percentage of face-on disks having a bar (Kormendy 1982 in [9])

Bars are confined to the inner regions of the galaxy. Studies based on stellar orbit theory suggest that bars end at or slightly inside their co-rotation radius (e.g. Contopoulos 1980 [18]), see section 2.2.4 for more on that. The bar length seems to depend on galaxy type, too: bars in late-type galaxies seem to be shorter relative to the total galaxy size than those in early-type galaxies (Athanassoula & Martinet 1980 [4]).

In studies of external galaxies (Gerssen et al. 2002 [49]) bars are seen to rotate fast, i.e. such that their co-rotation radius exceeds the bar size only slightly by some 20 – 30 %, resulting in rotation speeds in the range of ~ 50 km/s/kpc. On the other hand, simulations of cosmological structure formation suggest that galaxies have centrally concentrated dark matter halos, which should rapidly slow down bar rotation by dynamical friction (Debattista & Sellwood 1998 [24]; but see also Athanassoula 2003 [3]).

2.1.3 The Milky Way as a disk galaxy

The Milky Way seems to be of Hubble type Sbc, or SBbc, if we take its bar seriously. Its scale-length is not very well known. Preliminary data of the 2MASS survey (Ohja 2001 [70]) suggest a value of 2.8 ± 0.3 kpc, whereas a recent study of COBE infrared data (Drimmel & Spergel 2001 [34]), yields $0.28 R_\odot \sim 2.3$ kpc. The stellar disk seems to be truncated at about 10.5 kpc for $\Sigma(R)$ or 4 – 5 disk scale lengths R_Σ, which appears rather large compared to external galaxies where the truncation usually occurs at about 3 scale lengths (see also Dehnen 2002 [29]).

Apart from the usual stellar disk there is probably a so-called thick disk composed of old metal-poor stars with a higher vertical scale height and a stellar density of some percent of the thin disk's. Ohja 2001 obtained a vertical scale-height of 860 ± 200 pc for this. The idea of a distinct thick disk came up when star count studies toward the Galactic poles showed a space density fitted by a sum of two exponentials with two different scale heights (Gilmore and Reid 1983 [50]). The stars distributed with the larger scale height also seemed to be redder in colours, so there may indeed be two distinct galactic star populations. Further evidence for the thick disk came with the IRAS data in the mid infrared (Habing 1988 [52]). Different evolutionary scenarios for the two disks seem probable.

De Vaucouleur 1964 [22] was the first to postulate that the bulge of the Milky Way contains a triaxial structure or a bar, in order to explain the radial velocities of gas in the inner few kiloparsecs of the Galaxy, which radio astronomy has shown to be inconsistent with travelling on circular orbits. During the 1970s and 1980s, there have been some papers arguing in favor of the Milky Way as a barred galaxy (e.g. Peters 1975 [76]), but it was not before the work of Blitz & Spergel 1991 [12] that this idea gained momentum. Anticipating the COBE measurements of the infrared emission of the Galaxy, these authors used balloon observations at $2.4\ \mu$m done by Matsumoto et al. in 1982 to investigate the presence of a bar, for which they found clear hints.

Widespread availability of infrared data, first of all from the first extensive IR satellite mission IRAS, brought major progress. Weinberg 1992 [96] was able to see the bar directly in the distribution of IRAS Mira variables. The COBE mission, primarily designed to measure the cosmic microwave background, provided photometric images of the Galactic bulge region in the near infrared through its DIRBE instrument. Several authors (e.g. Dwek et al. 1995 [35], Freudenreich 1998 [44]) used these data to do fits of detailed models of Galactic structure including a bar component. Freudenreich concluded that the Milky Way disk has an inner hole slightly larger than the bar, which has probably been cleared out by the bar.

Further evidence for the Galactic bar comes from gravitational microlensing towards the Galactic bulge, where a higher than expected rate of microlensing events has been observed (e.g Paczynski et al. 1994 [74]). This can be explained by stars in the near part of the Galactic bar microlensing stars in the far side of the bar. A corresponding model has been given by Zhao, Spergel & Rich 1995 [98]. Stanek 1997 [90] used the photometric OGLE data to construct a model of the Galactic bar by the luminosity distribution of red clump stars.

The gas dynamics in the inner Galaxy has been modelled by Binney, Gerhard et al. 1991 [8], more recently by Englmaier & Gerhard 1999 [40], and compared to deprojections of IR data.

The Milky Way's bar is probably rotating fast, too. A direct measurement using OH/IR star tracers (Debattista et al. 2002 [23]) yields (59 ± 5) km/s/kpc. In an indirect manner, certain features of the local velocity distribution point to a high pattern speed of the bar via its resonant radii, cf. section 2.3.5.

From its content of IR C stars, Cole & Weinberg 2002 [17] infer a maximum age of the Galactic bar of 6 Gyr, most probable seems to be an age of less than 3 Gyr. These authors find that this star population is a reliable tracer of the bar, and therefore they might be related to a bar-triggered star formation event during bar formation. Whether this justifies the conclusion from individual stars to a collective dynamical feature will of course be a matter of debate.

The outer disk of the Milky Way seems to have a warp. Evidence for this is as old as the first HI-data for the southern hemisphere in the 1950's, and has been corroborated with modern HI-surveys. The warp starts somewhere around the solar circle, and the Sun happens to lie near one of its nodelines.

For the spiral structure of the Milky Way see section 5.1.2.

2.2 Stellar dynamics

Close encounters of individual stars are very rare and can be neglected, therefore stellar dynamics is governed by a collisionless Boltzmann equation ("Vlasov equation" in plasma physics). This is nothing else but the statement that the distribution function $f(\mathbf{r},\mathbf{v},t)$, being the mass or particle[1] density in the one-particle phase space composed of the space and velocity coordinates ($\mathbf{r}$ and $\mathbf{v}$, respectively), behaves as some kind of incompressible fluid. It can be formulated as follows:

$$\begin{aligned} 0 = \frac{df}{dt} &= \frac{\partial f}{\partial t} + \frac{d\mathbf{r}}{dt}\cdot\frac{\partial f}{\partial \mathbf{r}} + \frac{d\mathbf{v}}{dt}\cdot\frac{\partial f}{\partial \mathbf{v}} = \\ &= \frac{\partial f}{\partial t} + \mathbf{v}\cdot\frac{\partial f}{\partial \mathbf{r}} - \frac{\partial \Phi}{\partial \mathbf{r}}\cdot\frac{\partial f}{\partial \mathbf{v}} \end{aligned} \tag{2.2}$$

The corresponding equations for the zeroth and first velocity moments of the distribution function are known as Jeans equations, and are central to stellar dynamics. As implied by their nature, they are obtained by integrating the collisionless Boltzmann equation over velocity space, after an additional multiplication by $\mathbf{v}$ in the appropriate case:

$$0 = \frac{\partial \rho}{\partial t} + \sum_i \frac{\partial(\rho\,\bar{v}_i)}{\partial x_i}, \tag{2.3}$$

$$0 = \frac{\partial(\rho\,\bar{v}_j)}{\partial t} + \sum_i \frac{\partial(\rho\,\overline{v_i v_j})}{\partial x_i} + \rho\frac{\partial \Phi}{\partial x_j}, \tag{2.4}$$

where $\rho = \int f d^3v$ is the spatial density and $\rho\,\bar{v}_i = \int f v_i\, d^3v$, $\rho\,\overline{v_i v_j} = \int f v_i v_j\, d^3v$ are the first and second moments of f. Using

$$\sigma_{ij}^2 := \overline{(v_i - \bar{v}_i)(v_j - \bar{v}_j)} = \overline{v_i v_j} - \bar{v}_i\,\bar{v}_j \tag{2.5}$$

we can rewrite (2.4) as

$$\rho\frac{\partial \bar{v}_j}{\partial t} + \sum_i \rho\bar{v}_i\frac{\partial \bar{v}_j}{\partial x_i} = -\rho\frac{\partial \Phi}{\partial x_j} - \sum_i \frac{\partial(\rho\sigma_{ij}^2)}{\partial x_i}, \tag{2.6}$$

which makes the analogy to the Euler equations of hydrodynamics obvious and shows that $\rho\sigma_{ij}^2$ is a stress tensor corresponding to an anisotropic pressure.

With the help of the Jeans equations it can be shown that any steady-state solution of the collisionless Boltzmann equation can depend on phase-space coordinates only through integrals of the motion. Conversely, any function of the integrals of motion constitutes such a steady-state solution. This is called Jeans theorem.

---

[1] As common in stellar dynamics, we will consider a single kind of particle having unit mass. Thus, we will not distinguish between mass and particle density.

Integrals of motion constrain the motion to certain hypersurfaces in phase space, and the number of the integrals of motion a given orbit observes is decisive for its regular or chaotic character. We will not go into this kind of questions here. Suffice it to say that most potentials allow for chaotic regions of phase space.

2.2.1 Motion in axisymmetric potentials and the epicycle approximation

In axisymmetric potentials we always have at least two integrals of motion: the energy E and the z-component of angular momentum L.

We know that in these potentials circular orbits will always be a solution, and we can express the orbital speed and the corresponding angular velocity of these orbits directly in terms of the potential[2]:

$$v_c^2(R) = R\frac{\partial \Phi}{\partial R}, \qquad \omega^2(R) = \frac{1}{R}\frac{\partial \Phi}{\partial R} \tag{2.7}$$

Clearly, the angular momentum of such orbits is $L = Rv_c(R)$.

The fact that energy E and angular momentum L are integrals of the motion can be used for reducing the problem to the motion of a fictitious particle in only two coordinates R and z. For this, write the energy in the form $E = 1/2(\dot{R}^2 + \dot{z}^2) + \Phi_{\text{eff}}(R, z)$ with an effective potential

$$\Phi_{\text{eff}}(R, z) = \Phi(R, z) + \frac{L^2}{2R^2} \tag{2.8}$$

Having this fictitious particle at rest in a potential minimum at some radius R_g corresponds to a circular motion of the real particle with angular velocity $\omega = \dot{\varphi} = L/R_g^2$.

Galactic orbits are quite often nearly circular, so they can be approximated by small oscillations of the fictitious particle around its potential minimum. This is the epicycle approximation. If we do a Taylor expansion of Φ_{eff} around its minimum (details can readily be found e.g. in Binney & Tremaine 1987 [11]), we usually get harmonic oscillator equations for the deviations, with frequencies

$$\kappa^2 := \left.\frac{\partial^2 \Phi_{\text{eff}}}{\partial R^2}\right|_{R_g}, \qquad \nu^2 := \left.\frac{\partial^2 \Phi_{\text{eff}}}{\partial z^2}\right|_{R_g}, \tag{2.9}$$

which we call the epicycle and vertical frequency, respectively. By (2.7), the first one can also be written as

$$\kappa^2 = \left.\left(R\frac{\partial \omega^2}{\partial R} + 4\omega^2\right)\right|_{R_g} \tag{2.10}$$

In the tangential direction, the motion is likewise an oscillation at the same frequency κ, because of $\dot{\varphi} = L/R^2$. Therefore, if the vertical oscillation is not excited, the real particle performs a closed elliptic motion around its guiding center at R_g, which itself is rotating uniformly at the circular velocity ω. If X and Y denote the semimajor axes of the epicycle ellipse in the radial and tangential direction, respectively, the axis ratio of the ellipse is

$$\frac{Y}{X} = \frac{2\omega}{\kappa} =: \gamma, \tag{2.11}$$

as can be seen by expanding $\dot{\varphi} = L/R^2$ around R_g.

---

[2] For a circular orbit we have clearly $\mathbf{r} \cdot \mathbf{v} = 0$ and therefore $0 = d(\mathbf{r} \cdot \mathbf{v})/dt = d\mathbf{r}/dt \cdot \mathbf{v} + \mathbf{r} \cdot d\mathbf{v}/dt = v^2 - \mathbf{r} \cdot \nabla\Phi = v^2 - R\,\partial\Phi/\partial R$.

Note that from (2.10), a flat rotation curve corresponds to $\kappa = \sqrt{2}\omega$, a Keplerian falloff to $\kappa = \omega$ and a solid body rotation to $\kappa = 2\omega$. Since Keplerian and solid body behaviour constitute some kind of limiting cases, we will have $\omega \lesssim \kappa \lesssim 2\omega$, and the epicycle ellipse will always be elongated in the tangential direction.

An equivalent characterization of the epicycle approximation is to say that the energy of the vertical motion has been taken as a third integral (see e.g. Dehnen & Binney 1996 [30]). This corresponds to assuming a discoupling of the vertical motion from that in the disk.

2.2.2 Motion in rotating non-axisymmetric potentials

Consider a potential rotating at a certain angular velocity Ω_P ("pattern speed"). In this case, Energy E and angular momentum $\mathbf{L}$ are not conserved. There is, however, a conserved quantity which expresses the fact that the potential is time-independent in a frame rotating at the same angular speed (see appendix A for a formal treatment of the problem). This is the so-called Jacobi integral:

$$E_J = E - \boldsymbol{\Omega}_p \cdot \mathbf{L}, \tag{2.12}$$

where $\boldsymbol{\Omega}_p = (0, 0, \Omega_p)$ is the vectorial pattern speed. Except for the Coriolis force, which is not accounted for, we can use this quantity analogously to the energy to discuss the problem in terms of an effective potential, which in this case is the true potential plus a term representing the centrifugal force:

$$\Phi_{\text{eff}} = \Phi - \frac{1}{2}(\boldsymbol{\Omega}_p \times \mathbf{r})^2 = \Phi - \frac{1}{2}\Omega_p^2 R^2, \tag{2.13}$$

so that Jacobi's integral can be written as (see appendix A for derivation)

$$E_J = \frac{1}{2}|\dot{\mathbf{r}}|^2 + \Phi_{\text{eff}}, \tag{2.14}$$

where $\dot{\mathbf{r}}$ is the velocity in the rotating frame.

Extremal points of the effective potential (see Fig. 2.2) are called Lagrangian points in analogy to similar points in the theory of the restricted three-body problem. Particles located exactly at these points would describe a circular orbit co-rotating with the bar. The saddle points L1 and L2, however, are generically unstable, i.e. small deviations from this equilibrium position will amplify. The minimum L3 at the center is always stable, and stability conditions of the maximum points L4 and L5 depend on the details of the mass distribution. However, in a lot of cases they are indeed stable, especially if the bar is not too strong (see Pfenniger 1990 [77] for a detailed discussion), and there are families of orbits oscillating around these.

Because of (2.14) and the fact that the Jacobi integral is a constant of the motion, we can use Φ_{eff} to put restrictions on the movement of particles, cf. Fig. 2.3. Orbits can never enter the region below the solid red line in this figure. They can, however, at suitable angles get below the dashed green line. Stars with E_J greater than $\Phi_{\text{eff}}(\text{L4/L5})$ (dotted green line in the figure) are free to explore the entire space (though they are often effectively confined by the Coriolis force) and are said to belong to the hot regime. Stars with E_J smaller than $\Phi_{\text{eff}}(\text{L1/L2})$ (dotted red line) can never pass the radius corresponding to L1/L2, and are confined to the region outside or inside of this. Stars with $\Phi_{\text{eff}}(\text{L4/L5}) > E_J > \Phi_{\text{eff}}(\text{L1/L2})$ form an intermediate regime in which the accessible radii depend on the angle.

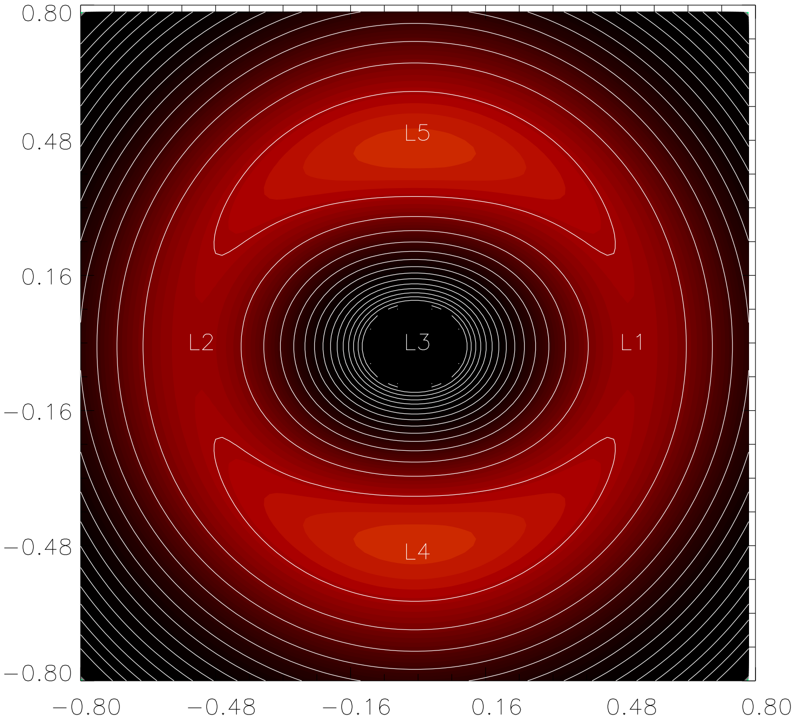

Figure 2.2: Contour plot of an effective bar potential Φ_{eff} in the co-rotating frame, resulting in the typical “vulcano”-shape. The plot uses the potential defined in section 3.1. The Lagrangian points are indicated, there are maxima (L4 and L5), a minimum (L3) and saddle points (L1 and L2).

2.2.3 Kinematic effects of bars: resonances

If the difference $\omega(R) - \Omega_b$ of the angular velocity of circular trajectories and the rotation velocity of the bar is in some small-number ratio to its epicycle frequency $\kappa(R)$, we have a resonance. Stars on such orbits will regularly be found in identical configurations relative to the bar, so that small influences will accumulate over time. A special resonance is co-rotation, where the two angular speeds are equal. The resonance condition is usually written as

$$\Omega_b = \omega(R) - \frac{n}{m}\kappa(R). \tag{2.15}$$

The same condition for the vertical frequency $\nu(R)$ gives the vertical resonances, but these are thought to be less important than the radial ones.

Since the resonance condition makes reference to circular velocities and epicycle frequencies, the entire concept is always related to the linear regime, where the epicycle approximation or some analogue is valid. In this sense, every resonance corresponds to a certain radius where (2.15) is fulfilled.

When viewed in the frame co-rotating with the bar, the resonance condition means that the corresponding epicylce orbit is closed. A particle will have completed m cycles of its radial oscillation while having circled n times around the center. Since in the outer regions of the Galaxy $\omega(R)$ will always be a decreasing function of R, orbits further out than co-rotation will appear retrograde in the

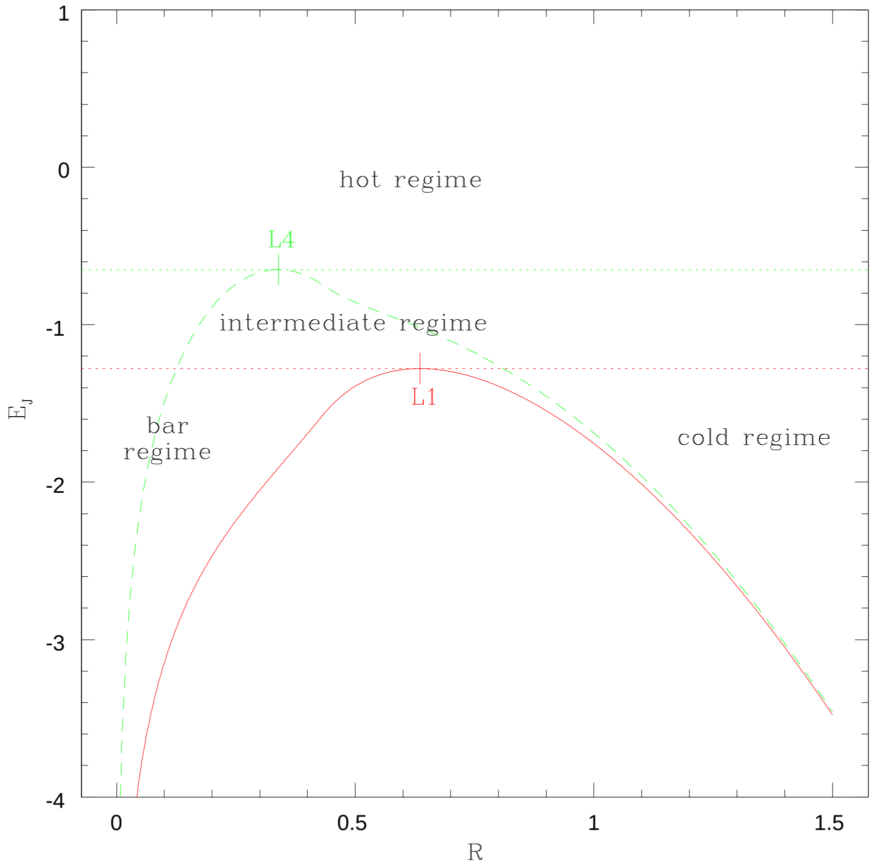

Figure 2.3: The effective potential (2.13) divides the (R, E_J)-plane in different regimes. The solid (red) and dashed (green) lines show Φ_{eff} along the long and short axis of the bar, respectively.

co-rotating frame. Most resonances come in pairs, with one prograde member inside co-rotation, and one retrograde outside. These pairs correspond to positive or negative sign of n.

A bar potential has a multipole order of 2, and therefore the $m = 2$ resonances are supposedly the most significant. They are called Lindblad resonances, after the Swedish astronomer Bertil Lindblad (1895 - 1965). Table 2.1 gives an overview over the most important resonances.

The inner Lindblad resonance is a special case, because it can itself be double. Whether we have one or two ILRs depends on the exact form of the rotation curve in the inner region. With a strong central concentration or a large point mass in the center, the rotation curve might increase monotonically with decreasing radius. In this case, there is always exactly one ILR. If, however, the central concentration is less strong, the angular velocity curve will tend towards a constant value, which by (2.10) implies $\kappa = 2\omega$ and accordingly $\omega - 1/2\kappa$ goes to zero towards the center, so that there is a maximum in it (cf. Fig. 2.4). There will then be either two ILRs or none at all, depending on whether the pattern speed of the bar is larger or less than the maximum of the curve. If it is nearly equal to this maximum value, there will be a region with “near resonance” effects.

n	m	name
0		Co-rotation CR
-1	2	Outer Lindblad resonance OLR
1	2	Inner Lindblad resonance ILR if two-fold: inner (IILR) and outer ILR (OILR)
-1	1	Outer 1:1 resonance
±1	4	Ultraharmonic resonances UHR

Table 2.1: Bar resonances

2.2.4 Stellar orbits in barred potentials

Most helpful in the study of kinematics in an arbitrary potential are periodic orbits. These can be stable or unstable, depending on whether small deviations induce a backward driving force or tend to amplify. In the stable case, there will be a family of non-periodic orbits oscillating around the periodic one. The circular orbits of epicycle theory in an axisymmetric potential are stable, for example, and the epicycle orbits are the non-periodic family. On the other hand, unstable periodic orbits indicate borderlines of regions in phase space occupied by these families. So knowledge of the periodic orbits in a given potential provides a classification scheme for orbits, although it must always be remembered that there are also chaotic regions in phase space where particle orbits are not simply quasi-periodic oscillations around periodic orbits.

For axisymmetric potentials, we always know one family of periodic orbits to be the circular ones. If we have a weak non-axisymmetric perturbation in addition, we should be able to relate the periodic orbits to the ones in the unperturbed case. We can picture orbit families in a so-called characteristic diagram, usually a plot where the intersection of the orbit with the coordinate axis perpendicular to the bar is drawn versus Jacobi energy. While there is no perturbation, the circular orbits are lying on a single line in this diagram. At the prospective resonance radii with resonances of type $(n = \pm 1, m$ even$)$, we have bifurcations, where additional periodic orbits branch off (remember that the resonance condition means closure of epicyclically oscillating orbits viewed in the rotating frame), though these are usually unstable. On switching on the perturbation, the line gets broken at the bifurcation points, and we have a gap forming. Furthermore, the branched-off families may gain stability. Contrarily at odd-numbered resonances, we usually get the formation of a so-called pitchfork bifurcation, which is the branching-off of one stable and one unstable orbit family each time.

In the nomenclature of Contopoulos & Grosbol 1989 [19], we refer to the descendants of the originally circular orbits as family x_1. Very far to the outside, we shall call it $x_1(1)$. Going inwards, the outmost resonance, -1:1, leads to a branching-off of a stable family called simply -1:1 and an unstable one called -1:1 (Asym), though the latter are actually symmetric with respect to the bar. Further in, the gap caused by the OLR replaces $x_1(1)$ as the dominant family by a family called $x_1(2)$, which itself has an unstable continuation called $x_1^*(2)$. Going further in, the -1:3 resonance causes another pitchfork bifurcation of families -1:3 and -1:3 (Asym), the outer UHR causes again a gap replacing $x_1(2)$ by a $x_1(3)$ and so on. See Fig. 2.5 for an illustration. Generally, an $x_1(n)$ orbit has $2n$ cusps.

Inside co-rotation, the same happens in reverse order. In the case of a double ILR, however, we often have a so-called bubble, i.e. there are two resonant 1:2 families, above and below the x_1 in the unperturbed case, joining the two ILRs. Switching on the perturbation, the outward parts of the x_1 usually get connected with the lower loop of the bubble, whereas the rest joins the upper part of the

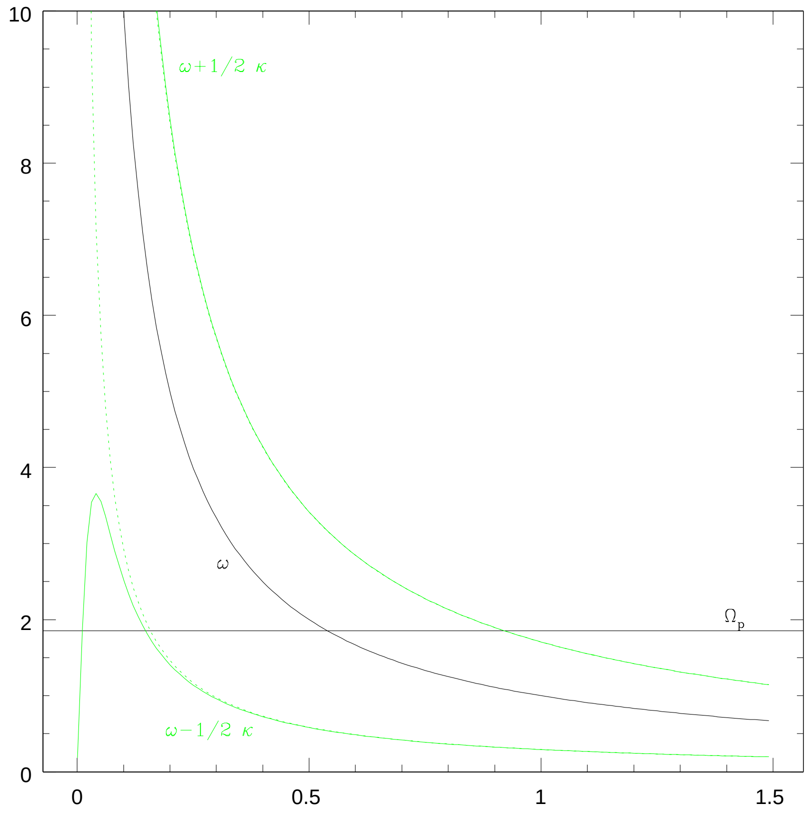

Figure 2.4: Angular frequency $\omega(R)$ and the curves $\omega(R) \pm 1/2\kappa(R)$ for an assumed axisymmetric galactic background with (dotted) or without a central mass concentration (solid lines). Note the maximum in the ILR-curve in the latter case. Position of co-rotation and the Lindblad resonances is determined by the intersections with the constant pattern speed Ω_p of the bar, so there might be two ILRs or none in this case.

bubble and closes in on itself. The upper part of this floating bubble is an unstable family x_3, the lower a stable family x_2, which is dominant in the region in between the ILRs. In addition, there is a family of retrogade orbits inside co-rotation, which is called x_4.

The alignment of the orbits' elongation with the bar changes on every resonance (see Table 2.2), a behaviour akin to the phase reversal of a driven harmonic oscillator as it wanders over a resonance. As a consequence, bars cannot extend beyond the co-rotation region, because the highest populated orbits outside CR are anti-aligned with the bar.

Finally, there are two families of orbits which are trapped around the Lagrangian point L4 and L5 of the potential. They are called long and short period orbits (LPO and SPO). LPOs have the shape of elongated bananas parallel to the bar, whereas SPOs are more or less elliptical and only slightly elongated. The Jacobi energy of SPOs is always greater than Φ_{eff} at L4/L5, while that of LPOs is usually smaller. Non-periodic orbits around L4 and L5 often show the same banana shape as the LPOs, but fill the interior of it, partially or completely. They are quasi-periodic, formed by combining the oscillation frequencies of the LPOs and SPOs. See Fig. 3.5 for an example.

location	family	bar alignment	comment
$<$ IILR	x_1	aligned	possible cause of small central bars
IILR - OILR	x_2	anti-aligned	only in case of two ILRs
OILR - ...	x_1	aligned	main supporters of galactic bars
...			
CR			
...			
... - OUHR	$x_1(3)$	anti-aligned	no bars possible outside CR
OUHR - OLR	$x_1(2)$	anti-aligned	
$>$ OLR	$x_1(1)$	aligned	

Table 2.2: Dominant orbit families in a weakly barred potential and their alignment relativ to the bar. Towards the CR, there is an infinity of families in ever smaller regions.

2.3 Kinematics of the solar neighbourhood

Like in hydrodynamics, we would expect the motion of the stars to consist of a macroscopic flow pattern, and superposed on that, random motions. The relative magnitude of the ordered and unordered motions is characteristic for the type of galaxy we have: for elliptical galaxies, the statistical dispersion of the random motions is larger than the ordered flow, whereas the inverse is true for disk galaxies. For the latter, dispersions typically range around some 10% of the rotation velocity, thus constituting a dynamically warm disk.

Since the Sun is but another star, we expect it to take part in the random motion, and since the Sun's peculiar velocity is physically irrelevant, we want to correct it out. In the following, we deal with the reconstruction of the local macroscopic flow velocity in section 2.3.3, with the properties of the random motions (sections 2.3.2 and 2.3.1) and with the differential flow field in the larger vicinity (section 2.3.4).

2.3.1 The velocity ellipsoid

The random motions of the stars constitute a distribution in velocity space reminiscent of a thermal distribution of Maxwell type. However, due to the collisionless nature of the stellar fluid, there may be anisotropies which in a collision-dominated gas would have been equilibrated out.

Karl Schwarzschild suggested in 1907 [85] to model the velocity distribution of the solar neighbourhood in the simplest possible way as a Gaussian distribution function. This has become known as the Schwarzschild distribution:

$$f(\mathbf{v})d^3\mathbf{v} = \frac{n_0\ d^3\mathbf{v}}{(2\pi)^{3/2}\sigma_1\sigma_2\sigma_3} \exp\left[-\left(\frac{v_1^2}{2\sigma_1^2} + \frac{v_2^2}{2\sigma_2^2} + \frac{v_3^2}{2\sigma_3^2}\right)\right], \tag{2.16}$$

where all the velocities are with respect to the local standard of rest (LSR) defined below (section 2.3.3).

We can define a velocity dispersion tensor as in (2.5) from the measured peculiar velocities of the neighbouring stars. The σ_i in Schwarzschild's distribution then correspond to the eigenvalues of this tensor, and the v_i are components taken along its principal axes. The Schwarzschild model is the simplest model if one only knows the σ_{ij}. It neglects any asymmetries of the distribution as for example the asymmetric drift. Apart from that, determinations of the true distribution as done by

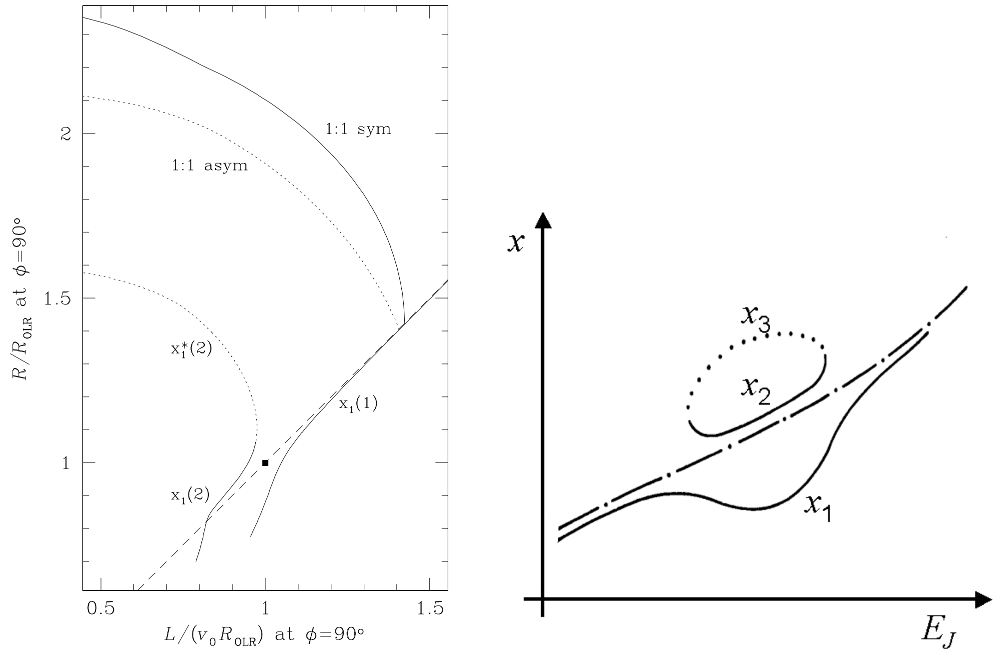

(a) (b)

Figure 2.5: Periodic orbit families in a weakly barred potential. Solid lines denote stable, broken lines unstable families. (a) outside, (b) inside co-rotation. (a) taken from Dehnen 2000 [28].

Dehnen 1998 [25] using the HIPPARCOS data (see section 2.3.5) show lots of additional structure. Thus, the Schwarzschild distribution is merely a very crude approximation.

If we nonetheless adopt the Schwarzschild distribution as an approximation to the true distribution, we find two main features which we will investigate further: (1.) the orientation of the principal axes, (2.) the axis ratio of the ellipsoids representing the isodensity contours. We are mostly concerned with the situation in the Galactic plane, and since the Sun is located sufficiently close to the plane, we do not expect any effects in components involving the vertical direction. Indeed, the velocity ellipsoid axes do not seem to be tilted out of the Galactic plane (Dehnen & Binney 1998 [31]). Qualitatively, the behaviour of the axis ratios is such that the ellipsoid is elongated in the direction of the Galactic rotation (in accordance with the results from epicycle approximation, see section 2.2.1), and that the shortest axis is the vertical one, which reflects the disky structure of the Galaxy. The axis ratio in the plane is a topic which we will repeatedly come back to in the following.

A mis-alignment of the velocity dispersion ellipsoid with respect to the direction to the Galactic center is called vertex deviation. It corresponds to a non-vanishing off-diagonal element ot the dispersion tensor (2.5) within the plane. This can only occur if there are deviations from axisymmetry in the Galaxy. Using HIPPARCOS data, it has been shown by Dehnen & Binney 1998 [31] to reach as high as 30° for very young stellar populations, and to lie in a range of $\sim$ 10° for the old ones. Whereas the high vertex deviation of the young populations is most probably due to the moving groups and thus in a sense accidental (Binney & Merrifield 1998 [10]), there should be dynamical reasons for its occurence with the old populations. Often this is attributed to spiral structure, but the bar may also play a role (see e.g. Kuijken & Tremaine 1994 [61]).

2.3.2 Velocity dispersion as a function of age and radius

The velocity dispersion of the stars shows an increase with age (see e.g. Wielen 1977 [97]), or, observationally, with colour (colour correlates with age statistically since bluer stars end their life-cycles earlier and are thus sorted out). Plots of dispersion versus colour for stellar samples (as again in Dehnen & Binney 1998 [31]) show positive gradients, which at around $B - V \approx 0.6$ turn abruptly to zero. This change in slope, known as Parenago's discontinuity, is thought to be a consequence of the finite age of the Galaxy: stars redder than this point have a life-cycle longer than this age and therefore the statistical correlation between age and colour is lost. Translating the colours to ages requires some modelling, see e.g. Binney, Dehnen & Bertelli 2000 [7]. The dispersion-age-relation is found to be consistent with $\sigma(t) = C \cdot t^{\beta} + \sigma_{t=0}$, with β in the range $0.2 - 0.5$. Binney, Dehnen & Bertelli find $\sigma_{t=0} \approx 8$ km/s and $\beta \approx 0.33$, and an age of the solar neighbourhood of 11.2 ± 0.75 Gyr.

The observed increase in dispersion with age suggests that the disk is being heated. An alternative explanation, assuming that stars were born with higher velocity dispersion in earlier times and thus invoking some secular evolution effect, is rarely drawn into serious consideration. Regarding the origin of the disk heating, direct star encounters are ruled out, because the relaxation times for these processes are much to high. Several mechanisms have been discussed (Binney 2001 [6]):

- Perturbations by giant molecular clouds (GMCs), first proposed by Spitzer & Schwarzschild 1953 [89]. However, Lacey 1984 [62] showed that the ratio of vertical to horizontal dispersions expected from this do not agree with observations.
- Perturbations by spiral arms (Carlberg & Sellwood 1985 [15]). However, only motions within the Galactic plane should be excited by this.
- Perturbations by infalling satellite galaxies. However, the resulting disk heating tends to be too high in this case, cf. Fuchs et al. 2001 [45].

Up to now, the question of the true reason of disk heating is not finally settled. Probably, an interplay of several factors must be assumed.

The spatial variation of the velocity dispersion is known from some measurements on external galaxies. Although this is quite a difficult task, Bottema 1993 [14] managed to obtain the radial dependence of the vertical dispersion σ_z for a set of face-on disks. It shows an exponential decline with radius similar to surface density, however with a larger scale length, which might approximately be twice as large. Indeed, this is the behaviour expected from stellar dynamics, where we can derive from the Jeans equations that for a thin disk the vertical dispersion should obey

$$\sigma_z^2 = 2\pi G \Sigma h, \tag{2.17}$$

h being the vertical scale-height. The same should hold for the other components of the velocity dispersion, since the shape of the velocity ellipsoid probably does not change very much. This is at least the result of an investigation by Gerssen et al. 1997 [48] where these authors tried to determine two dispersion components of an inclined disk galaxy simultaneously, however using the (in our view problematic) eqn. (3.19).

2.3.3 The local standard of rest (LSR) and asymmetric drift

If the Galaxy were completely axisymmetric, we expect the ordered flow of the stars to be a uniform rotation around the Galactic center. We call a reference frame which follows this uniform rotation a *standard of rest*, and *local standard of rest* (LSR) for the location of the Sun. Their rotation velocities are determined by the potential according to (2.7). One should think that the mean value of the (galactocentrically) tangential velocities of a spatially constrained sample of stars should equal these circular velocities. However, for non-vanishing velocity dispersion this is not the case. Instead, the mean rotation velocity is falling behind the circular velocity value, a phenomenon known as *asymmetric drift*. In terms of the epicycle approximation, it can be understood by remembering that the epicycle ellipse is a retrograde rotation. Thus stars on the outward part of their epicycle ellipse are moving slower than their guiding center, whereas the inverse is true on the inner part. Asymmetric drift then results from there being, at any location, more stars from the inside than from the outside, and this in turn is due to two effects:

- The exponential decrease in density of the stars with radius means that at some distance inside of a given radius there are more stars than at the same distance to the outside of it.
- The velocity dispersion itself is decreasing with the distance from the Galactic center, so that stars from smaller radii reach farther out than those from larger radii reach in.

Quantitatively, we can give an empirical formula ("Strömberg's relation") for the asymmetric drift $v_a = v_c - \bar{v}$, where $\bar{v}$ denotes the actual mean velocity of a stellar population (see e.g. Binney & Tremaine 1986 [11]):

$$v_a = \frac{\sigma_R^2}{D}, \qquad \text{where } D \approx 80 \text{ km/s}, \tag{2.18}$$

and σ_R is the dispersion in the radial direction.

The common way of determining the LSR is to consider distinct stellar populations which have different velocity dispersions, to calculate the mean motion for every one of these, and to extrapolate to the case of vanishing velocity dispersion. This program has been carried out by Dehnen & Binney 1998 [31] for the HIPPARCOS data, giving the motion of the Sun relative to the LSR as

$$\begin{aligned} U_\odot &= 10.00 \pm 0.36 \text{ km/s} \\ V_\odot &= 5.23 \pm 0.62 \text{ km/s} \\ W_\odot &= 7.17 \pm 0.38 \text{ km/s} \end{aligned} \tag{2.19}$$

where U, V, W are velocity components towards the Galactic center, in the direction of Galactic rotation and in the vertical towards the north Galactic pole, respectively. In the literature, there is widespread agreement for the values of $U_\odot$ and $W_\odot$, whereas most authors give values in the range of $10 - 20$ km/s for $V_\odot$ (see e.g. Mignard 2000 [68] for a recent example). This is due to an increase of the tangential velocities at very small dispersions, leading to these high values in the extrapolation. But small dispersions correspond to very young stars, and according to Dehnen & Binney 1998 these have to be excluded when extrapolating to vanishing dispersion, because very young stars are not yet kinematically equilibrated (they belong to moving groups and so still bear memory of their parent cloud), or the validity of Strömberg's relation breaks down. Using only less young stars, Dehnen & Binney arrive at the quoted value of about 5 km/s for $V_\odot$. Correspondingly, the slope of Strömberg's relation comes out higher, so Dehnen & Binney obtain the value for D of 80 ± 5 km/s quoted above, whereas usually ~ 120 km/s have been assumed before.

If the Galaxy is not completely axisymmetric, the definition of the LSR is less clear, since there are no longer uniquely defined circular velocities. In fact, we will withdraw to a purely operational definition of the standards of rest, by doing local averaging and correcting for asymmetric drift in the described way. It is possible then that such a standard of rest has radial and vertical components of motion, which cannot occur in the axisymmetric case. In addition, there might be some tangential component relative to some (generally ill-defined) uniform rotation.

2.3.4 Oort constants and the differential rotation of the Galaxy

The kinematic theory of Galactic rotation has been developed by Jan Hendrik Oort in 1926/27 [73, 72]. He introduced two of the constants now bearing his name which measure the effect of differential rotation on the local velocity field.

Define a standard of rest system for every point $\mathbf{r}$ of the disk and denote its velocity by $\mathbf{v}_{\mathrm{SR}}(\mathbf{r})$. Take a special one of these frames, e.g. the one at the Sun's position $\mathbf{r}_\odot$, as the LSR and call its velocity $\mathbf{v}_{\mathrm{LSR}}$. Then, if (x, y) relate to some coordinate system centered on $\mathbf{r}_\odot$, the relative velocity field $\mathbf{w}(\mathbf{r}) := \mathbf{v}_{\mathrm{SR}}(\mathbf{r}) - \mathbf{v}_{\mathrm{LSR}}$ in the neighbourhood of $\mathbf{r}_\odot$ can be written as

$$\begin{aligned}\mathbf{w}(\mathbf{r}) &= \begin{pmatrix} \frac{\partial w_x}{\partial x} & \frac{\partial w_x}{\partial y} \\ \frac{\partial w_y}{\partial x} & \frac{\partial w_y}{\partial y} \end{pmatrix} \begin{pmatrix} x \\ y \end{pmatrix} + \mathcal{O}\left(d^2\right) \\ &=: \begin{pmatrix} k+c & a-b \\ a+b & k-c \end{pmatrix} \begin{pmatrix} x \\ y \end{pmatrix} + \mathcal{O}\left(d^2\right), \end{aligned} \tag{2.20}$$

where $d = |\mathbf{r} - \mathbf{r}_\odot| = \sqrt{x^2 + y^2}$.

k and b have the physical meaning of the divergence and vorticity of the relative velocity field, respectively, whereas a and c are components of its shear tensor:

$$\nabla \cdot \mathbf{w} = 2k \tag{2.21}$$

$$[\nabla \times \mathbf{w}]_3 = 2b \tag{2.22}$$

$$\tau_{ij} := \partial_i w_j + \partial_j w_i - \delta_{ij} \sum_m \partial_m w_m = 2 \begin{pmatrix} c & a \\ a & -c \end{pmatrix}_{ij} \tag{2.23}$$

Expressing the Oort constants a, b, c, k as derivatives with respect to R and φ is a matter of algebra, cf. appendix E.

Whenever, as in the case of a purely circular rotation, we have a unique rotation curve $v_c(R) = R\,\omega(R)$, we also define

$$A := -\frac{1}{2} R \frac{d\omega}{dR} = \frac{1}{2}\left(\frac{v_c}{R} - \frac{dv_c}{dR}\right) \tag{2.24}$$

$$B := -\left(\omega + \frac{1}{2} R \frac{d\omega}{dR}\right) = -\frac{1}{2}\left(\frac{v_c}{R} + \frac{dv_c}{dR}\right) \tag{2.25}$$

For the purely circular velocity field, we have $k = c = 0$ and $a = A$, $b = B$. In fact, $k = c = 0$ holds for any axisymmetric and stationary disk, whereas a and b reduce to forms similar to (2.24), (2.25), true, but with v_c replaced by the mean rotation velocity $\bar{v}$ (cf. appendix E). So $a = A$ and $b = B$ require also neglection of the asymmetric drift. In general, we have to distinguish between A and B and the true Oort constants a, b, c, k.

Taking components of eqn. (2.20) along the line of sight and along the tangent within the Galactic plane (in direction of increasing Galactic longitude ℓ), we obtain to first order in d:

$$\begin{aligned} v_d &= \frac{1}{d}\,\mathbf{d} \cdot \mathbf{w} &&= d\,(k + c\cos 2\ell + a \sin 2\ell) \\ v_\ell &= \frac{1}{d}\,(\mathbf{d} \times \mathbf{w})_z &&= d\,(b + a\cos 2\ell - c\sin 2\ell) \end{aligned} \tag{2.26}$$

where $\mathbf{d} = (x, y)^t$ as above. We will use this formula as a means to determine the Oort constants in section 4.3.

Observationally, the Oort constants can be determined, by using relations (2.26), via measured proper motions or via line-of-sight velocities[3] of stars in the solar neighbourhood. One recent study of this kind is Feast & Whitelock 1997 [42] who used HIPPARCOS proper motions of Cepheids. Since the HIPPARCOS mission is based on a reference frame constituted of extragalactic sources, these data should be more reliable than earlier measurements (see Kerr & Lynden-Bell 1986 [55] for a review). Feast & Whitelock obtained

$$\begin{aligned} a &= 14.82 \pm 0.84\,\text{km/s/kpc} \\ b &= -12.37 \pm 0.64\,\text{km/s/kpc} \end{aligned} \tag{2.27}$$

According to a new analysis by Olling & Dehnen 2003 [71], all earlier determinations of the Oort constants overlooked a mode mixing effect as one major source of systematic error. Their own determination using a sample of stars from the ACT/Tycho-2 catalogs yield values for a, b and c which depend highly on the age of the stellar sample. For old red giant stars, they get

$$\begin{aligned} a &= 15.9 \pm 1.2\,\text{km/s/kpc} \\ b &= -16.9 \pm 1.2\,\text{km/s/kpc} \end{aligned} \tag{2.28}$$

There are also indications for a non-vanishing c, which has not been found by Feast & Whitelock. Olling & Dehnen obtain $c = -9.8 \pm 1.2$ km/s/kpc

Ignoring possible differences between a, b and A, B, we can calculate the local ω and the slope of the rotation curve via $\omega = A - B$ and $dv_c/dR = -(A + B)$, giving with the Feast/Whitelock data:

$$\omega_0 = 27.19 \pm 0.87\,\text{km/s/kpc} \tag{2.29}$$

$$\left(\frac{dv_c}{dR}\right)_0 = -2.4 \pm 1.2\,\text{km/s/kpc} \tag{2.30}$$

This would mean a slight decline of the rotation curve, which might be a local phenomenon. No decline, but instead a slight rise is implied by Olling & Dehnen's values.

By pure definition, we have

$$\frac{-B}{A-B} = \frac{1}{2}\left(1 + \frac{d\ln v_c}{d\ln R}\right) = \frac{\kappa^2}{4\omega^2} = \frac{1}{\gamma^2} \tag{2.31}$$

Most textbooks feature a relation ("Oort-relation") equating this quantity to the ratio of the squares of the velocity ellipsoid axes, at least in the limit of vanishing velocity dispersion. However, this does not hold in a non-axisymmetric galaxy, and available data indeed show problems with this equality:

- For a flat rotation curve, $-B/(A - B) = 1/2$ exactly, and for a slightly declining rotation curve, the value of $-B/(A - B)$ is smaller than $1/2$. This is, accordingly, what is obtained from the Feast & Whitelock values, whereas those of Dehnen & Olling give something $> 1/2$.

- The theoretical expectation for the axis ratio is a value somewhat larger than $1/2$. This is due to higher-order corrections arising from the velocity dispersion, which should prevail over the effect of a declining rotation curve and cause a value of the axis ratio $> 1/2$ (Kuijken & Tremaine 1994 [61] and 1991 [60]). However, observations indicate a value significantly smaller than $1/2$, e.g. Dehnen & Binney 1998 [31] found 0.4.

---

[3] To avoid confusion, we will always take the term "radial" as relating to a galactocentric coordinate system and refer to radial velocities in the heliocentric sense as line-of-sight velocities. The reader be warned that this is not a common convention, though.

This has been a puzzle for some time (cf. Evans & Collett 1993 [41]). We will have more to say on this problem in section 4.2.

2.3.5 The true velocity distribution

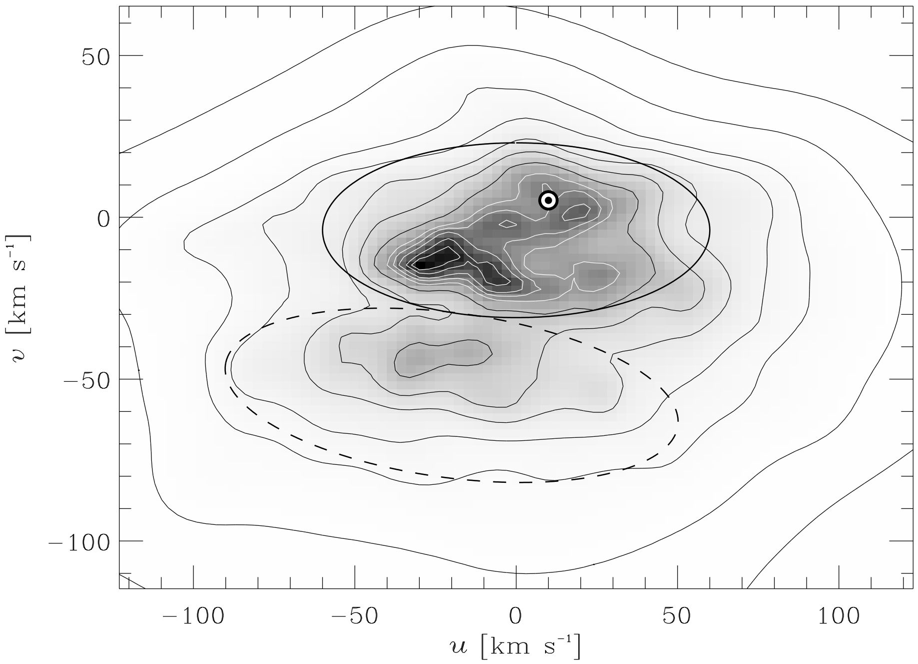

Figure 2.6: Distribution $f(u, v)$ inferred from HIPPARCOS data for late-type stars. The two ellipses indicate the suggested bimodality, the velocity of the Sun is denoted by $\odot$. Taken from Dehnen 1999 [27].

We mentioned already that the Schwarzschild distribution is only a very crude approximation. Reconstructions of the true distribution in velocity space from HIPPARCOS data have been carried out by Dehnen 1998 [25], where much more structure has been found. In particular, when considering early-type stars, the smooth distribution is superseded by moving groups (see Eggen 1996 [36, 37]), which probably reflect the cluster origin of stars. Furthermore the distribution shows a bi-modality which has become known as the "u-anomaly", especially for the late-type stars. If (u, v) denote velocity components with respect to the LSR in the direction the Galactic center and of Galactic rotation, respectively, the anomaly consists of an additional peak around $(u, v) = (-40, -20)$ km/s in the (u, v)-plane distribution, see Fig. 2.6. The respective stars are lagging behind the mean rotation and have an outward radial motion with respect to the LSR. This anomaly was also noted by Raboud et al. 1998 [82] in their independent analysis of the HIPPARCOS data.

Dehnen 2000 [28] explained this bi-modality by a resonant influence of the Galactic bar (see also Fux 2001 [46] and Quillen 2003 [81]). If the Sun is just outside the OLR radius, a bi-modality will naturally come about by the different alignment behaviour of the dominant orbits inside and outside the OLR (see Table 2.2). Stars in the solar neighbourhood from the inside will be on the retrograde part of their epicycle orbit, and thus lag behind the mean (LSR) rotation. If the phase angle of the Sun with respect to the bar is chosen appropriately, as in Fig. 2.7, we can attain a mean outward motion

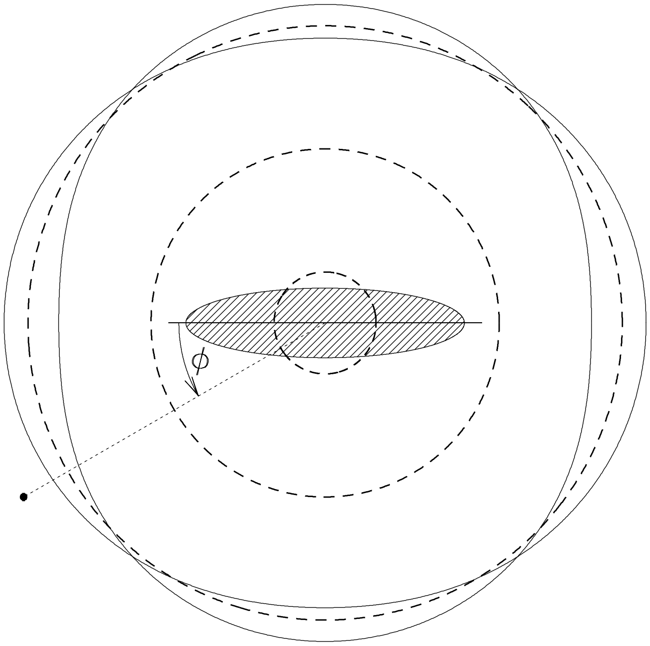

Figure 2.7: Closed orbits (solid curves) just inside and outside the OLR of a rotating central bar (hatched ellipse). The circles (dashed curves) depict the positions of the ILR, CR and OLR (from inside out) for circular orbits. Note the change in the orbits' orientation at the OLR, resulting in the crossing of closed orbits at four azimuths. A possible position for the Sun is shown as filled circle. The bar angle ϕ is indicated for the case of a clockwise-rotating bar. Taken from Dehnen 2000 [28].

for these stars and thus explain the u-anomaly. This will work if the phase angle φ is in the range $10^\circ - 70^\circ$, which is however already constrained by other evidence to lie between 20° and 45°.

Chapter 3

Bar Influence on the Velocity Distribution in the Outer Stellar Disk

As we have mentioned, the bar of the Milky Way may influence the stellar velocity distribution in the solar neighbourhood by resonant phenomena. In particular, the so-called u-anomaly may be a consequence of the location of the Sun shortly outside of the OLR radius, see section 2.3.5. The galactic bar might also have some relevance in explaining the vertex deviation and the anomalous axis ratio velocity-dispersion tensor, which we mentioned in section 2.3.1.

In Dehnen 2000 [28], simulations were made for a localized stellar sample, representing the solar neighbourhood. In this thesis, we will follow this approach further by investigating the velocity distribution in its spatial variability. Our primary interest is in the low-order moments of this distribution, i.e. the mean (streaming) velocity and velocity dispersion. In particular, we want to quantify whether the influence of the Galactic bar may explain the aforementioned anomalies, the vertex deviation and velocity-dispersion axis ratio, observed for the old stellar populations. Our approach applies to the kinematics in the solar neighbourhood, while at the same time it constitutes a completely general analysis of the bar influence in a stellar disk.

3.1 Simulation of bar influence

Since we do not want to construct a self-consistent model of the Galaxy, we just study the stellar dynamics for a simple model potential. In order to arrive at (stationary) equilibrium, we slowly add to the underlying axisymmetric Galactic potential the non-axisymmetric component of the bar (the bar monopole is assumed to be already accounted for by the Galactic potential). We do not pay very much attention to the inner parts (inside co-rotation), and we neglect influences of vertical motion, so our model is two-dimensional. The calculation consists of orbit integration of a large ensemble of phase-space points representing the initial equilibrium. This numerical technique, which may be called *restricted N-body method*, is equivalent to first-order perturbation theory, since the self-gravity due to the wake induced by the perturbation (bar) is neglected. After the orbit integrations, the velocity moments at any time are computed from the phase-space positions of the trajectories.

3.1.1 Sampling

The sampling of the initial phase-space points is done as described in Dehnen 1999 [26], using the distribution function (eq. (10) in [26])

$$f(E,L) = \frac{\omega(R_E)\,\Sigma(R_E)}{\pi\kappa(R_E)\,\sigma^2(R_E)} \exp\left[\frac{\omega(R_E)[L - L_c(R_E)]}{\sigma^2(R_E)}\right], \tag{3.1}$$

where $\omega(R)$, $\kappa(R)$, and $L_c(R)$ are the azimuthal and epicycle frequency and angular momentum of the circular orbit at radius R, while R_E is the radius of the circular orbit with energy E, see eqn. (C.8). With this choice for the distribution function, the collisionless Boltzmann equation is satisfied at $t = 0$ (since f depends only on the integrals of motion E and L) and the surface density and radial velocity dispersion of the disk follow approximately, those given with the *parameter functions* $\Sigma(R)$ and $\sigma(R)$, respectively. Here, we assume exponentials for both of them:

$$\Sigma(R) = \Sigma_0\,\mathrm{e}^{(R_0-R)/R_\Sigma}, \qquad \sigma(R) = \sigma_0\,\mathrm{e}^{(R_0-R)/R_\sigma}. \tag{3.2}$$

If not stated otherwise, we choose $R_\sigma = R_0$ and $R_\Sigma = 0.33R_0$, R_0 being the distance of the Sun from the galactic center. We also set $\sigma_0 = 0.2v_0$ by standard, where v_0 is the circular velocity at R_0. In this way, samples of $K = 10^7$ initial phase-space points are created.

Since the sample corresponds to the stellar disk, we might introduce some outer cutoff to reflect the disk truncation we described in section 2.1. However, to avoid the introduction of additional poorly known parameters we ignore this here.

3.1.2 Model Potential and Orbit integration

Orbit integration and adiabatic growth of a quadrupole bar is done similarly to Dehnen 2000 [28].

The galactic background potential is chosen to give a power law in the velocity curve

$$v_c(R) = v_0\left(\frac{R}{R_0}\right)^\beta, \tag{3.3}$$

namely:

$$\Phi_0(R) = \begin{cases} \frac{1}{2\beta}v_0^2\left(\frac{R}{R_0}\right)^{2\beta} & (\beta \neq 0) \\ v_0^2 \ln\frac{R}{R_0} & (\beta = 0) \end{cases} \tag{3.4}$$

The power-law index is restricted to $\beta \in [-1/2, 1]$ with $\beta = 1$ and $\beta = -1/2$ corresponding to, respectively, the harmonic potential and that of a point mass at the origin.

For the bar potential $\Phi_1 = \Phi_1(R, \varphi, t)$, we only use its quadrupole, since higher poles are much less important at large radii. Following Dehnen 2000 [28], we set

$$\Phi_1 = -A_b(t)\cos 2\varphi \times \begin{cases} (2 - \left(\frac{R}{R_b}\right)^3) & (R \leq R_b) \\ \left(\frac{R_b}{R}\right)^3 & (R > R_b) \end{cases} \tag{3.5}$$

where R_b is the size of the bar. The angle φ is defined in the frame rotating at pattern speed Ω_b (see Fig. 3.1). The strength A_b of the bar is increased from 0 to a value A_f during time $0 < t < t_1$ according to

$$A_b(t) = A_f\left(\frac{3}{16}\xi^5 - \frac{5}{8}\xi^3 + \frac{15}{16}\xi + \frac{1}{2}\right), \quad \xi = 2\frac{t}{t_1} - 1 \tag{3.6}$$

and stays constant at $A_b = A_f$ after t_1. With this functional form, Φ_1 and its first and second time derivative are continuous, thus representing adiabatic growth of the bar and ensuring a smooth transition. The final bar strength A_f is controlled via the dimensionless model parameter α

$$\alpha = 3\frac{A_f}{v_0^2}\left(\frac{R_b}{R_0}\right)^3, \tag{3.7}$$

which is the ratio of the forces due to Φ_1 and Φ_0 at galactocentric radius R_0 on the bar's major axis. Our standard choice is $\alpha = 0.01$. Some properties of this potential are listed in appendix C.

Orbit integration is performed on the sampled particles in the co-rotating frame up to a time $t_2 > t_1$ using a 5th order integrator, cf. appendix B. In contrast to Dehnen 2000 [28], we integrate forward in time. The only effect of working in the rotating frame is one single modification in one of the equations of motion (cf. appendix A), which is incorporated into the integration kernel. Particle states are denoted by their phase space coordinates w consisting of the values of R, φ and of the momenta p_R and $p_\varphi = L$, which are identical in the rotating and the inertial frame. We get the radial and tangential velocities u and v of the particles in the inertial frame simply by

$$u = p_R, \qquad v = L/R \tag{3.8}$$

3.1.3 Calculation of velocity moments

The (p, q)th moment of the velocity distribution at position $\mathbf{r}$ is defined as

$$M_{pq}(\mathbf{r}, t) = \int du\, dv\; u^p v^q\; f(t,\, \mathbf{x} = \mathbf{r},\, \mathbf{v}) \tag{3.9}$$

$$= \int d\mathbf{x}\, d\mathbf{v}\; \delta(\mathbf{r} - \mathbf{x})\; u^p v^q\; f(t,\, \mathbf{x},\, \mathbf{v}) \tag{3.10}$$

with $\mathbf{v} \equiv (u, v)$, where u and v denote, respectively,the radial and azimuthal velocity component (see Fig. 3.1). We do not know the value $f(t,\, \mathbf{x},\, \mathbf{v})$ of the distribution function at any time $t > 0$, but instead have a representative sample $\{\mathbf{x}_k(t), \mathbf{v}_k(t)\}, k = 1, ..., K$ of phase-space points.

Several methods have been applied for evaluating these moments. The simplest is to compute the moment integral (3.10) via Monte-Carlo integration, resulting in

$$M_{pq}(\mathbf{r}, t) = \frac{M_{\rm tot}}{K} \sum_k \frac{1}{\epsilon_k^2}\, w\left(\frac{|\mathbf{x}_k - \mathbf{r}|}{\epsilon_k}\right) u_k^p\, v_k^q. \tag{3.11}$$

where we have replaced the δ-function in equation (3.10) by $\epsilon_k^{-2} w(|\mathbf{x}_k - \mathbf{r}|/\epsilon_k)$ with the weight function

$$w(d) = \frac{2}{\pi}(1 - d^2)\; \theta(1 - d^2), \tag{3.12}$$

where θ is the Heaviside function. The parameter ϵ_k gives the radius over which the kth trajectory contributes to the moment integrals. We adjusted ϵ_k such that a constant number of sampled orbits was expected to fall in the area of radius ϵ_k centered on $\mathbf{x}_k$ by the assumed exponential surface brightness distribution of the disk.

In practice, the zeroth, first and second moments are estimated in this way. From these, the mean velocities and velocity dispersion tensor[1] can be obtained as follows:

$$\bar{u} = M_{10}/M_{00}, \quad \bar{v} = M_{01}/M_{00} \tag{3.13}$$

---

[1] Notation: σ_{uu}^2 etc. are components of the tensor σ^2, whose eigenvalues are the *squares* of the velocity dispersions in the principal directions. Note that σ_{uv}^2 may well be negative.

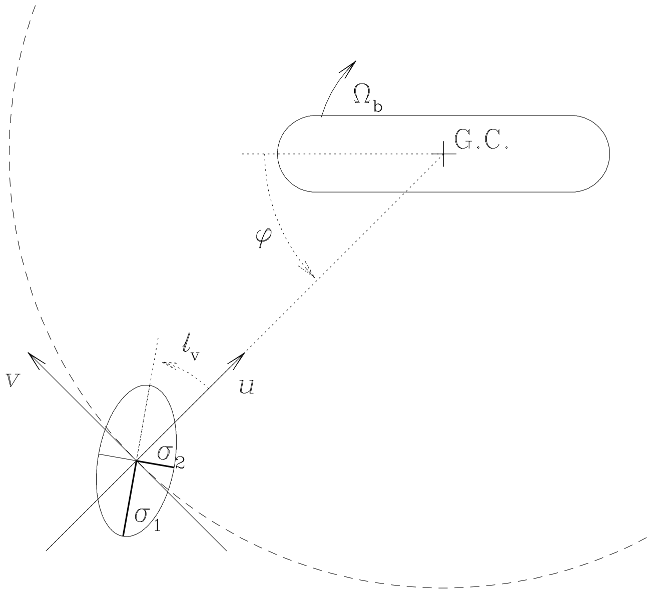

Figure 3.1: Geometry of the rotation of the galaxy and definition of coordinate system. Note that positive values of radial velocity u are taken to point inwards and that azimuth angle φ is measured from the bar axis in the mathematically positive sense, but against the direction of bar rotation (modulo 180°). Also shown is a velocity dispersion ellipsoid exhibiting a (positive) vertex deviation ℓ_v.

$$\begin{gathered}\sigma_{uu}^2 = \frac{M_{20}}{M_{00}} - \left(\frac{M_{10}}{M_{00}}\right)^2, \ \sigma_{vv}^2 = \frac{M_{02}}{M_{00}} - \left(\frac{M_{01}}{M_{00}}\right)^2, \\ \sigma_{uv}^2 = \sigma_{vu}^2 = \frac{M_{11}}{M_{00}} - \frac{M_{10}M_{01}}{M_{00}^2}\end{gathered} \tag{3.14}$$

All this is done for spatial points on a grid.

Once the orbit integration is done, one can easily switch to a model with initial distribution function $f_1 \neq f$ by weighting each orbit with the ratio f_1/f, which accounts for the fact that the trajectories were actually sampled from f. However, for this method to be useful, the ratio f_1/f must not become too large, because otherwise the moment estimates are dominated by a few orbits with large weights. Since by virtue of the collisionless Boltzmann equation the values of the distribution functions are conserved along the trajectories, the ratio f_1/f is conserved, too, and can be evaluated at time $t = 0$, when the distribution functions can be computed via equation (3.1). In this way, we did a switch to exponential disks with velocity dispersions σ_0 smaller than $0.2v_0$ (the value for the sampling distribution functions), such that $f_1/f \leq [0.2v_0/\sigma_0]^2$ (for $\sigma_0 > 0.2v_0$, the ratio f_1/f has no upper limit).

3.1.4 Fourier components of velocity moments

To see what is going on, it is useful to do a Fourier transform on the azimuthal angle φ. We apply this to the mean velocities and dispersion tensor elements after we calculated them in the usual way (3.13 and 3.14), except that this time we do not use a weighting function, but take bins in R and φ. This has the additional advantage that every calculated particle contributes to the final result. We use a discrete

Fourier transform of the following kind:

$$\begin{aligned} c_m &= \frac{2}{N}\sum_{j=1}^{N} f(\varphi_j)\cos m\varphi_j, \\ s_m &= \frac{2}{N}\sum_{j=1}^{N} f(\varphi_j)\sin m\varphi_j, \end{aligned} \tag{3.15}$$

where $\varphi_j = 2\pi j/N$. This gives an approximate Fourier expansion

$$f(\varphi) \approx \frac{c_0}{2} + \frac{c_n}{2}\cos n\varphi + \sum_{m=1}^{n-1}(c_m \cos m\varphi + s_m \sin m\varphi), \tag{3.16}$$

where $n = N/2$ and N is supposed to be even. This has been done for $N = 32$ in 25 radial bins. Since we have an azimuthal $m = 2$ symmetry, we expect all coefficients of odd index m to be zero, which they turn out to be within their errors.

We also construct an estimate of the surface density Σ by dividing the number of sampled orbits per bin by the segment area of the bin, and apply the Fourier transform to this quantity as well.

3.1.5 Error estimation

We employ a bootstrap method: the calculations leading from the data set of every radial bin to its Fourier coefficients are redone for arbitrary subsamples of this data set. The rms-scatter in the outcome of many such calculations gives a measure of the error.

3.1.6 Integration times and models

Usually we follow our models up to 18 bar rotation periods, after the bar has grown adiabatically within the first 5 periods. We also did one model with a very long integration time of 120 bar periods, where we also allowed a longer time of 10 periods for bar growth. In absolute time, the bar period is fixed by our choice of the OLR radius. Our favoured value is $0.92R_0$, and adopting the IAU recommended values of $R_0 = 8.5$ kpc and $v_0 = 220$ km/s, this means that one bar rotation period corresponds to roughly 128 Myr. So our standard integration time of 18 periods is equivalent to about 2.3 Gyr, the long integration time of 120 periods is in the range of a Hubble time.

3.1.7 Symmetries and the question of stationarity

In order to check, whether or how far our distributions have reached a stationary equilibrium state, we employ a symmetry consideration. As noted by Fux 2001 [46], equilibrium velocity distributions in an $m = 2$ symmetric potential have a symmetry

$$f(R, \varphi, u, v) = f(R, \pi - \varphi, -u, v), \tag{3.17}$$

which is a consequence of the azimuthal $m = 2$ symmetry and the time-reversal symmetry of stellar dynamics in conjunction with stationarity of the distribution function. We can turn this argument around and use the degree of symmetry as a measure for stationarity. A quantitative measure of the symmetry can be obtained in the obvious way by subtracting corresponding distribution function values over a grid in phase space and doing a quadratic sum over the grid points. Results of these kind of analysis are shown in Fig. 3.2. As can be seen, the simulations showed only a small increase in asymmetry of 15% above the noise level (as given by the initial state as well as a very long-time simulation), which dropped rapidly after bar growth is finished.

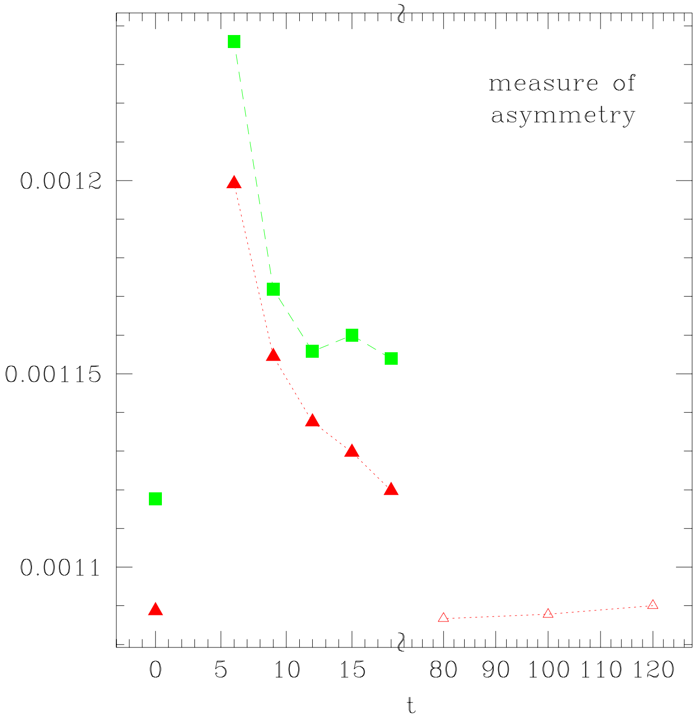

Figure 3.2: Evolution towards stationarity as measured be the symmetry (3.17) for different models (arbitrary units, horizontal axis is time in bar rotation periods). Models shown have $R_{\rm OLR}/R_0 = 0.8$ (square symbols) and $R_{\rm OLR}/R_0 = 0.92$ (triangles), and usual (filled symbols) or long integration time (open symbols). Bar growth is taking place in the first 5 periods for normal and in the first 10 periods for the long integration time. In addition, the value for the sampled starting distribution at $t = 0$ is shown, indicating the level of significance.

3.2 Results

Kuijken & Tremaine 1991 [60] gave an analytical expression for the behaviour of the mean velocities under the influence of a non-axisymmetric perturbation of multipole order m in a linear approximation. For our case, this yields (in a co-rotating frame where $\varphi = \varphi_{\rm Inertial} - \Omega_b t$)

$$\begin{aligned} \bar{u} &= \frac{\alpha(R) v_0^2}{3R} \frac{3\Omega_b - \omega}{(\omega - \Omega_{\rm ILR})(\omega - \Omega_{\rm OLR})} \sin 2\varphi, \\ \bar{v} &= v_0 - \frac{\alpha(R) v_0^2}{6R} \frac{4\Omega_b - \omega}{(\omega - \Omega_{\rm ILR})(\omega - \Omega_{\rm OLR})} \cos 2\varphi, \end{aligned} \tag{3.18}$$

where $\Omega_{\rm ILR}$ and $\Omega_{\rm OLR}$ refer to the circular frequencies at the radii of the inner and outer Lindblad resonance, and $\alpha(R) = 3A_f/v_0^2\ (R_b/R)^3$ is defined similarly to (3.7). For a flat rotation curve, $\omega = v_0/R$. In our range of interest, equations (3.18) are dominated by a pole at the OLR.

The results of our simulation, presented below, agree roughly with these expectations: the mean velocities show modulations $\bar{u} \propto \sin 2\varphi$, $\bar{v} \propto \cos 2\varphi$ in the co-rotating frame. The sign of the modulations varies with radius, sign changes should indicate resonances. For the dispersion tensor the situation is similar: the off-diagonal component shows a $\sin 2\varphi$ perturbation, the diagonal components a $\cos 2\varphi$.

3.2.1 Fourier analysis

Since we have an azimuthal $m = 2$ symmetry, all coefficients of odd index m are expected to vanish, what they do within their errors. Furthermore, in the undeveloped state before bar growth, all coefficients except those with $m = 0$ are, by construction, zero within their errors.

The $m = 0$ components (Fig. 3.3):

The dashed lines in Fig. 3.3 represent the initial axisymmetric case, which shows an exponential decline in Σ as well as in the diagonal components of velocity dispersion tensor. The mean azimuthal motion deviates from the circular speed v_0 by the asymmetric drift, which is stronger for large σ_0, as expected. The mean radial motion vanishes, as required for any stationary model.

The solid lines in Fig. 3.3 show the radial run of the $m = 0$ components in the barred case. Apart from the components for $\bar{u}$ and σ^2_{uv}, which have to vanish for stationary models, some signs of perturbation are visible, the stronger the smaller σ_0.

First of all, we learn that dispersive effects are quite efficient in drawing resonance-induced features away from the actual position of the resonance. Whereas for small velocity dispersion the association of the features with the OLR at $R_{\rm OLR} = 0.92R_0$ is clearly visible, they appear in the high dispersion case at a radial range of 1.1 to $1.4R_0$, where naively one would not attribute them to the OLR.

In particular, we have a bump in the $\bar{v}$-curve outside of OLR, which becomes more explicit with decreasing dispersion while roughly keeping its absolute magnitude. In contrast to this, the asymmetric drift as the dominant deviation of $\bar{v}$ from the nominal rotation velocity v_0 diminishes with decreasing dispersion. There is a similar bump in σ^2_{uu}, whereas we have a two-fold feature in σ^2_{vv}.

Most of the perturbative features in the $m = 0$ components are induced by the opposite orientation of the near-circular orbits on either side of the resonance.

The $m = 2$ components (Fig. 3.4):

Because of the symmetry of the problem, we expect the $m = 2$ components to be the dominant ones. As for every $m > 0$, we have one more degree of freedom here, since we have a cosine- and a sine-component (see Fig. 3.4), or equivalently, an amplitude and a phase.

The cosine-terms of $\bar{u}$ and σ^2_{uv} as well as the sine terms of Σ, $\bar{v}$, σ^2_{uu}, and σ^2_{vv} vanish (within their error), which is to be expected from equation (3.17) for a stationary model. The behaviour of the remaining non-vanishing terms agrees roughly with the expectation from simple linear theory, cf. equation (3.18). In particular, we see indication of the poles at the OLR radius, though they are, of course, smoothed over. However, there are two significant deviations. First, as σ_0 increases (from left to right panels in Fig. 3.4), the resonant features are shifted away from $R_{\rm OLR}$ to larger radii and are also somewhat smoothed out. Second, there is an additional feature at $R \sim 0.6R_0$, in particular, for $\bar{v}$. When inspecting the orbits of stars dominating at this radius, we find that many belong to an orbit family associated with the stable Lagrange points L_4 and L_5, see Fig. 3.5. These orbits can reach radii far beyond co-rotation and, in a frame co-rotating with the bar, perform a retrograde motion around the Lagrange points. They thus result in a reduced $\bar{v}$ at azimuths perpendicular to the bar and hence lead to a positive $\cos 2\varphi$ component.

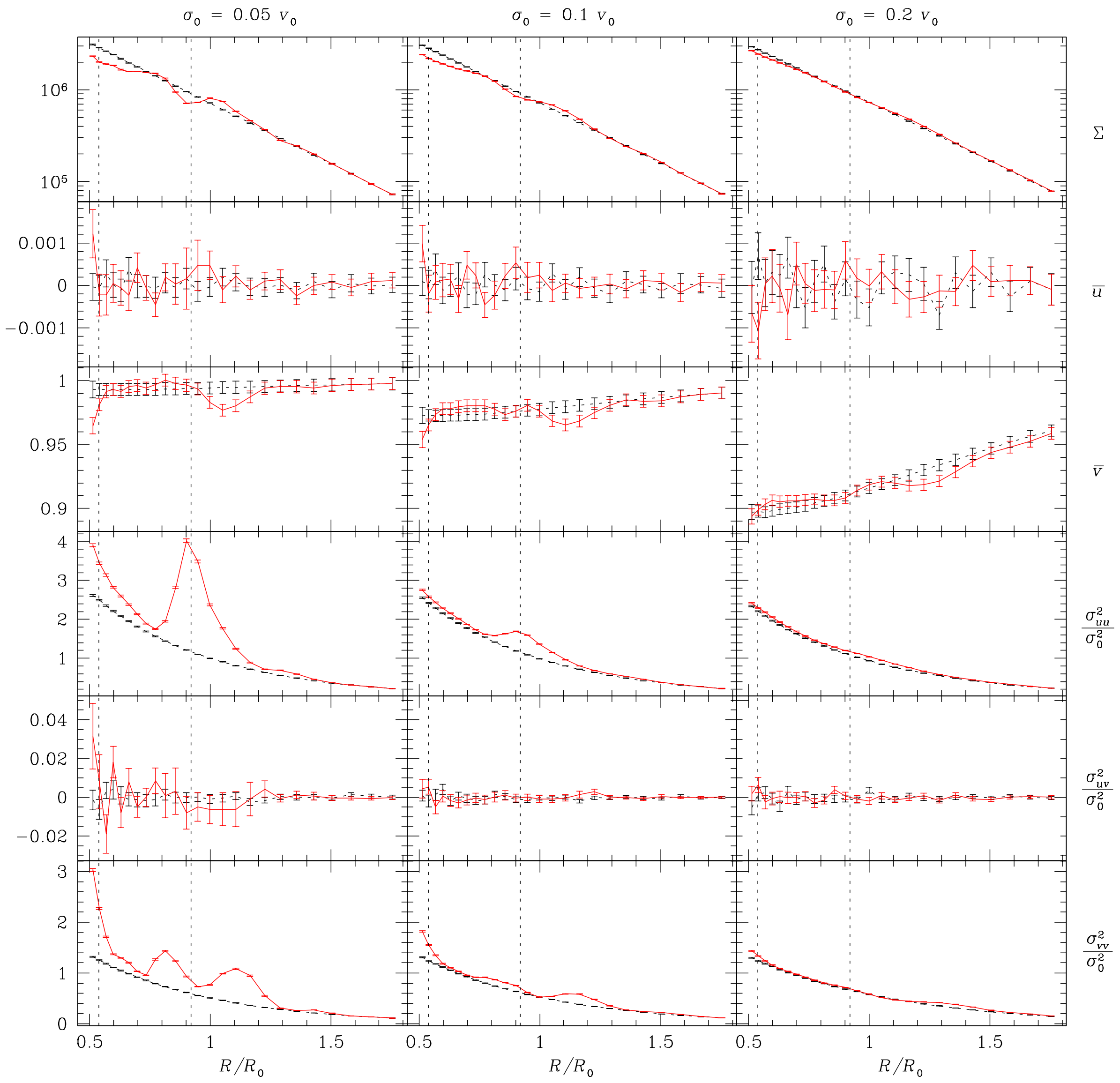

Figure 3.3: $m = 0$ Fourier components of velocity distribution in the undeveloped state before bar growth (*dashed curve*) and in the final state (*solid red curve*), plotted against radius. Left, middle, and right panels have $\sigma_0 = 0.05v_0$, $0.1v_0$ and $0.2v_0$ respectively. The plotted values are actually half the Fourier coefficient, i.e. the first term in expansion (3.16). Units on the vertical axes are particle number per area for surface density Σ and v_0 for the velocities. The model shown has an OLR-radius of $0.92R_0$, corresponding to a CR of $0.539R_0$ (*dashed vertical lines*).

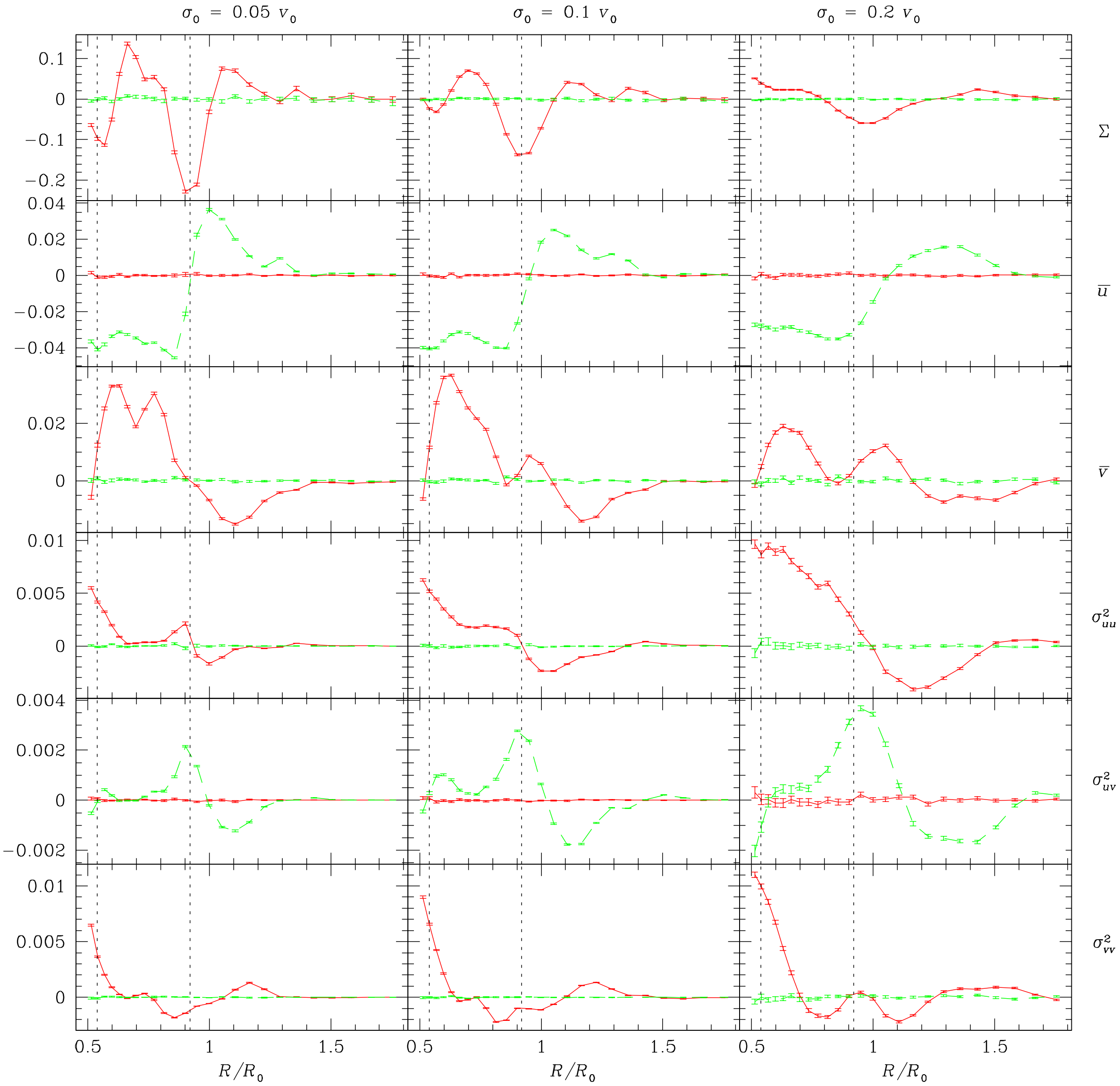

Figure 3.4: $m = 2$ Fourier cosine (*solid red line*) and sine (*dashed green line*) components, plotted against radius. Panels as in Fig. 3.3. For surface density Σ, the value shown is relative to the undisturbed $m = 0$ value. Units on the vertical axes are v_0 for velocities $\bar{u}$ and $\bar{v}$ and v_0^2 for the σ's. OLR and CR are at $0.92R_0$ and $0.539R_0$ respectively (*dashed vertical lines*).

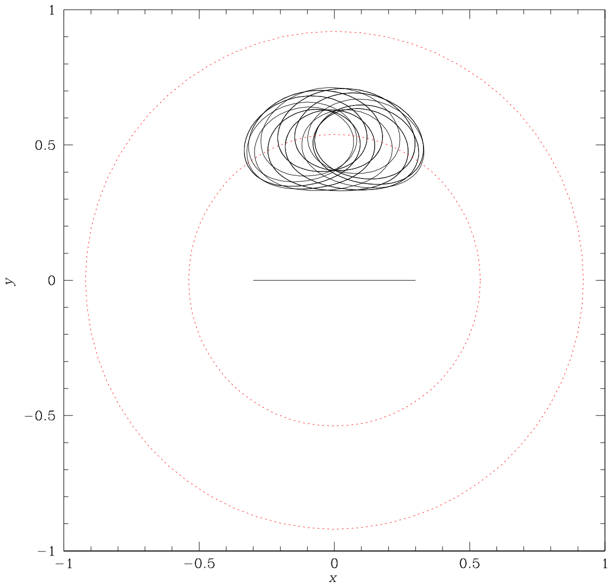

Figure 3.5: Orbit near co-rotation that circulates the L_4 point in a retrograde sense (anti-clockwise for a clockwise rotating bar). The bar is indicated by a line, while the dotted circles correspond to CR and OLR. In our model, a considerable fraction of stars is trapped in orbits of this family, resulting in the somewhat peculiar run of the velocity moments (Fig. 3.4).

Higher-order components (Fig. 3.6) :

The $m = 4$ components are usually smaller by at least a factor 3 compared to the $m = 2$ modes, but they are significantly different from zero. In contrast, the analytical model (3.18) had no excitation of higher modes at all, since mode coupling is not included in a linear approximation.

The excitation of the $m = 4$ modes follows the overall pattern seen in the $m = 2$ case: in accordance with the symmetry requirements, we have a $\sin(4\varphi)$ in u and σ_{uv}^2, and a $\cos(4\varphi)$ in all the other components, see Fig. 3.6. Our signal-to-noise ratio is in the range of 3 – 5 for the $m = 4$ case, and less for higher-order components, so surely the significance of our model is petering out. Nevertheless, some $m = 8$ modes do seem to be discernible still.

3.2.2 Variation of parameters

Doubling the bar strength leads to a doubling of the magnitude of the effects. This is true for the differences between the undeveloped and final state as well as for Fourier coefficients.

Changing the bar size, i.e. the parameter R_b in (3.5), produces some local variations in the magnitude of the effects, but it does not shift them in location. Of course, this is to be expected if the location is determined by resonance conditions.

Variation of the disk scale length does not seem to have any strong effects, which is to be expected, since it only slightly affects the sampling of the orbits but not the dynamics.

The shape of the velocity curve has a mild effect: we tried models with a slightly rising ($\beta = 0.1$) or falling ($\beta = -0.1$) velocity profile, and found very similar results as for $\beta = 0$. (Note that we kept the OLR radius fixed, so models with different velocity profiles have different rotation frequencies of the bar, cf. appendix C). This is expected, too, since β essentially controls the distances between various resonances (growing wider for larger β), while most of our results are dominated by a single

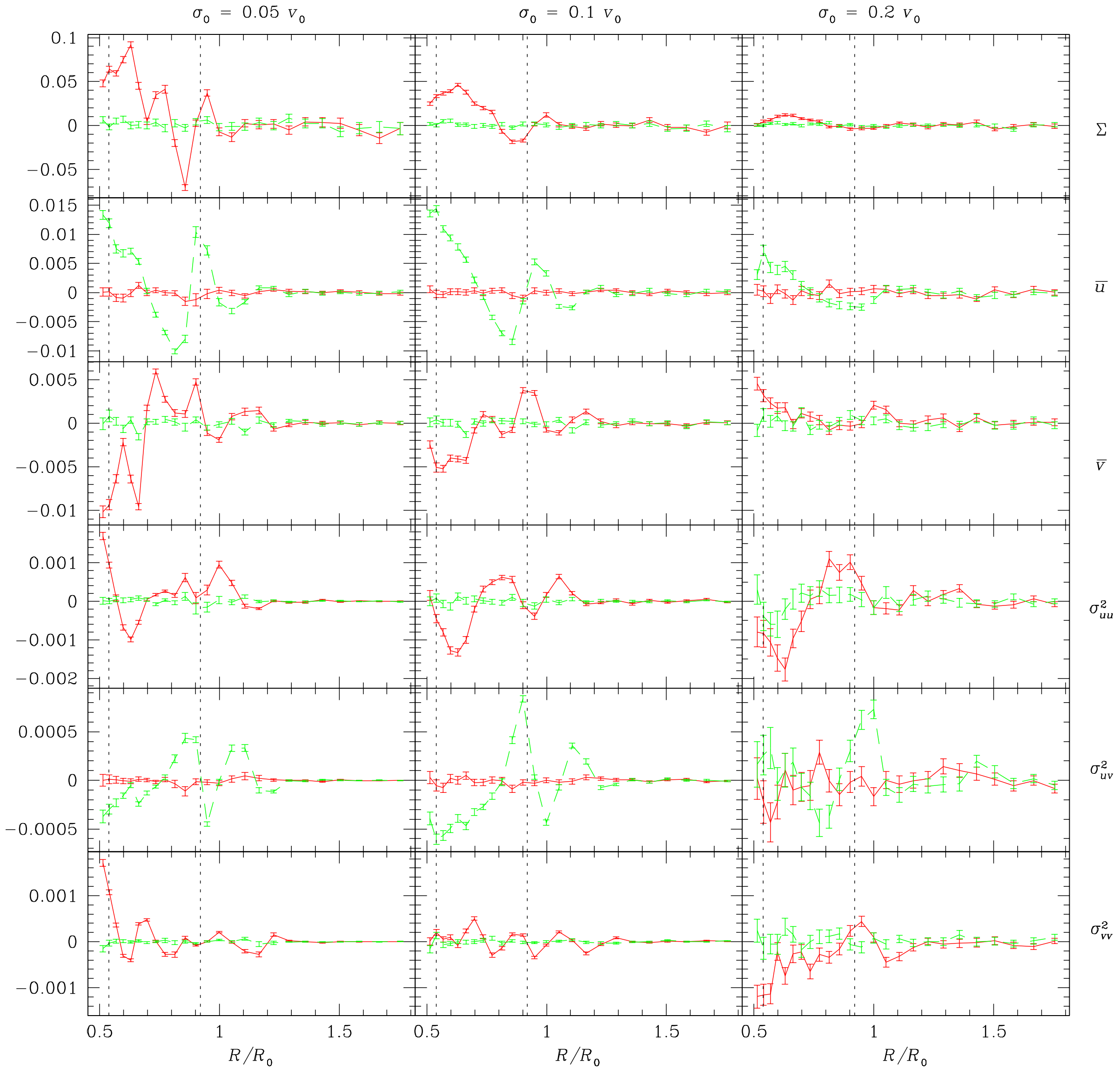

Figure 3.6: $m = 4$ Fourier cosine (*solid red line*) and sine (*dashed green line*) components, plotted against radius. Panels and units as in Fig. 3.4. For surface density Σ, the value shown is relative to the undisturbed $m = 0$ value. Again, OLR and CR are at $0.92R_0$ and $0.539R_0$ respectively (*dashed vertical lines*).

resonance, the OLR.

3.2.3 Dispersion axis ratio

Fig. 3.7 shows the ratio of the principal axes of the velocity dispersion ellipsoid, i.e. the eigenvalues $\sigma^2_{1,2}$ of the tensor σ^2. For a flat rotation curve, this ratio is often expected to be 0.5. Indeed, it can be shown (see for example Binney & Tremaine 1987 [11], ch. 4.2.1(c)) that in the undisturbed case (for which $\sigma_1 = \sigma_{uu}$ and $\sigma_2 = \sigma_{vv}$)

$$\lim_{\sigma\to 0} \frac{\sigma_2^2}{\sigma_1^2} = \frac{\kappa^2}{4\Omega^2} \equiv \frac{1}{2}\left(1 + \frac{d\ln v_c}{d\ln R}\right), \tag{3.19}$$

where κ is the epicycle frequency, cf. eqn. 2.31. This relation is often given without the limit and then referred to as Oort's relation. It is, however, important to note that the error in Oort's relation is considerable already for $\sigma_0 = 0.2v_0$ (Evans & Collett 1993 [41], Dehnen 1999 [26]), which means that using it for the old stellar disk of the Milky Way is, at best, dangerous. This can be seen clearly from Fig. 3.7 showing that σ_2^2/σ_1^2 for the unperturbed case significantly deviates from 0.5 for a warm stellar disk ($\sigma_0 = 0.2v_0$).

After formation of the bar perturbation, we have large variations in this quantity. For $\sigma_0 = 0.2v_0$ and at $R = R_0$, the values are generally somewhat higher than Oort's value 0.5 but smaller than for an undisturbed disk. For directions that are roughly along the bar ($\varphi \sim 0$), this ratio rises sharply just outside the solar circle to values reaching as high as 0.8.

It is instructive to take a look at the same quantities for a smaller velocity dispersion of $\sigma_0 = 0.05v_0$ or $0.1v_0$ (left and middle panels of Fig. 3.7). First of all, the axis ratio in the undisturbed case (dashed line in the right panels) is much closer to Oort's value of 0.5 here, as expected. Generally, the observed features have smaller width, i.e. they are less washed out by dispersion, but the effect of the bar, i.e. the difference between the solid and dashed lines, is still similar for the different velocity dispersions, even quantitatively. Thus, the deviation of σ_2^2/σ_1^2 from Oort's value may be decomposed into a velocity-dispersion dependent term, which consists of a general elevation of only mild radial dependence and a bar-induced term, which varies spatially and appears to be negative for the solar position.

As a consequence, for mildly warm stellar disks ($\sigma \lesssim 0.2v_0$), the ratio σ_2^2/σ_1^2 in the solar neighbourhood may well drop below Oort's value.

3.2.4 Vertex deviation

The so-called vertex deviation

$$\ell_v = \frac{1}{2}\arctan\frac{2\sigma_{uv}^2}{\sigma_{uu}^2 - \sigma_{vv}^2} \tag{3.20}$$

is the angle between the direction of the largest velocity dispersion and the line to the Galactic center, see also Fig. 3.1. For axisymmetric equilibrium models, $\ell_v = 0$.

In Fig. 3.8, we plot ℓ_v, computed from Fourier coefficients up to $m = 2$ only in order to eliminate short-scale fluctuations. We find that the bar-induced vertex deviation decreases with increasing velocity dispersion from up to $\sim 30°$ for $\sigma_0 = 0.05v_0$ to $5° - 10°$ for $\sigma_0 = 0.2v_0$. In the direction of the bar and perpendicular to it, $\ell_v = 0$, as expected from symmetry. For moderately warm stellar disks ($\sigma_0 \gtrsim 0.1v_0$) the vertex deviation at azimuth angles between $0°$ and $90°$ (including the solar azimuth) is positive at and inside the solar circle and negative for some range outside. The actual radius where the sign change occurs is obviously coupled to the OLR, but again shifted to the outside. For a cold

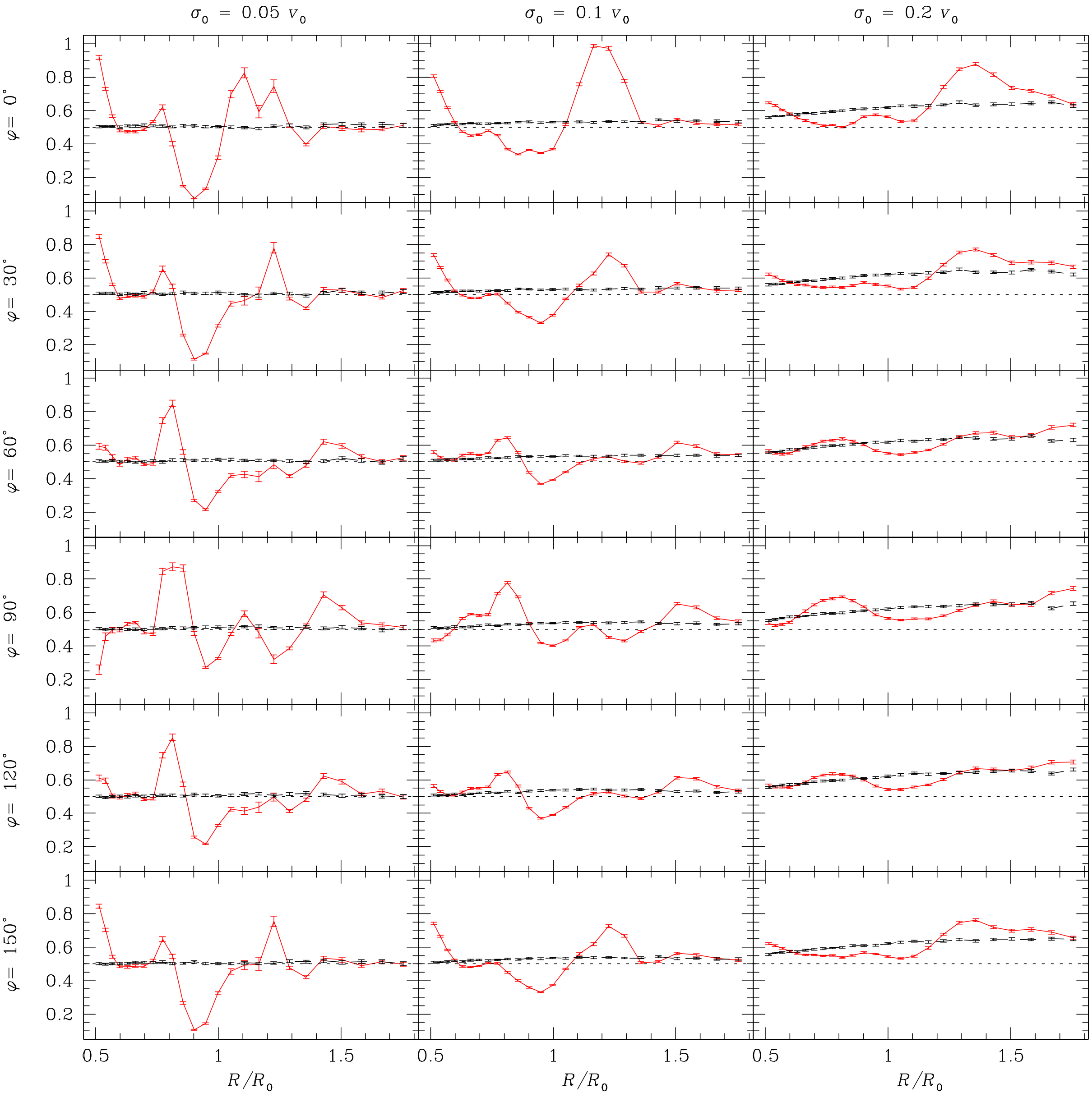

Figure 3.7: Axis ratio σ_2^2/σ_1^2 of the principal components of the velocity-dispersion tensor for the final (*solid, red*) and the initial unperturbed state (*dashed*) at various azimuths for the models with $R_{\rm OLR} = 0.92R_0$ and σ_0 of $0.05v_0$ (*left*), $0.1v_0$ (*middle*), and $0.2v_0$ (*right*).

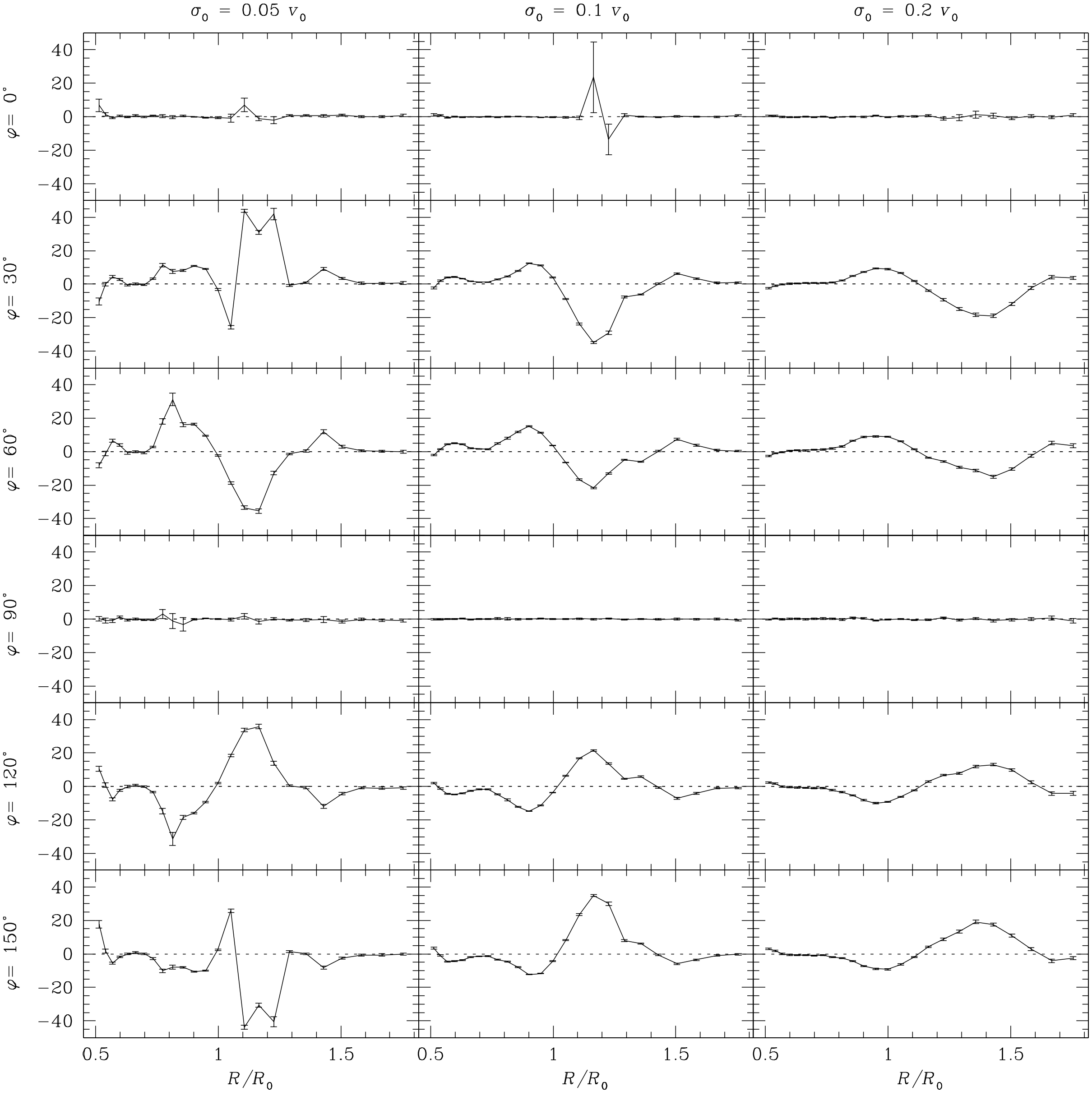

Figure 3.8: Vertex deviation ℓ_v as reconstructed from Fourier components at various azimuths for the same models as in Fig. 3.7. The highly uncertain outliers at $R \sim 1.2R_0$, $\varphi = 0^\circ$ for $\sigma_0 = 0.1v_0$ are caused by a near-circular velocity ellipsoid ($\sigma_1 \sim \sigma_2$, see Fig. 3.7), which renders the vertex deviation ill-defined.

stellar disk, the bar-induced vertex deviation displays are more complicated pattern and may reach as high as $40°$.

Obviously, the vertex deviation is antisymmetric with respect to $\varphi \mapsto (\pi - \varphi)$, whereas the velocity dispersion axis ratio is symmetric. This is a simple consequence of symmetry (3.17), which in particular implies $(\sigma^2_{uu}, \sigma^2_{uv}, \sigma^2_{vv}) \mapsto (\sigma^2_{uu}, -\sigma^2_{uv}, \sigma^2_{vv})$.

3.3 Discussion

Radial motions $\bar{u}$ of standards of rest can be seen to occur quite frequently (see Fig. 3.9), and can reach magnitudes of the order of about $0.02v_0$, corresponding to about 5 km/s for the Milky Way. Because of the $\sin 2\varphi$ dependence, these would be maximal at $\varphi = 45°$, which is quite near the proposed position of the Sun of $\varphi \approx 30°$. In its radial dependence however, $\bar{u}$ swings through zero shortly outside of the OLR, and it may well be that the Sun just meets that point. So we cannot give a definite prediction for the bar-induced radial motion of the LSR here, not even by sign only, except that it should be very small (at most a few km/s).

Observational evidence for radial motion of the LSR is unclear. From measurements of line-of-sight velocities of gas in the outer Galaxy, Blitz & Spergel [13] postulated in 1991 an outward movement of the LSR of around 14 km/s. Contrary to this, Metzger & Schechter 1994 [67] concluded from line-of-sight velocities of carbon stars in the anticenter direction that the LSR is moving inwards at 6.6 ± 1.7 km/s. A recent study (Gould 2003 [51]) based on halo subdwarfs excludes radial LSR motions greater than 2 km/s. If this holds indeed, it would fit very well with our results.

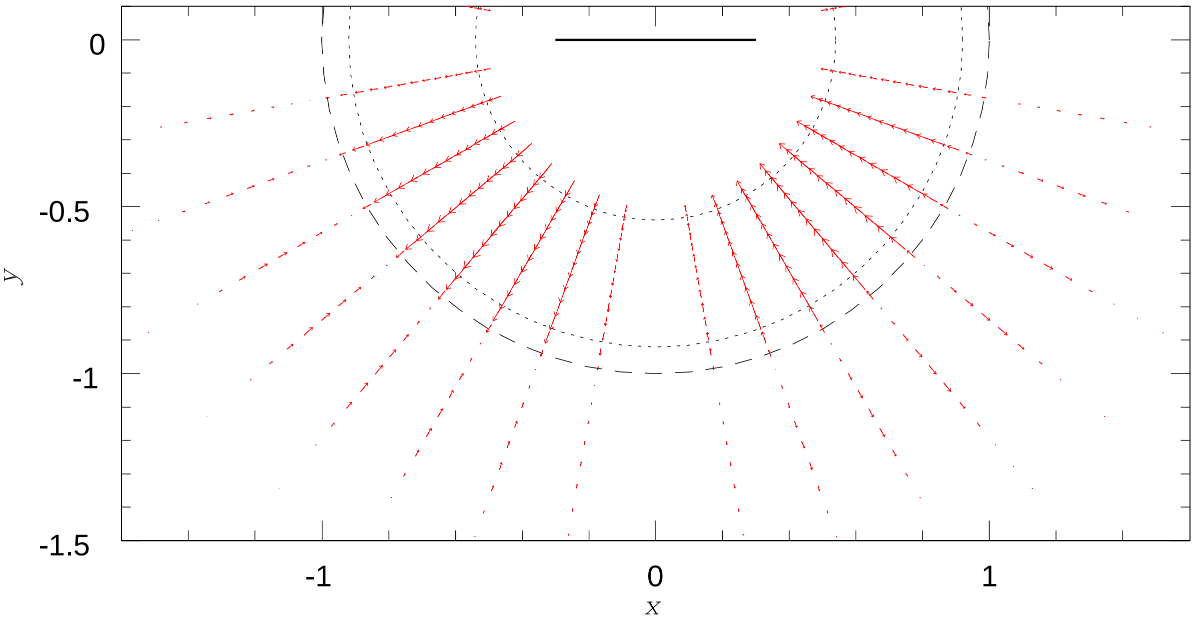

Figure 3.9: Mean radial velocities up to m=2. The bar is indicated by the solid line in the center and is supposed to rotate clockwise. The dashed line is the solar circle (also serving as unit length), dotted lines are co-rotation and outer Lindblad resonances.

Variations of the mean azimuthal velocity are also present, but here we have to deal with several perturbation effects, the dominant one for realistic cases being traditional axisymmetric asymmetric

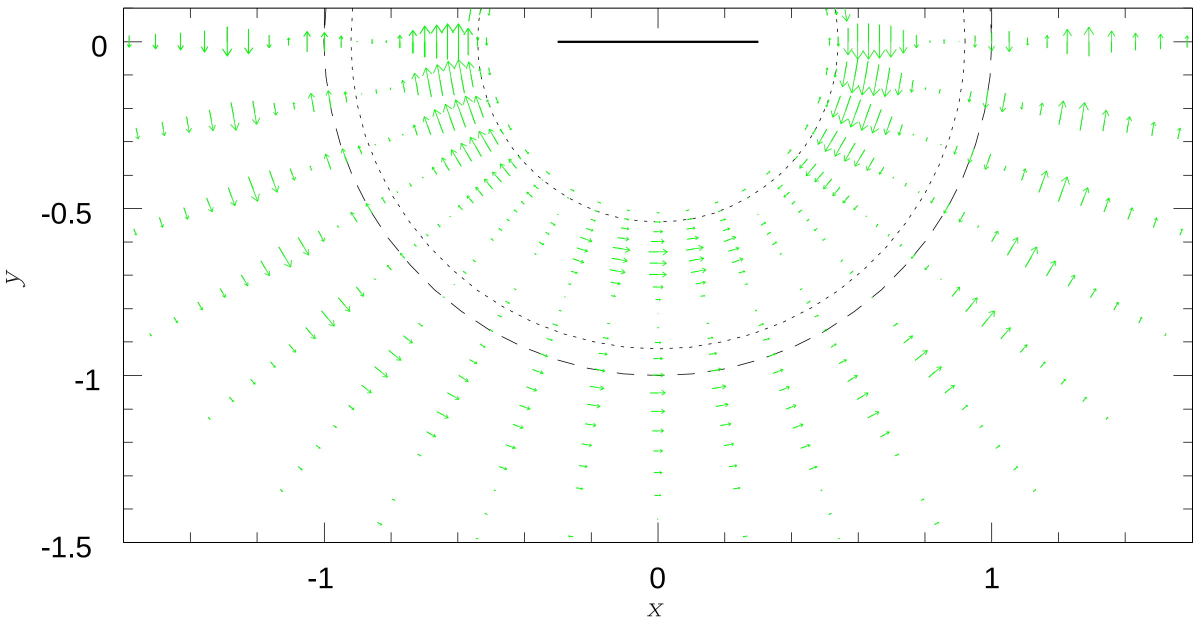

Figure 3.10: Modifications of tangential velocities up to m=2, not including asymmetric drift.

drift. We can construct a picture of the bar-induced $\bar{\mathbf{v}}$-modifications only (see Fig. 3.10) by subtracting $\bar{\mathbf{v}}$ in the undeveloped case before bar growth, thus also canceling asymmetric drift. However, this is, of course, impossible for real galaxies, where only the combination of circular speed (LSR motion), asymmetric drift, and bar induced drift is measurable (in principle). In observational data, the effect of asymmetric drift can be corrected for, as done by Dehnen & Binney 1998 [31], by calculating $\bar{v}$ for stellar populations with different velocity dispersions and extrapolating to vanishing dispersion. This approach, however, cannot be applied to the bar-induced perturbations in $\bar{v}$, since, as can be seen in Fig. 3.3, the relative magnitude of the bar-induced wiggle keeps constant at about 2%, independent of velocity dispersion. So, as long as only local measurements are available, there is no way to discern the bar-induced azimuthal velocity perturbations from variations in the background rotation curve, and so it will be rather hard to draw any observational constraints from the mean azimuthal velocities.

Our calculations show that for an equilibrium in a barred Milky Way, with bar orientation, strength and pattern speed consistent with other data, a vertex deviation of the size and direction as observed emerges naturally. Moreover, we also found that for dynamically cooler sub-populations, i.e. bluer or younger stars, the bar-induced vertex deviation increases in amplitude, very similar to the observed values.

This gives strong support for the hypothesis that the vertex deviation observed in the solar neighbourhood is predominantly caused by deviations from axisymmetry rather than from equilibrium. This explanation also naturally accounts for the fact that ℓ_v for young stars has the same direction as for old ones, which with the traditional explanation would be a chance coincidence.

The axis ratio of the (principal components of the) velocity dispersion tensor, σ_2^2/σ_1^2, is clearly affected by the central bar. In particular, values less than 0.5, Oort's value for a flat rotation curve, are possible (Oort's value is a *lower* limit for an axisymmetric galaxy, see section 3.2.3 and Evans & Collett 1993 [41], Dehnen 1999 [26]). This nicely fits to the values inferred from HIPPARCOS data (Dehnen & Binney 1998 [31]), which give $\sigma_2^2/\sigma_1^2 \sim 0.4$ for the old stellar disk.

Chapter 4

Further Studies of the Barred Model

In this chapter, we review some further studies we have done with our model. Frequently, we used the pure sampling here, without any evolution in the barred potential. First we will say some words on the asymmetric drift, which rather amounts to something like a consistency check. Then we will have some detailed discussion on the validity of the Oort relation, and finally we report on our attempts of constructing the Oort constants for our model.

4.1 Understanding the asymmetric drift

The value of the parameter D in Strömberg's relation (2.18) refers to the solar neighbourhood, of course, and D will in general depend on the position in the disk. In Fig. 4.1, we show again the mean tangential velocities in the unperturbed disk, i.e. before bar growth, for a variety of input dispersions. Using the (uu)-component of the velocity dispersion tensor of our unperturbed sample, we can construct the parameter D of Strömberg's relation, which we also show in Fig. 4.1. It turns out to be independent of the initial dispersion measure σ_0 and to be an inverse linear law $D = 1/(C_1 + C_2 R)$ in Radius R. A linear regression on the values yields $C_1 \approx -0.27 \pm 0.2$, $C_2 \approx 2.54 \pm 0.2$.

Turning to theory, we can derive from the Jeans equations the following expression for the asymmetric drift velocity (cf. Binney & Tremaine 1987 [11], sect. 4.2.1 (a)):

$$\frac{v_a}{\sigma_{uu}^2} = \frac{1}{2v_c}\left[\frac{\sigma_{vv}^2}{\sigma_{uu}^2} - 1 - \frac{\partial \ln(\rho\sigma_{uu}^2)}{\partial \ln R} - \frac{R}{\sigma_{uu}^2}\frac{\partial \overline{v_R v_z}}{\partial z}\right], \tag{4.1}$$

where ρ is the spatial density. Assuming that

- the last term induces no strong R-dependence, which probably holds to some degree. For a disk symmetric about the z = 0 plane it should vanish exactly.
- σ_{uu}^2 and ρ are both exponentials in the disk, so that $\partial \ln(\rho\sigma_{uu}^2)/\partial \ln R \propto R$, and finally,
- the shape of the velocity ellipsoid does not change very much so that $\sigma_{vv}^2/\sigma_{uu}^2 \approx$ const.,

we do indeed get an inverse linear law for D, independent of the dispersion magnitude. If we take a look at $1/D$ in the developed case after bar growth (Fig. 4.2), we find again some resonant structure, largely a reflection of those in v and σ_{uu}^2. It is getting sharper and at the same time growing in magnitude with decreasing velocity dispersion. Also, we find the now familiar phenomenon that with rising dispersion it is increasingly shifted to the outside.

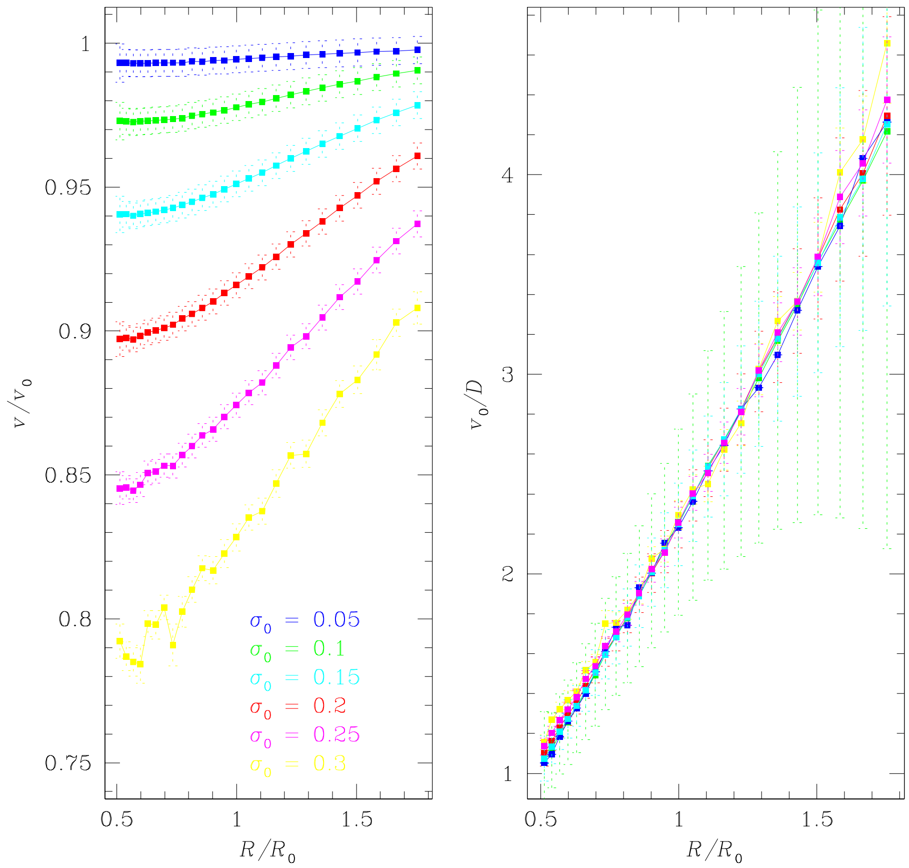

Figure 4.1: Asymmetric drift in one of our sampled models before bar growth. Left panel shows the mean tangential velocity for various input dispersions, right panel shows the inverse of the D-parameter of Strömberg's relation (2.18) reconstructed with the models dispersion tensor component σ_{uu}^2. Error bars for $\sigma_0 = 0.05$ are left out in the right panel, but are large. Errors are propagation errors from the bootstrap errors constructed in section 3.

4.2 Discussion of the dispersion ellipsoid axis ratio

As mentioned in the introduction, it is often claimed that[1] $\sigma_{vv}^2/\sigma_{uu}^2$ should equal the quantity given in eqn. (2.31). Thinking about it, we see that it is actually three different quantities which are identified by this:

- the axis ratio of the velocity dispersion ellipsoid, $\sigma_{vv}^2/\sigma_{uu}^2$, for which Dehnen & Binney 1998 [31] found a value of 0.4. In appendix F, we gain an expression for this from first principles.

- the quantity in (2.31), i.e. $-B/(A-B)$ for the Oort constants defined with the circular velocities according to eqns. (2.24) and (2.25), as long as such definition is meaningful in some way. This is exactly equal to $1/2$ for a flat rotation curve, $< 1/2$ for a declining and $> 1/2$ for a rising rotation curve.

---

[1] Writing $\sigma_{vv}^2/\sigma_{uu}^2$ means that we simply take the ratio of the corresponding dispersion tensor components, whereas in chapter 3 we diagonalized this tensor first. It is shown in appendix F that the difference is of second order only.

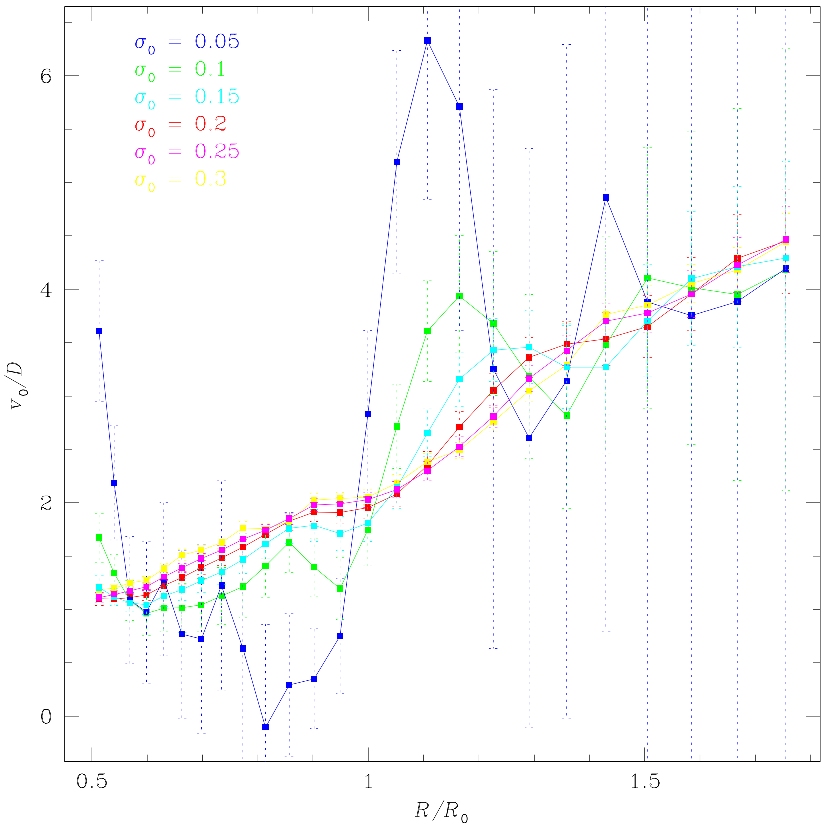

Figure 4.2: Same as right panel in Fig. 4.1, but for the developed case after bar growth.

- $-b/(a-b)$ for the true Oort constants defined using the actual stellar streaming motions. The observational situation (if smaller or larger than $1/2$) is not clear in this case.

In the general case, neither of these three needs to coincide with any other. In a non-axisymmetric galaxy, $-B/(A-B)$ might not even be definable (since circular velocities are not), and for $\sigma_{vv}^2/\sigma_{uu}^2$ and $-b/(a-b)$ there is absolutely no reason to equal each other, cf. eqns. (E.8), (E.9) and (F.14).

But even if we restict ourselves to the axisymmetric case, all three might be different. Indeed, we have then, from (E.8) and (E.9):

$$\frac{-b}{a-b} = \frac{1}{2}\left(1 + \frac{d\ln\bar{v}}{d\ln R}\right) \tag{4.2}$$

which is to be compared to expression (2.31) for $B/(A-B)$ and to expression (F.18) for $\sigma_{vv}^2/\sigma_{uu}^2$:

$$\frac{-B}{A-B} = \frac{1}{2}\left(1 + \frac{d\ln v_c}{d\ln R}\right) \tag{4.3}$$

$$\frac{\sigma_{vv}^2}{\sigma_{uu}^2} = \frac{1}{2}\left(1 + \frac{d\ln\bar{v}}{d\ln R} - \frac{\Delta_{\varphi\varphi\varphi}}{\bar{v}\sigma_{uu}^2} + \frac{1}{\rho R\bar{v}\sigma_{uu}^2}\frac{d}{dR}(R^2\rho\Delta_{RR\varphi})\right) \tag{4.4}$$

- $-b/(a-b)$ coincides with $-B/(A-B)$ only if we neglect the difference between $\bar{v}$ and v_c, i.e. the asymmetric drift. For a flat rotation curve, $-B/(A-B) = 1/2$ exactly, while we obtain using $\bar{v} = v_c - v_a(R)$

$$\frac{-b}{a-b} = \frac{1}{2} - \frac{R}{2\bar{v}}\frac{dv_a}{dR}, \tag{4.5}$$

and since v_a is a decreasing function of R, $-b/(a-b)$ will be larger than $1/2$.

- The difference between $\sigma_{vv}^2/\sigma_{uu}^2$ and $-b/(a-b)$ in the axisymmetric case is found in appendix F to consist of terms involving some third moments. As already stressed by Cuddeford & Binney 1994 [20], these are in no way negligible. This is also the problem with derivations such as in Binney & Tremaine 1987 ([11], sec. 4.2.1 (c)), where, apart from the disk being stationary and vertex deviation being negligible, it is named as a prerequisite that the velocity distribution needs to be symmetric in $v - \bar{v}$. This simply does not hold for realistic velocity distributions, and the mentioned third moments measure the extent of violation of this symmetry.
  The correction induced by the third moments is positive, so $\sigma_{vv}^2/\sigma_{uu}^2$ is still larger than $-b/(a-b)$.
- For this reason, $\sigma_{vv}^2/\sigma_{uu}^2$ is also different from $-B/(A-B)$.

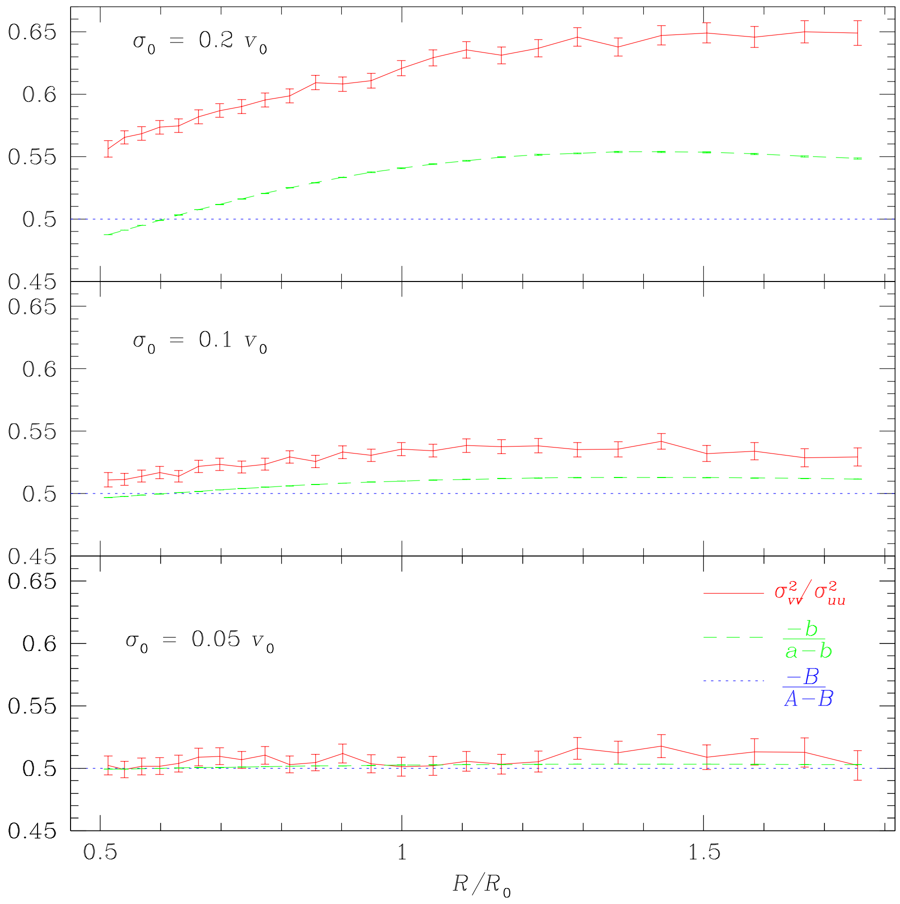

Figure 4.3: Comparison of quantities usually identified in the Oort relation. The values shown relate to our unperturbed model before bar growth, i.e. to an axisymmetric regime. The curves for $\sigma_{vv}^2/\sigma_{uu}^2$ are the same as the ones of the unperturbed model in Fig. 3.7. The quantitiy $-b/(a-b)$ is constructed according to (4.5) with $v_a = \sigma_{uu}^2(C_1 + C_2 R)$ using the values of section 4.1. Because of the flat rotation curve, $-B/(A-B) \equiv 1/2$ constantly.

Fig. 4.3 shows the three quantities for the unperturbed (axisymmetric) state before bar growth for our model with flat rotation curve: both $\sigma_{vv}^2/\sigma_{uu}^2$ and $-b/(a-b)$ are larger than $-B/(A-B) \equiv 1/2$.

The run of both curves is similar, but the first one is shifted upwards. So the effect of the third moment terms seems to be roughly constant in R and positive.

Regarding the behaviour with varying overall dispersion, we see the differences between the three curves vanish as dispersion gets smaller. Obviously, not only the asymmetric drift, but also the third moments get smaller with σ_0. However, we see that the dispersion must not be greater than $\sim 5\%$ of the rotation velocity for an equality to hold approximately.

Whether the Oort relation may be used in observational measurements for any of the quantities involved should thus depend on the dispersion of the stellar population used; as long as this is indeed small enough, it may be justified. However, this is only true as long as non-axisymmetries are excluded, and the fact that measurements of the dispersion axis ratio generally yield values $< 1/2$ which axisymmetric theory cannot explain must be taken as a clear hint that non-axisymmetries are important. We saw in section 3.2.3 that bar-induced variations of the axis ratio may generally be larger than all the axisymmetric effects, and that they also may yield values for $\sigma_{vv}^2/\sigma_{uu}^2$ smaller than $1/2$.

4.3 Oort constants

4.3.1 Determination of the Oort constants

We also tried to determine the Oort constants in our model. After some unsuccessful attempts we found that the best way to do this is to use eqn. (2.26). So we take the sample points lying within a certain distance interval around a position (R_0, φ_0) – representing the possible position of the Sun – and transform their velocity components according to eqn. (H.13) in appendix H. Eqn. (2.26) then suggests that we again apply a disrete Fourier transform of the kind of eqn. (3.15). For this, we assign the sample points to a number of bins in Galactic longitude ℓ as seen from (R_0, φ_0), and calculate mean values and standard deviations of v_d, v_ℓ for each bin. In order to improve the result, we employ some κ-σ-clipping, i.e. we iteratively exclude points which differ from the mean by more than a certain factor κ times the standard deviation σ. After that, we perform the Fourier transform on the mean values of v_d and v_ℓ. The Oort constants should then appear as the zeroth and second Fourier coefficients in this expansion, according to (2.26).

However, not taking proper care of asymmetric drift induces an $m = 1$ mode, and this is dominating the behaviour of v_d and v_ℓ as a function of ℓ, see Fig. 4.4. In order to see how this comes about, let us start from the transformation formula (H.13) of appendix H for v_d and v_ℓ and express them as functions of ℓ using eqns. (H.2) and (H.4). We assume an axisymmetric Galaxy with a flat rotation curve but we allow for asymmetric drift, so

$$v_R \equiv 0, \qquad v_\varphi(R) = v_0 - v_a(R), \tag{4.6}$$

where we approximate the asymmetric drift to first order in distance:

$$v_a(R) \approx v_{a0} + D_0 \cdot (R - R_0) \qquad \text{with} \qquad v_{a0} := v_a(R_0), D_0 := \left.\frac{\partial v_a}{\partial R}\right|_{R_0} \tag{4.7}$$

This yields then

$$v_{\rm los} = -v_{a0}\sin\ell + \underbrace{\frac{1}{2}\frac{v_0 - v_{a0} + D_0 R_0}{R_0}}_{\hat{=}\, a} d\sin 2\ell \tag{4.8}$$

$$v_\ell = \underbrace{-\frac{1}{2}\frac{v_0 - v_{a0} - D_0 R_0}{R_0}}_{\hat{=}\, b} d - v_{a0}\cos\ell + \underbrace{\frac{1}{2}\frac{v_0 - v_{a0} + D_0 R_0}{R_0}}_{\hat{=}\, a} d\cos 2\ell \tag{4.9}$$

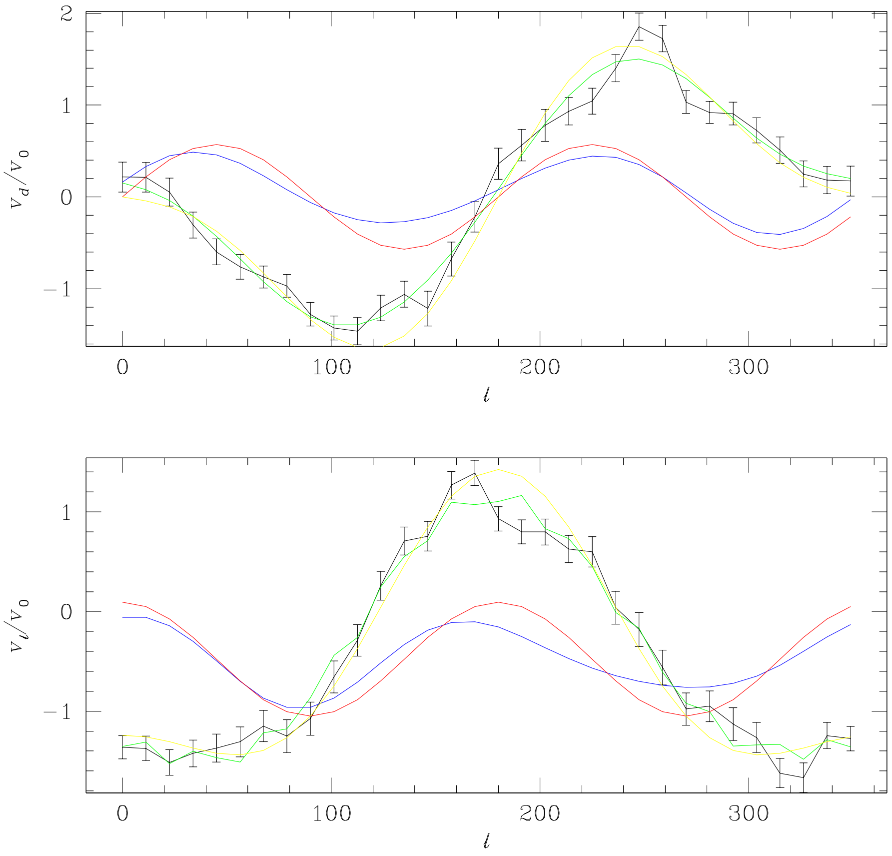

Figure 4.4: Mean velocities (in units of v_0) of the sample points lying in a ring around the presumed location of the Sun in the unperturbed model before bar growth. Upper panel shows line-of-sight velocity, lower panel the tangential component as a function of Galactic longitude ℓ. Also shown is a reconstruction of the data out of its first three Fourier components (*green curves*), the expectation for these curves according to eqn. (2.26) using some observational values for a and b (*red curves*), and how this is matched if the Fourier reconstruction leaves out the $m = 1$ terms (*blue curves*). Finally, we show the theoretical result eqns. (4.8) and (4.9) with values for v_{a0}, D_0 appropriate here (*yellow curves*).

As we can see, there are two effects: one is the appearance of the $m = 1$ terms, the other is a modification in the Oort constants. For the latter, the effects of the value and the gradient of the asymmetric drift will tend to cancel each other for b (remember $D_0 < 0, v_{a0} > 0$), whereas both will lead to an overestimation of a by $A = v_0/(2R_0)$. Therefore, the shift induced by asymmetric drift will be much greater for a than for b (Lewis 1990 [63]).

The $m = 1$ terms arise from using the "wrong" rest-frame velocity v_0 in eqn. (H.13), where rather $v_0 - v_{a0}$ should have been used as the correct LSR-velocity instead of v_0. Had we used eqn. (H.13) with $v_0 \longrightarrow v_0 - v_{a0}$, we would have arrived at expressions (4.8), (4.9) without the $m = 1$ terms. Nevertheless, if we simply ignore the $m = 1$ component, we can still use eqn. (2.26) to read off the Oort constants. That this is justified can be seen in that a reconstruction of the curve using only the zeroth and second moments matches up rather well with the expected curve according to (2.26) using the Feast/Whitelock values for a and b (red and blue curves in Fig. 4.4). We plotted relations

(4.8), (4.9) into Fig. 4.4 as well (yellow lines), the agreement of these curves with the simulation data showing that our analysis is correct.

4.3.2 Oort constants in the unperturbed sampling

In Fig. 4.5, we show the Oort constants determined in this way as a function of distance d, i.e. the radius of the ring used for calculation. Ideally, we should take the limit $d \longrightarrow 0$, but in practice we have to choose some appropriate value. As we can see in the figure, there is a slight variation with d, and since we know that in this axisymmetric case c and k should vanish, we can gain a feeling of the uncertainties involved. In particular, we see that we should choose d not too small. Evaluation was done around (R_0, φ_0), where the choice of φ_0 should not matter as long as we consider our axisymmetric sampling. Doing the evaluation for different values of φ_0 gives a measure of the error again.

What we can see in Fig. 4.5, above all, is that a differs considerably from the value determined by Feast & Whitelock (dotted lines in the figure), whereas b more or less agrees. Also, with smaller dispersion, values for a are rising, whereas those for b are essentially unchanged. This illustrates the fact that asymmetric drift affects a stronger than b. In contrast to observational values such as Feast & Whitelock, we have $|b| > a$ in our model, which is clear since $|b| - a = -(a+b)$ equals the gradient of the velocity curve (cf. eqn. (2.30); note that from eqns. (E.8) and (E.9), $-(a+b)$ continues to equal the gradient even if non-axisymmetries are taken into account), which is effectively rising due to asymmetric drift. However, in observational measurements it is rather common to find $|b| < a$ (see Kerr & Lynden-Bell 1986 [55]), indicating, as we have mentioned, a locally falling velocity curve. Thus, if observational determinations of the Oort constants are indeed affected by asymmetric drift, one would have to assume that the velocity curve intrinsically, i.e. with regard to the underlying Galactic potential, is even more strongly declining.

Olling & Dehnen 2003 [71] find $|b| > a$, but their values agree less with our predictions. Of course one can speculate that this is due to non-axisymmetric perturbations of the real Galaxy.

Regarding the spatial variability of the Oort constants, we repeated our evaluation (choosing $d = 0.06$, here and always hereafter) for several points (R, φ), again φ being irrelevant and providing error bars on its variation. The result is shown in Fig. 4.6. Both a and b show a decrease in absolute value with R, resulting primarily from the inverse R-dependence as $a \approx v_0/(2R) \approx -b$ in the roughest approximation. Whether the irregularities seen in the curve are artifacts of the sampling or have some meaning is not clear at this stage.

4.3.3 Oort constants in the perturbed state

Switching now to the bar-perturbed disks, we can follow the same program and determine the Oort constants as functions of position. This time, however, dependence on azimuth angle is also relevant. We show a selection of results in Fig. 4.7. Most remarkable is a range of negative k and c near the OLR radius at azimuths $\varphi \sim 30°$ for smaller velocity dispersions. This is in accordance with the negative c of -9.8 km/s/kpc which Olling & Dehnen (2003 [71]) have found in their determination of the Oort constants for the old stars (Olling & Dehnen did not determine k). We include their values in the figure here.

Perhaps also interesting in this case is the ratio $-b/(a-b)$. We found in section 4.2 that it should always be larger than $1/2$ in the outer disk of an axisymmetric galaxy (which it turns out to be for the a, b constructed above). In the bar perturbed disk, however, we find regions where it reaches well below $1/2$, see Fig. 4.8. Furthermore, we see that, unlike the axisymmetric case, the difference of

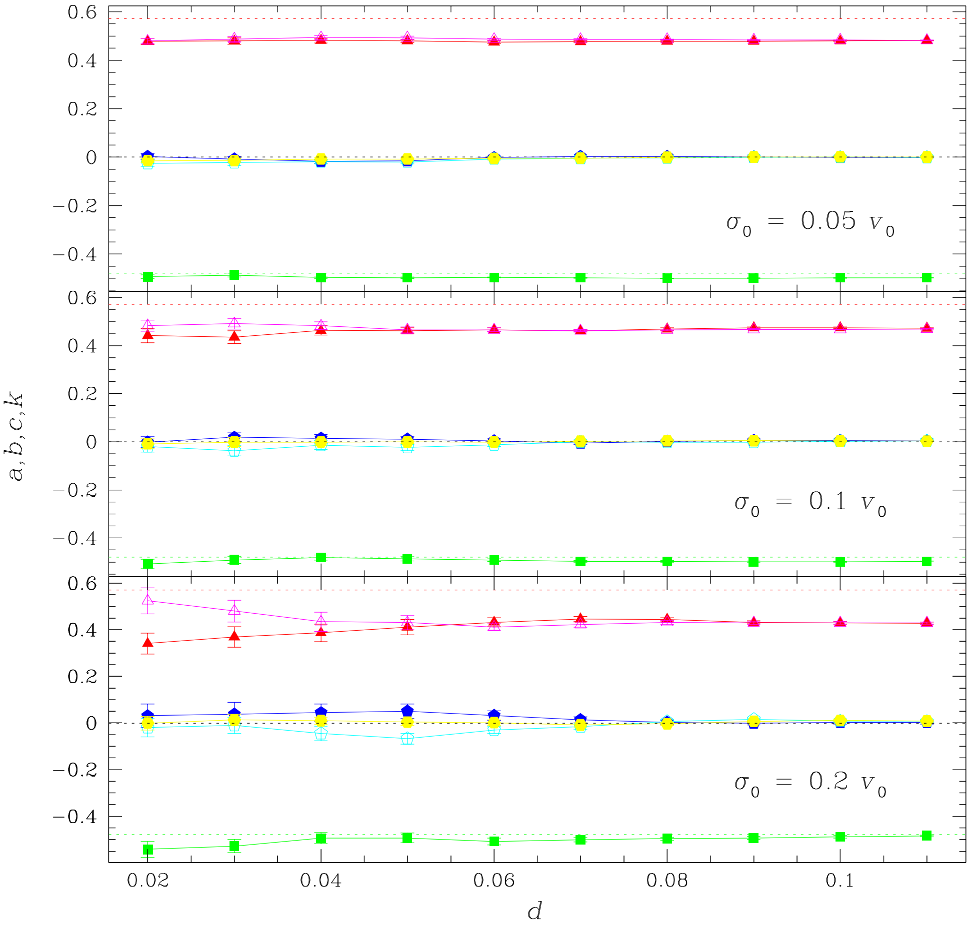

Figure 4.5: Oort constants at R_0 in the axisymmetric sampling as a function of distance d (in units of $R_0 = 8.5$ kpc) used for determining these as Fourier coefficients of line-of-sight velocity v_d or tangential velocity v_ℓ. Symbols are: a determined from v_d (*filled triangles, red*), or from v_ℓ (*open triangles, magenta*), b (*filled squares, green*), c determined from v_d (*filled pentagons, blue*), or from v_ℓ (*open pentagons, cyan*), k (*filled hexagons, yellow*). Scale on the vertical axes is in units of $\Omega_0 = 25.88$ km/s/kpc. Also shown are the Feast/Whitelock values for a and b (*dotted red and green lines*).

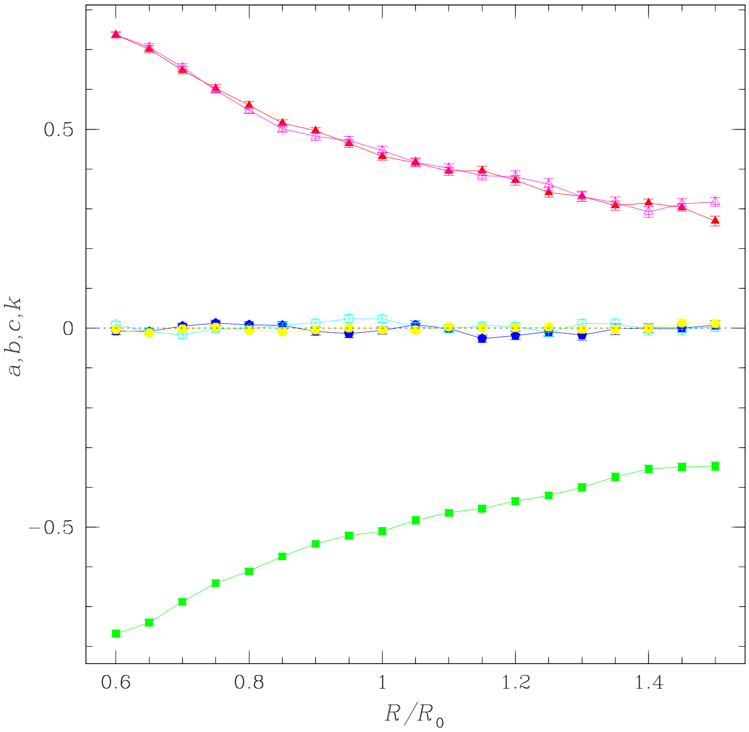

Figure 4.6: Spatial dependence of Oort constants in the axisymmetric case. Evaluation was done within a ring around $d = 0.06R_0$. Symbols and units as in Fig. 4.5.

$-b/(a-b)$ from $1/2$ does not decrease with velocity dispersion. The observational situation here is not clear: whereas e.g. the Feast & Whitelock values give $-b/(a-b) \approx 0.46$, Olling & Dehnen's values yield ≈ 0.52.

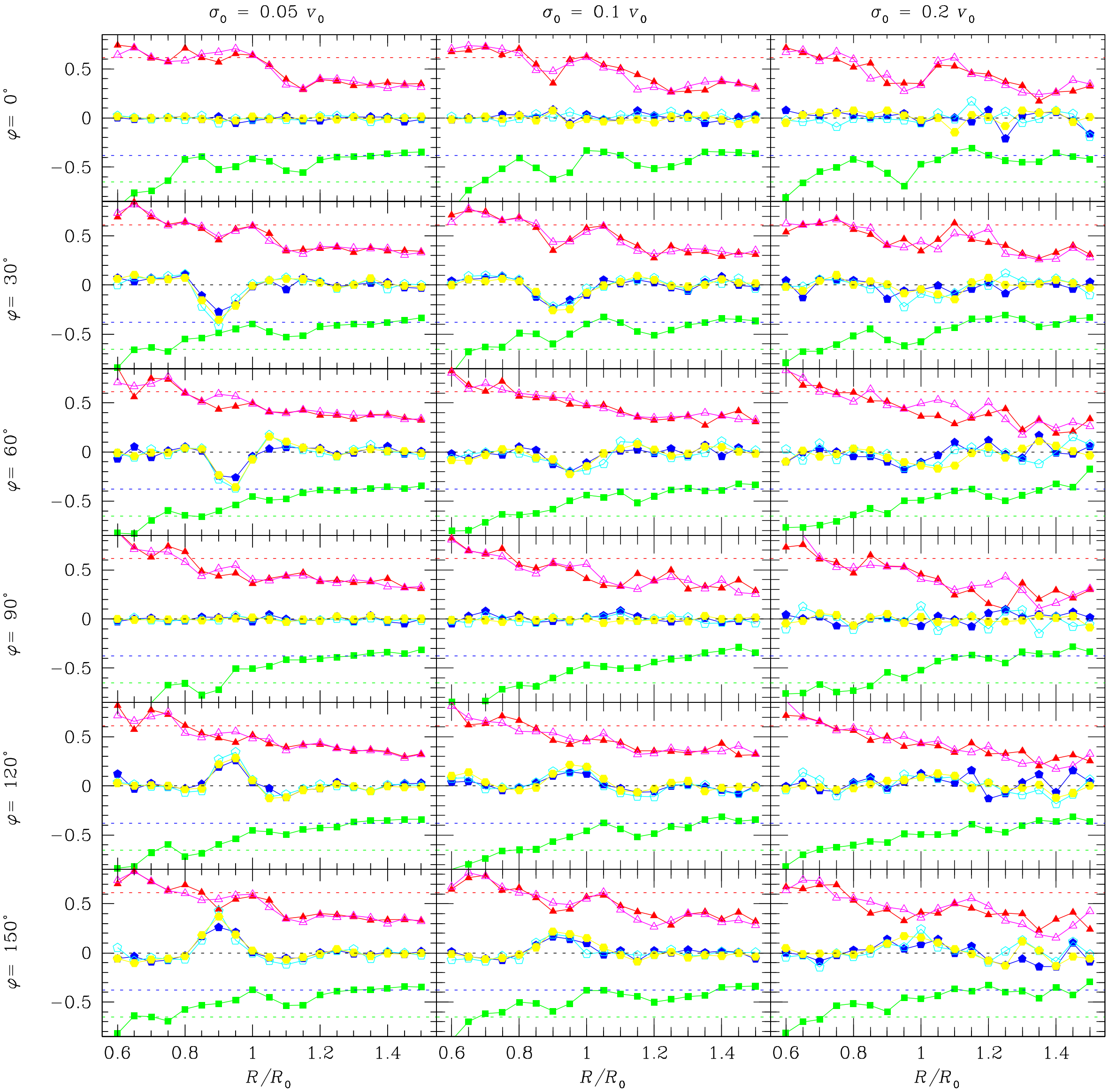

Figure 4.7: Oort constants in the developed case after bar growth as functions of Radius R for various azimuth angles φ and for three different velocity dispersions. Symbols as in Fig. 4.5. Also shown are the observational values for a, b, c that Olling & Dehnen 2003 [71] found for old stars (*red, green and blue dashed lines*).

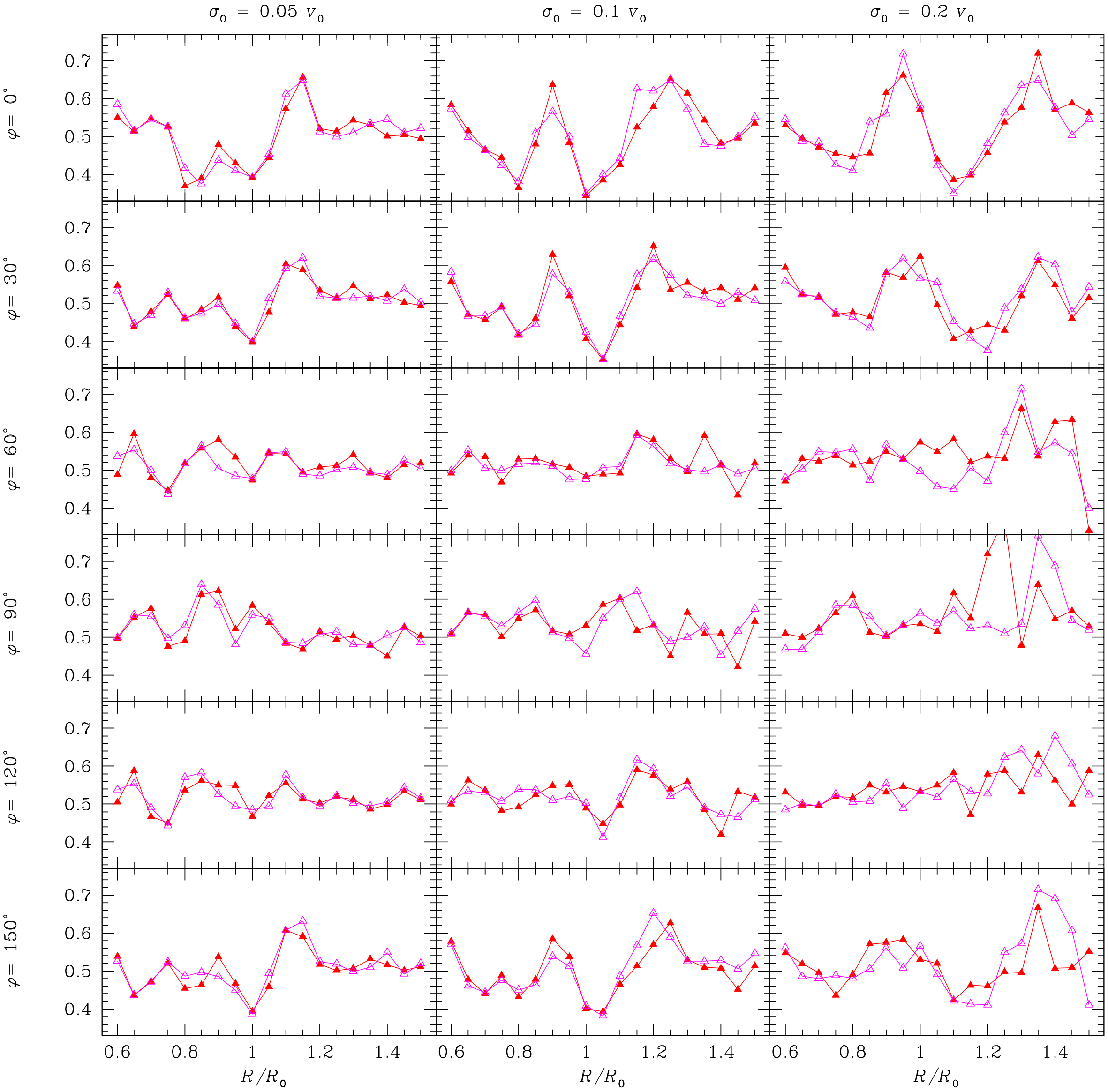

Figure 4.8: Oort constant ratio $-b/(a-b)$ formed from the values shown in Fig. 4.7. Again, filled red symbols use a obtained from v_d, open magenta symbols use a from v_ℓ.

Chapter 5

Influence of Spiral Structure

Since the disk of the Galaxy is not simply a smooth axisymmetric background but bears other structure as well, one has to ask how much our bar-induced effects will be covered by other effects. Most prominent, of course, are the spiral arms. In this chapter, we want to extend our model to include some spiral structure.

A recent study on the combined effects of bar and spiral perturbations on a stellar disk was done by Quillen 2003 [81].

5.1 General remarks on spiral arms

5.1.1 Origin and nature of spiral structure

Clearly, spiral arms cannot be made up of the same stars for long, because the differential rotation of the disk would wind them up within a short time. They are usually seen to be trailing with respect to the rotation of the galaxy, though the ambiguity of the inclination angle in the deprojection of a galactic disk in the sky procludes a determination of the orientation of the arms in general.

Early researchers thought that spiral structure is caused by interstellar magnetic fields. Today it is clear that these fields are by far not strong enough for this. Bertil Lindblad recognized that the spiral structure arises through the interplay of orbital kinematics and gravitational forces of the disk stars, but it was not before the works of C. C. Lin and F. Shu in the 1960s [64, 65] that this view gained wider acceptance. These authours regarded spiral structure as a wavelike, gravitationally supported density oscillation propagating through the differentially rotating disk. Winding-up would be avoided by the self-gravity of the arms. The formalism of density-wave theory developed from this (see e.g. Bertin & Lin 1996 [5] for a review) did not only allow to model spiral structure, but had further applications to disk stability theory as well. What remained unclear, however, was the extent to which spiral arms are density wave enhancements in the background stellar distribution, or whether they were predominantly gas-dynamical, thus being regions of enhanced star formation. Recent studies (Kranz et al. 2001 [56] and 2003 [57]) suggest that most spiral arms are true stellar density enhancements.

For a certain time after Lin and Shu's works, it was widely believed that spiral arms are quasi-stationary structures which are stable for many orbital periods and are rotating with a pattern speed of their own. This was thought to be supported by the appearance of "grand-design" spirals with highly symmetric arms. For these, the regularity of the spiral structure seems to require some global process involving the entire disk. Today, however, the origin of spiral arms is again less clear, and probably different scenarios apply in different cases. There are theories of chaotic spiral arm formation (see the review by E. Athanassoula 1984 [2]), where the arm fragments are more or less short-lived and spatially limited phenomena caused by local processes, such as self-propagated star formation. This may apply to spirals with a flocculent complexion where the spiral arms appear irregular and fragmented, and cannot be followed for more than some fraction of a circle individually. On the other hand, for the grand-design spirals the spiral arms appear in many cases to be triggered externally, by tidal interaction with a satellite galaxy, or through a central bar.

Aside from an amplitude characterizing the strength of the spiral arms, an important parameter describing the shape of the spiral structure is the pitch angle p, i.e. the angle between the arm tangent and tangential direction. The simplest mathematical model of spiral arms is that of a logarithmic spiral, where lines of constant phase are given by $\varphi \propto \ln R$, which is a reasonable approximation for observed spirals.

5.1.2 Spiral structure of the Milky Way

Various tracers can be used for probing the spiral arm structure of the Milky Way:

- (ℓ-$v_{\rm los}$)-plots[1] of CO radio emission, as characteristic for molecular clouds. See Dame et al. 2001 [21] for a recent survey.
- (ℓ-$v_{\rm los}$)-plots of HI 21 cm emission, see e.g. Hartmann & Burton 1997 [53].
- spatial distribution of nearby young stars as indicated by Cepheids, OB-associations and HII regions
- decomposition of COBE maps (e.g. Drimmel & Spergel 2001 [34]), i.e. primarily the dust emission in the far infrared
- modelling the free electron density from the dispersion measure of pulsar signals (Taylor & Cordes 1993 [92])

While the tangents of the spiral arms are rather well-determined, it is usually much less certain how to connect the tangents. From (ℓ-$v_{\rm los}$)-plots, it is in principle possible to construct the position of the features in the Galactic plane, at least up to an intrinsic ambiguity inside the solar circle. Due to crowding in velocity space, however, tracing of individual arm segments is possible largely only outside or shortly inside the solar circle.

A classical study in this field is by Georgelin & Georgelin 1976 [47] who used HII data to constrain the spiral arms. Their result was a four-armed structure consisting of two major and two minor arms. In addition, the Sun happens to lie roughly inside the so-called Orion-Cygnus-arm, which is interpreted as a mere local interarm feature. Regarding the proper spiral arms, the Sun is lying roughly in the middle of two adjacent arms. Pitch angles of the arms were found by Georgelin & Georgelin to be approximately 12°. Taylor & Cordes 1993 [92] in their study of the free-electron density in the Milky Way incorporated some minor modifications to this picture, originally proposed by Downes et al. 1980 [32] and Caswell & Haynes 1987 [16]. Their picture of the Galactic spiral arms, see Fig. 5.1, is the most frequently reproduced since then.

Vallee 2002 [93] gives an overview of recent developments: most authors cling to a number of four spiral arms, though values for the pitch angle vary widely from about 6° to 17°. Drimmel 2000 [33] and Drimmel & Spergel 2001 [34] fitted spiral models to infrared emissions as measured by COBE/DIRBE. They suggested a four-armed structure for the dust emission in the far infrared, while

---

[1] Density plots of line-of-sight velocity $v_{\rm los}$ vs. Galactic longitude ℓ.

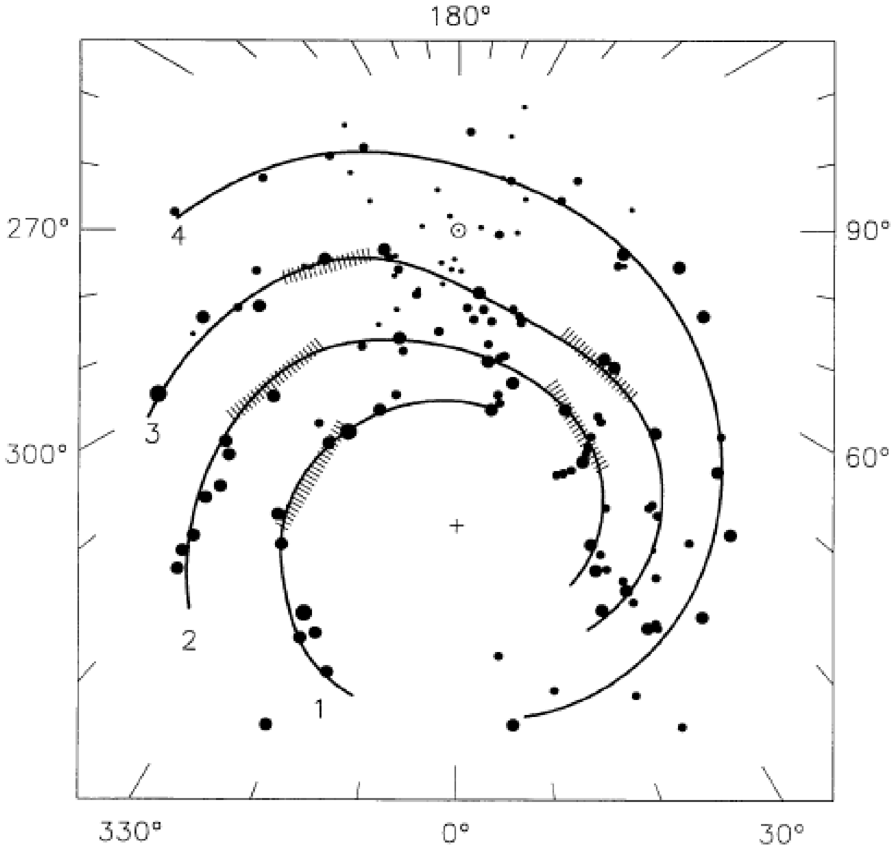

Figure 5.1: Spiral arm structure of the Milky Way. Circles represent HII regions, hatched areas correspond to the directions of spiral arm tangents as traced by the thermal continuum and neutral hydrogen emission. 1 – Norma arm, 2 – Scutum-Crux arm, 3 – Sagittarius-Carina arm, 4 – Perseus arm. Taken from Taylor & Cordes 1993 [92].

the NIR emission, which is probably due to older stars, can equally well be fitted by a two-armed spiral pattern. From external galaxies it is known (Seigar & James 1998 [86]) that spiral structure in the K band often bears little resemblance to the one seen in the visible, and frequently consists of two-armed modes. So this could be taken to suggest that stellar and gas dynamical processes excite different kinds of spiral modes.

5.2 Including spiral structure in the model

While in the cases of the bar and galactic background we specified a model potential directly, this would probably not be sufficient here. Instead, we take a simple model for the spiral density structure and solve for the corresponding potential. This is one step towards self-consistency, although we cannot yet expect our resulting particle distribution to reflect the input spiral density.

Kalnajs 1971 [54] (see also Binney & Tremaine 1987 [11]) has given a theory of how to calculate potentials of flat disks which is especially suitable for spiral structure, since it uses Fourier-type expansions into logarithmic spiral waves. In terms of the new radial coordinate

$$u = \ln R, \tag{5.1}$$

the potential of a flat distribution of matter $\rho(R,\varphi,z) = \delta(z)\Sigma(R,\varphi)$ can be written within the symmetry-plane as follows:

$$\Phi(R,\varphi) = -\frac{G}{\sqrt{R}}\int_{-\infty}^{\infty} du' \int_0^{2\pi} K(u-u',\varphi-\varphi')e^{3u'/2}\Sigma(e^{u'},\varphi')d\varphi', \tag{5.2}$$

where the integration kernel K is

$$K(u-u',\varphi-\varphi') = \frac{1}{\sqrt{2(\cosh(u-u') - \cos(\varphi-\varphi'))}}, \tag{5.3}$$

which has a nice translation symmetry in the (u,φ)-plane. Kalnajs used this to develop a Fourier decomposition of a disk into logarithmic spiral waves. However, we found it easier to calculate (5.2) directly.

The spiral structure density modification is taken to be a logarithmic spiral

$$\Sigma_{\text{spir}}(R,\varphi) = \delta_{\text{spir}}\Sigma_0 e^{-R/R_\Sigma} f(R)\cos(ku(R) - m\varphi) \tag{5.4}$$

with the same exponential decline as the background disk (3.2) and an amplitude δ_{spir} relative to its strength Σ_0. The radial wave number parameter k is related to the pitch angle p by

$$k = \frac{m}{\tan(p)} \tag{5.5}$$

and m is the number of spiral arms. $f(R)$ is some additional cut-off function, giving zero outside some interval $[R_{\text{cut}}^{\text{low}} - \Delta R_{\text{cut}}^{\text{low}}, R_{\text{cut}}^{\text{upp}} + \Delta R_{\text{cut}}^{\text{upp}}]$, unity inside some smaller interval $[R_{\text{cut}}^{\text{low}} + \Delta R_{\text{cut}}^{\text{low}}, R_{\text{cut}}^{\text{upp}} - \Delta R_{\text{cut}}^{\text{upp}}]$, and which is continuous up to its second derivative. We use expressions similar to (3.6) in the transition zones.
This structure is finally set rotating by the substitution $\varphi \to (\varphi + \Omega_{\text{spir}}t)$.

It turns out that for this density, the φ-integration in (5.2) can be done analytically, so that there is only one integral left for numeric computation. For details see Appendix G.

5.2.1 Strength of the spiral structure

In the first part of the work (section 3), we fixed the length and time scale of our model by setting $R_0 = 1$ and $v_0 = 1$. So far, we have not done so for the mass scale, but this is becoming necessary now. We have to adjust the strength of our spiral potential relatively to the other potentials.

We do this by the following considerations: The axisymmetric background potential (3.4), causing the more or less flat rotation curve, is a superposition of the potential of the disk and the dark matter halo. It seems unlikely that the contribution of the disk to the rotation velocity near the solar circle is less than $\eta = 50 - 80\%$. If we take the disk to be purely exponential in density as in (3.2) and neglect for a moment the bar and spiral parts, its contribution to the rotation velocity can be calculated by (see for example Binney & Tremaine 1987 [11])

$$v_{c,\text{disk}}^2 = 4\pi G\Sigma_0 R_\Sigma\, y^2(I_0(y)K_0(y) - I_1(y)K_1(y)), \tag{5.6}$$

where $y = R/(2R_\Sigma)$, and I_n, K_n are modified Bessel functions of the first and second kind. In this way, equating $v_{c,\text{disk}}$ to ηv_0, we find out how to relate the disk density to the potential.

$\Delta m_K [mag]$	K	V	δ_{spir}
0.13	1.127	0.127	0.060
0.15	1.148	0.148	0.069
0.20	1.202	0.202	0.092
0.25	1.259	0.259	0.115
0.30	1.318	0.318	0.137
0.35	1.380	0.380	0.160
0.40	1.445	0.445	0.182
0.45	1.514	0.514	0.204
0.50	1.585	0.585	0.226
0.60	1.738	0.738	0.269
0.70	1.905	0.905	0.312
0.80	2.089	1.089	0.353
0.90	2.291	1.291	0.392
1.00	2.512	1.512	0.431
1.10	2.754	1.754	0.467
1.20	3.020	2.020	0.502
1.30	3.311	2.311	0.536
1.40	3.631	2.631	0.568
1.50	3.981	2.981	0.598
1.60	4.365	3.365	0.627
1.70	4.786	3.786	0.654
1.80	5.248	4.248	0.680
1.90	5.754	4.754	0.704
2.00	6.310	5.310	0.726

Table 5.1: Luminosity contrasts in magnitudes, corresponding flux and density ratio K and spiral structure amplitude δ_{spir}. Also listed is the corresponding variation in surface brightness $V = (\Sigma_{\text{max}} - \Sigma_{\text{min}})/\Sigma_{\text{min}}$ as used by Rix & Zaritsky 1995 [84].

What remains to be done is to estimate the amplitude of the spiral arm density variations relative to the disk density. There is hardly a way to determine this from observations in our own galaxy. Measurements on external galaxies, for example Rix & Zaritsky 1995 [84], found azimuthal variations in surface density $V = (\Sigma_{\text{max}} - \Sigma_{\text{min}})/\Sigma_{\text{min}}$ of order unity, corresponding to $\delta_{\text{spir}} = V/(V+2) \approx 0.33$. On the other hand, Elmegreen et al. 1999 [38] found for rather flocculent galaxies arm-interarm contrasts in surface brightness in the K band of $\Delta m_K = 0.13 - 0.35$ mag. In the case of grand design galaxies with prominent spiral arm structure the value could be even as high as $\Delta m_K = 0.44 - 2$ mag. This corresponding flux ratios are $K = 10^{0.4 \Delta m_K}$, which we will also identify with the matter density ratio of this regions. Our model parameter δ_{spir}, being the amplitude of our spiral arm pattern, can then be taken[2] to be $\frac{K-1}{K+1}$ (see Elmegreen & Elmegreen 1984 [39]), or roughly $(K-1)/2$ if $K-1$ is small. Table 5.1 lists some values for the quoted range of luminosity contrasts. For the following, we assume that we can use a $\delta_{\text{spir}} \lesssim 0.2$, which would be sufficient to include the galaxies examined in Kranz et al. 2003 [57, 58]. With our standard choice for the bar strength, $\delta_{\text{spir}} = 0.1$ would correspond to about 25% of the bar's quadrupole strength near the solar circle (judging from the maximal gradient of the spiral potential near the solar circle).

For our simulations we try different values for δ_{spir} in the range of 0.1 to 0.2.

---

[2] Arm and interarm mass densities in our model are $\Sigma_0 + \delta_{\text{spir}}\Sigma_0$ and $\Sigma_0 - \delta_{\text{spir}}\Sigma_0$, respectively, so their ratio is $K = (1+\delta_{\text{spir}})/(1-\delta_{\text{spir}})$, which solves to $\delta_{\text{spir}} = (K-1)/(K+1)$.

5.2.2 Other spiral parameters

Literature values for the pitch angle p vary from 6° to 20° (Vallee 2002 [93]). Given m and p, the interarm distance S at radius R is given as

$$S = R \cdot \left(e^{\frac{2\pi}{m} \tan p} - 1 \right) \tag{5.7}$$

We assume a constant pattern speed for the spiral structure, which is not necessarily correct. For the size of this pattern speed, most of the newer investigations (Amaral & Lépine 1997 [1], Mishurov & Zenina 1999 [69]; useful as a review on this question is Shaviv 2003 [88], who postulates climatological impacts of spiral arm passages) find values in the range of $\Omega_s = (17 - 30)$ km/s/kpc, so that the Sun is not very far from spiral co-rotation, whereas early works on the subject assumed values in the range $10 - 14$ km/s/kpc. We consider two possibilities: either we take the bar OLR equal to the spiral co-rotation, or the bar co-rotation equal to the spiral ILR. This implies rotation velocities of the order of either 28 or 14 km/s/kpc, respectively.

A further parameter of the spiral model is its phase. Since we did not really specify the position of the Sun, we do not have a phase with respect to the Sun, but of course we have the relative phase between spiral pattern and the bar.

5.2.3 Evaluation of results

We now repeat the simulations as for the bar case, i.e. we calculate the motion of our distribution function sample while adiabatically switching on the bar and spiral potential. Unless the rotation frequencies of the spiral and bar patterns coincide, we no longer have a time-independent potential in a co-rotating frame, and there is no longer any conserved quantity as the Jacobi energy. However, the total potential still shows a periodicity, with period $T_{\text{rel}} = 2\pi / |\Omega_b - \Omega_{\text{spir}}|$.

It seems that our simple method of taking snapshots of the velocity distribution at certain times is not sufficient, but we should also keep track of the time evolution. We do this, but we restrict ourselves to a region around the solar circle in order to keep the amount of data manageable. In this region, we follow the evolution in very small timesteps for one joint period T_{rel}. In addition, we also take the usual snapshots, for the entire outer galaxy, where, this time, we have to take care to choose the right time for the snapshots. Since we have seen that the Sun lies, apart from the Orion-Cygnus interarm structure, more or less in the middle between two adjacent spiral arms, we should take time points where the relative phase of spiral structure and bar is such that the proposed location of the Sun of trailing about $\varphi_\odot = 30°$ behind the bar is lying at a spiral density minimum. The condition for this is

$$t_n = \frac{1}{|\Omega_{\text{rel}}|} \left(\frac{(2n+1)\pi}{m} - \varphi_\odot \right), \tag{5.8}$$

where $\Omega_{\text{rel}} = \Omega_{\text{spir}} - \Omega_b$ is the relative rotation frequency of bar and spiral pattern.

5.3 Results

We had to reduce integration times for the spiral models, i.e. although the time allowed for switching on bar and spiral structure was the same as in the pure bar models, time snapshots were taken earlier after their completion. The same is true for the time development observations which were done at similar times. Therefore, there may be transient features in the results here, which we did not have in section 3.2, and which would die out if we let the simulation run longer. However, because of the spiral perturbation, we would never reach a static distribution anyway.

5.3.1 Time snapshots

Results of our usual analysis using snapshots at a fixed time are shown in Figs. 5.2 to 5.5. Since the spiral structure destroys the symmetry requirements discussed in section 3 both sine and cosine coefficients may be excited for any mode. Such excitations can clearly be seen although some of them may as well be transients, because of the shorter development time.

However, the bar-induced features are still discernible, including the washed-out poles in the cosine coefficient of $\bar{u}$ and the two-fold feature in the sine coefficient of $\bar{v}$, see Fig. 5.3. All in all, comparing Figs. 5.2 to 5.5 to Figs. 3.3 and 3.4, we find that the differences and thus the effects of spiral arms are rather minuscule.

Regarding the $m = 0$ components as in Fig. 5.2, we see major differences to the bar-only case (Fig. 3.3) only in the radial velocity component $\bar{u}$ and possibly in the off-diagonal dispersion component σ^2_{uv}, particularly for the smaller dispersions. Apart from that, the features we found in section 3 are still here: the bump in $\bar{v}$ outside of the bar OLR, moving closer towards it with decreasing dispersion while at the same time getting stronger; a wiggling feature in surface density Σ; similar features in the dispersion components.

Essentially the same is true for the $m = 2$ components (Fig. 5.3): we see the familiar pole in the sine of $\bar{u}$ and the two-fold feature in the cosine of $\bar{v}$. Surface density and dispersion components are also very similar to the bar-only case. The situation changes very little in the case of the four-armed spiral (Figs. 5.4 and 5.5).

On the other hand, if we regard a spiral-only model, where the bar strength is set to zero (Figs. 5.6 and 5.7), we find indeed that there are only very weak perturbations at all. Of course, they do not bear resemblance to our bar features.

5.3.2 Time evolution

We followed the time evolution of our velocity moments over the period of the relative rotation frequency of bar and spiral pattern, which is the time we expect a periodicity for. This is $T_{\text{rel}} = 2\pi/|\Omega_b - \Omega_{\text{spir}}|$, as mentioned above. We present some examples of results in Figs. 5.8 to 5.10.

In a first series we regarded the time development in a system co-rotating with the bar (Fig. 5.8 for a two-armed spiral, Fig. 5.9 for a four-armed). We can see several phenomena:

- oscillations
- an underlying drift
- transients, e.g. various peaks around time $t \approx 28$.

In order to single out the drift, we performed the same development for a bar model without spiral arms (Fig. 5.10). We find the same underlying drift but no oscillations. Of course, the transients cannot be reproduced either.

Since our frame of reference is still the one co-rotating with the bar, we expect the number of oscillations seen during one relative period to be the number of spiral arms. This is roughly the case. So the oscillations we see in the $m = 2$ components should be a reflection of the spiral potential. In a self-consistent model, the resulting density contrast should equal that used for constructing the potential, and the first one can for a two-armed spiral be read off from the behaviour of the $m = 2$ component in Fig. 5.8 to be $\sim 0.028 \pm 0.002$ (note that we cannot read this off from the $m = 2$ component in Fig. 5.3 because bar contributions are included there). Compared with the value used

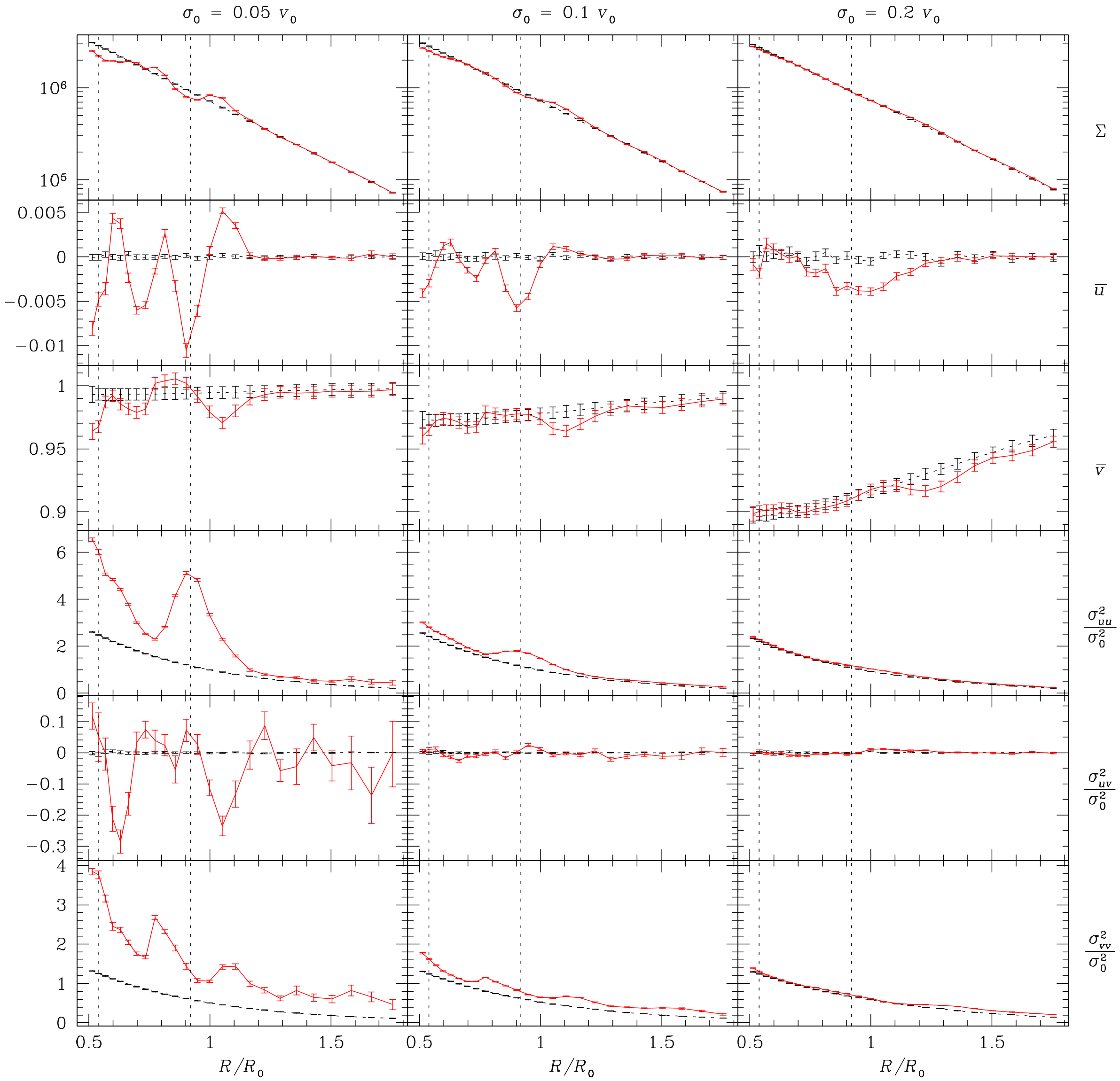

Figure 5.2: Same as Fig. 3.3 for model with two spiral arms with pitch angle 6° and strength $\delta_{\rm spir} = 0.1$

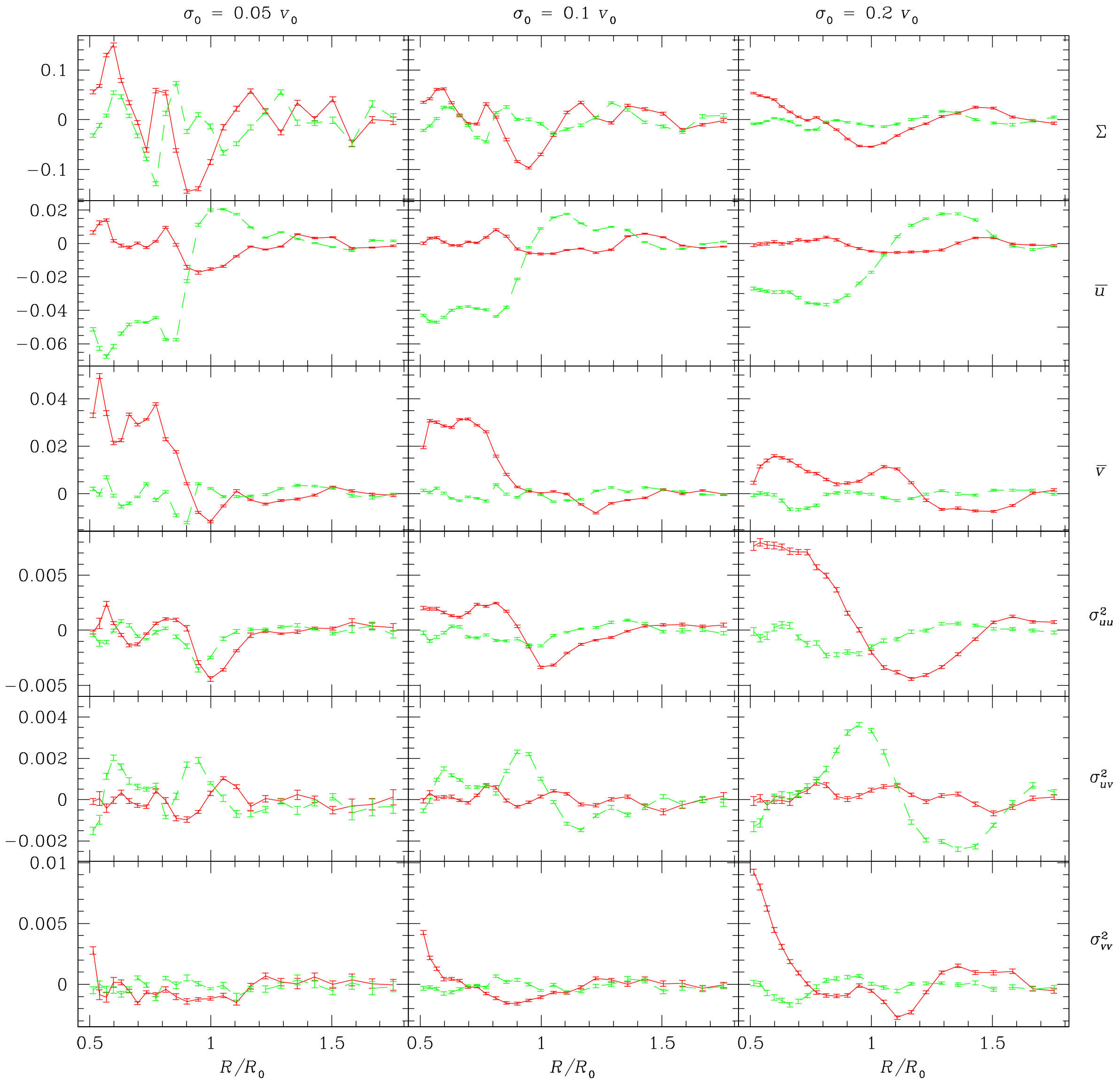

Figure 5.3: Same as Fig. 3.4 for the model of Fig. 5.2.

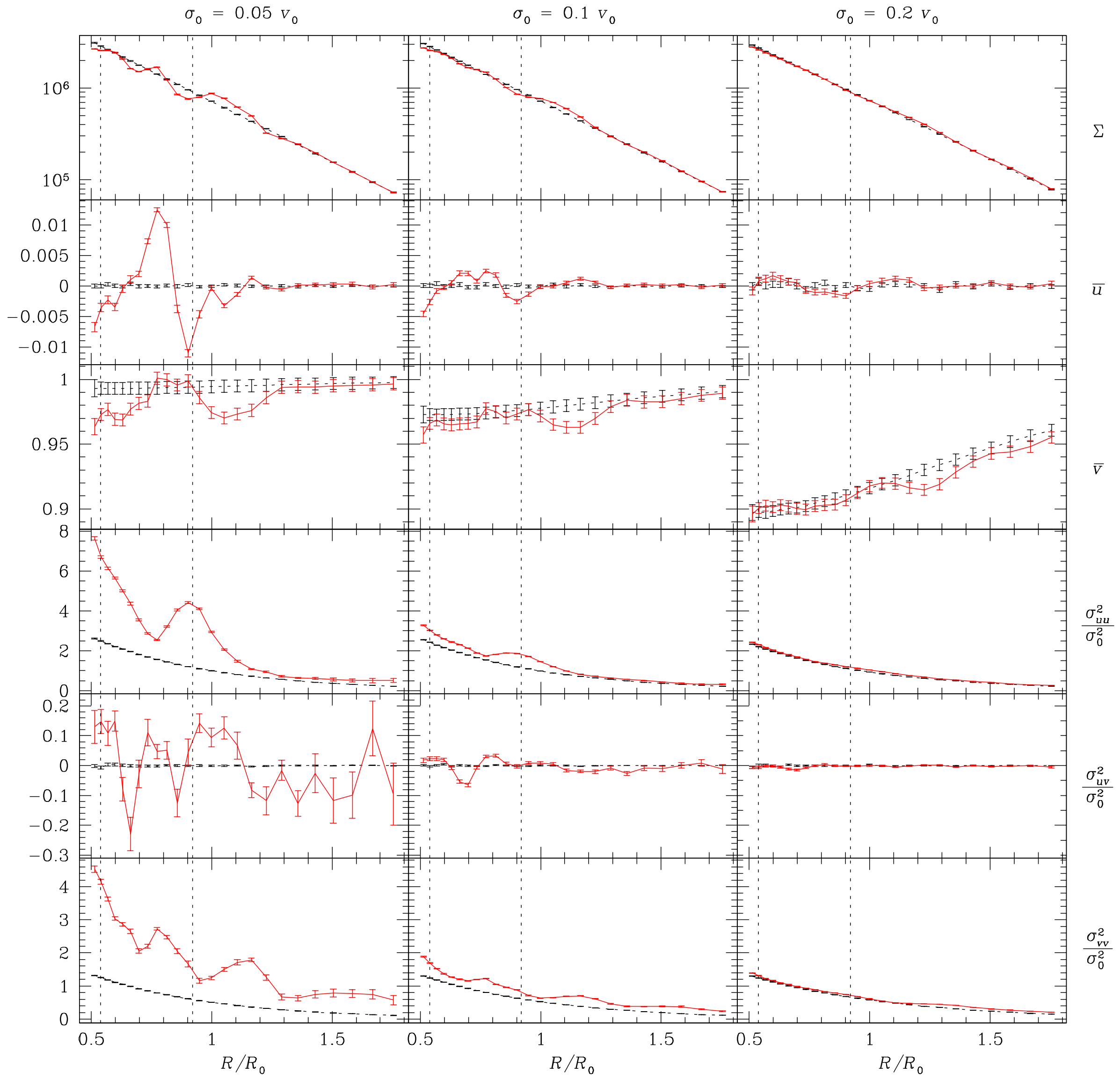

Figure 5.4: Same as Fig. 5.2 but for four-armed spiral.

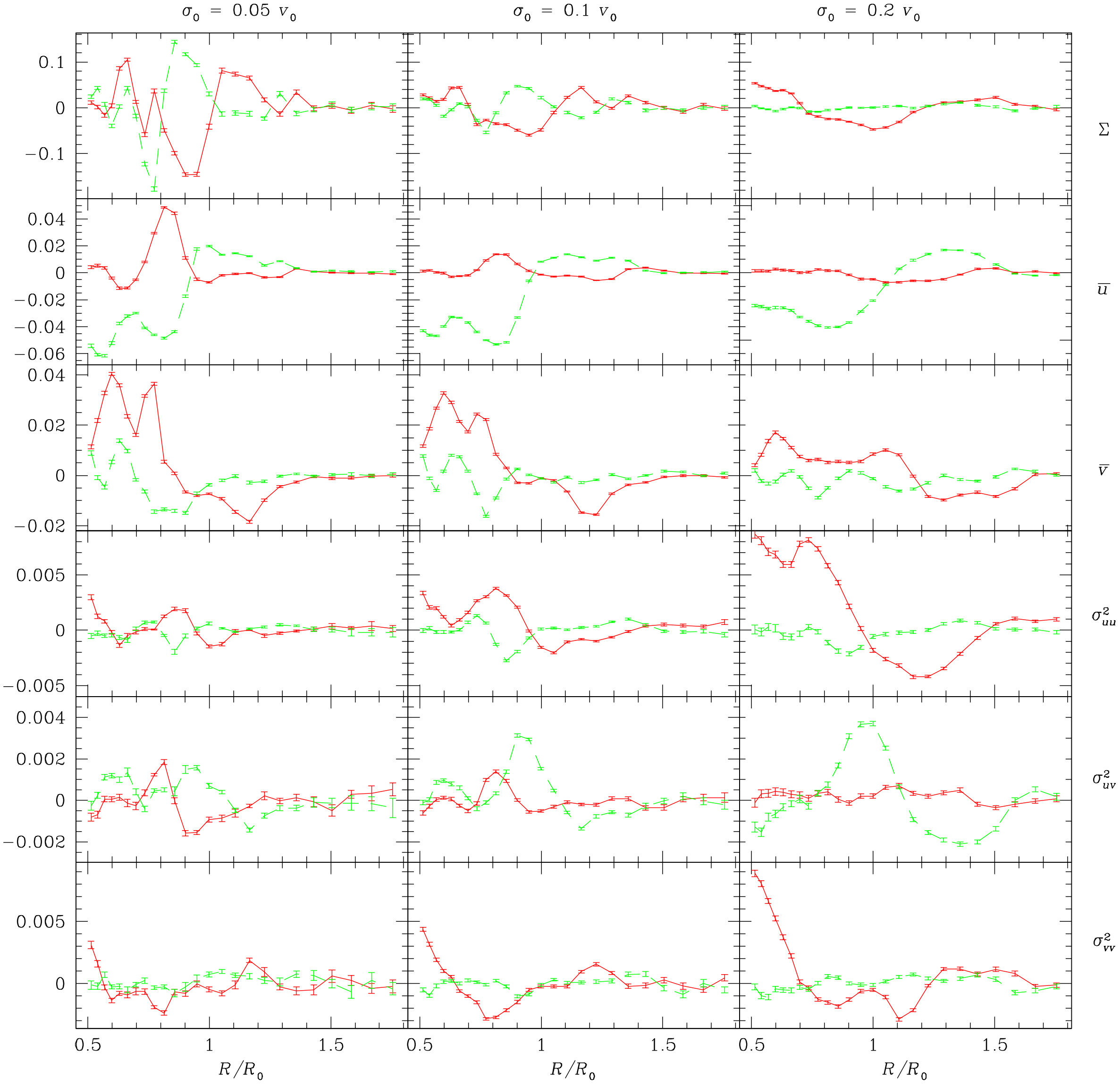

Figure 5.5: Same as Fig. 5.3 but for four-armed spiral.

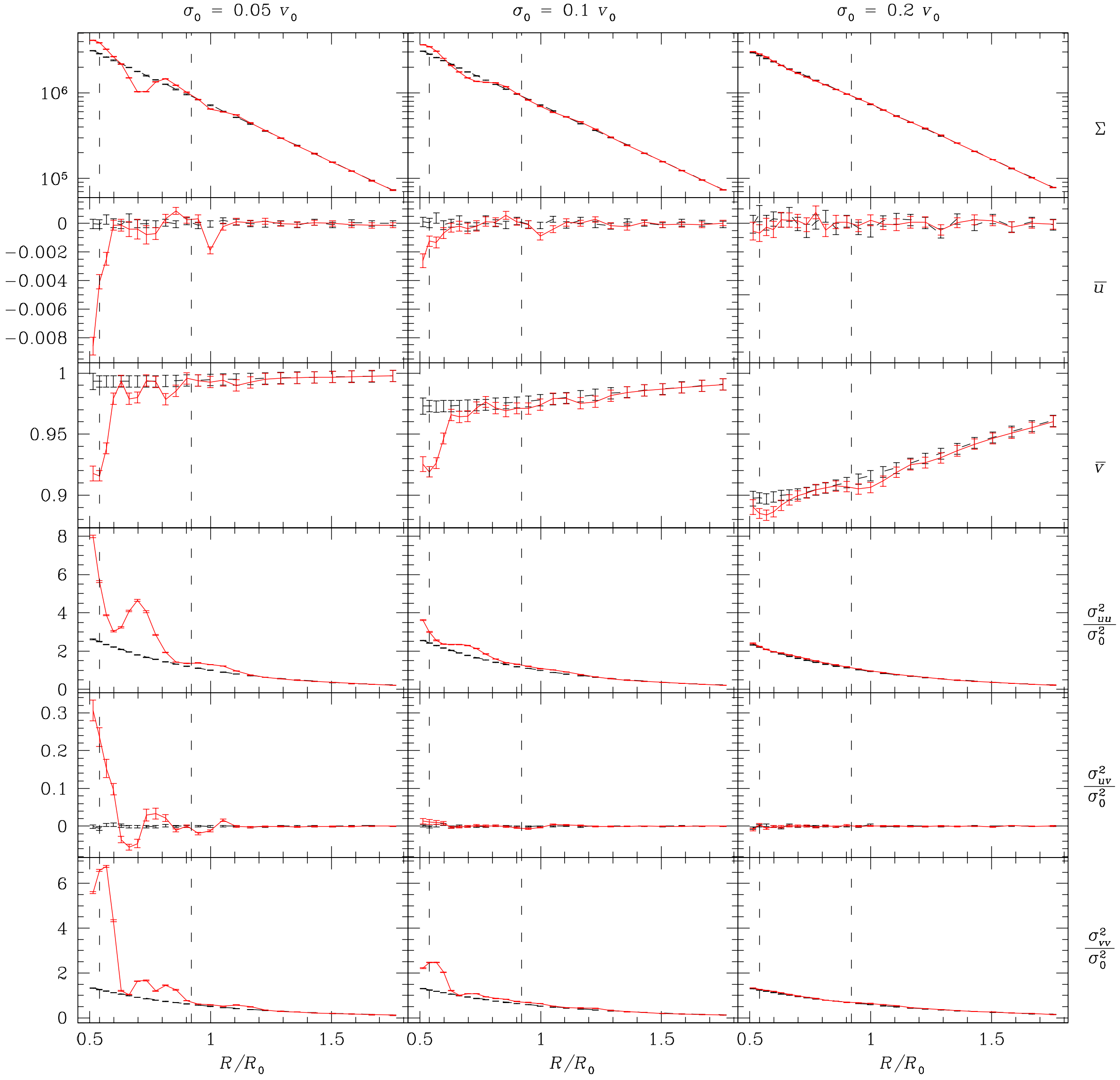

Figure 5.6: Same as Fig. 5.2 but without bar.

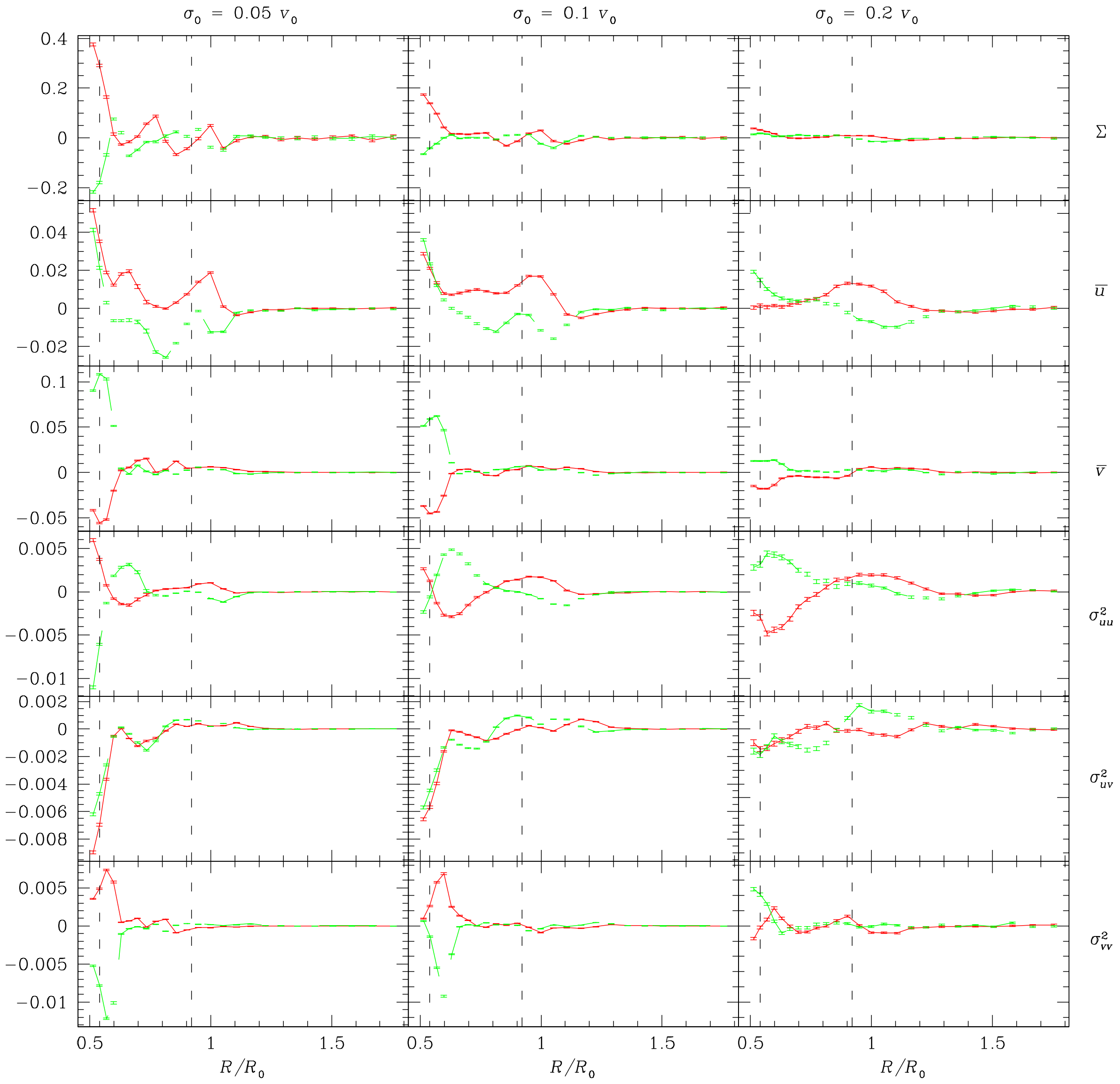

Figure 5.7: Same as Fig. 5.3 but without bar.

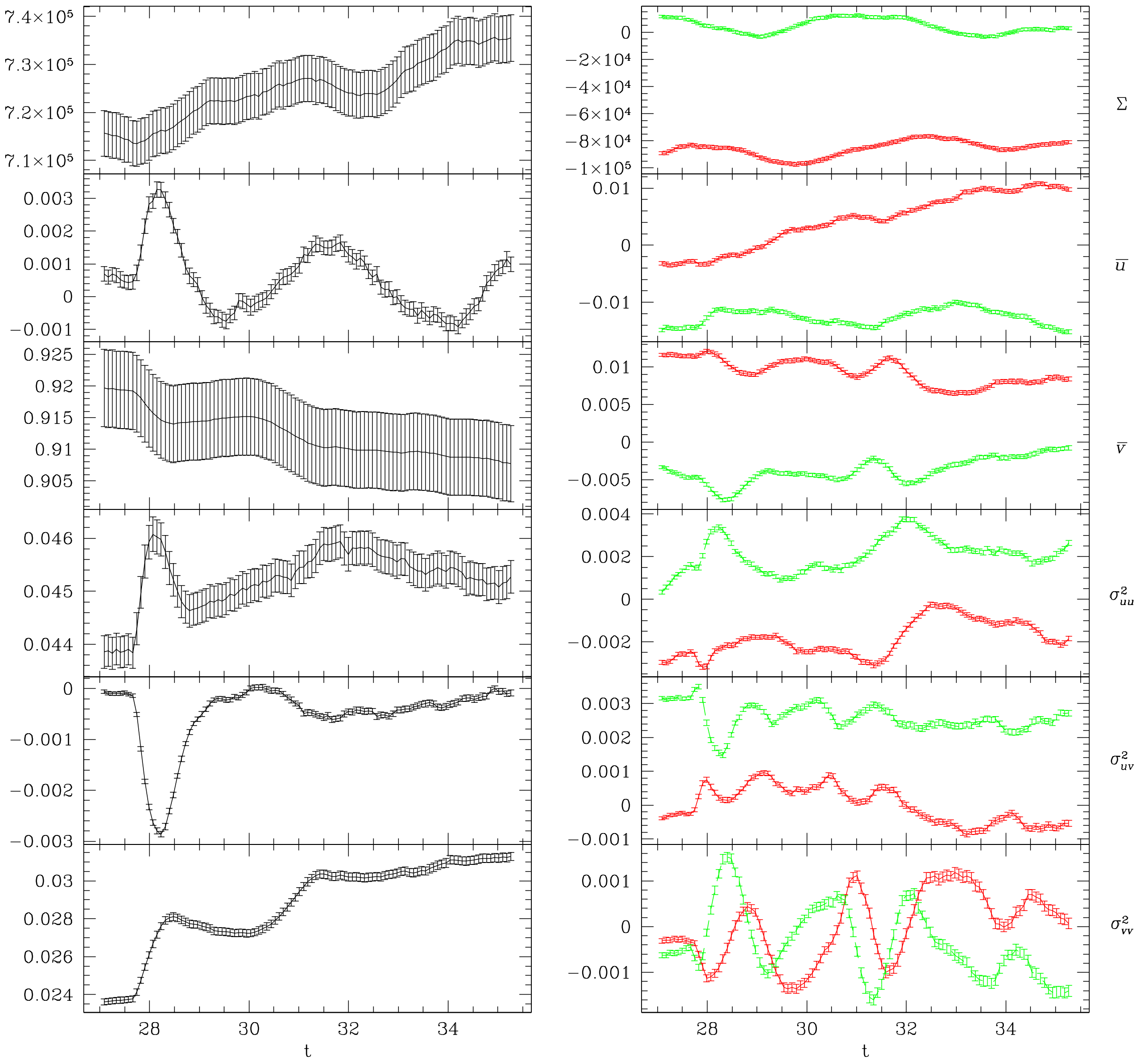

Figure 5.8: Fourier components of the time developing velocity distribution moments near the solar circle. Left panels show $m = 0$, right panels $m = 2$ components. Perturbative potentials are bar and a two-armed spiral pattern with pitch angle 6° and spiral strength $\delta_{\rm spir} = 0.1$. Reference system is co-rotating with the bar.

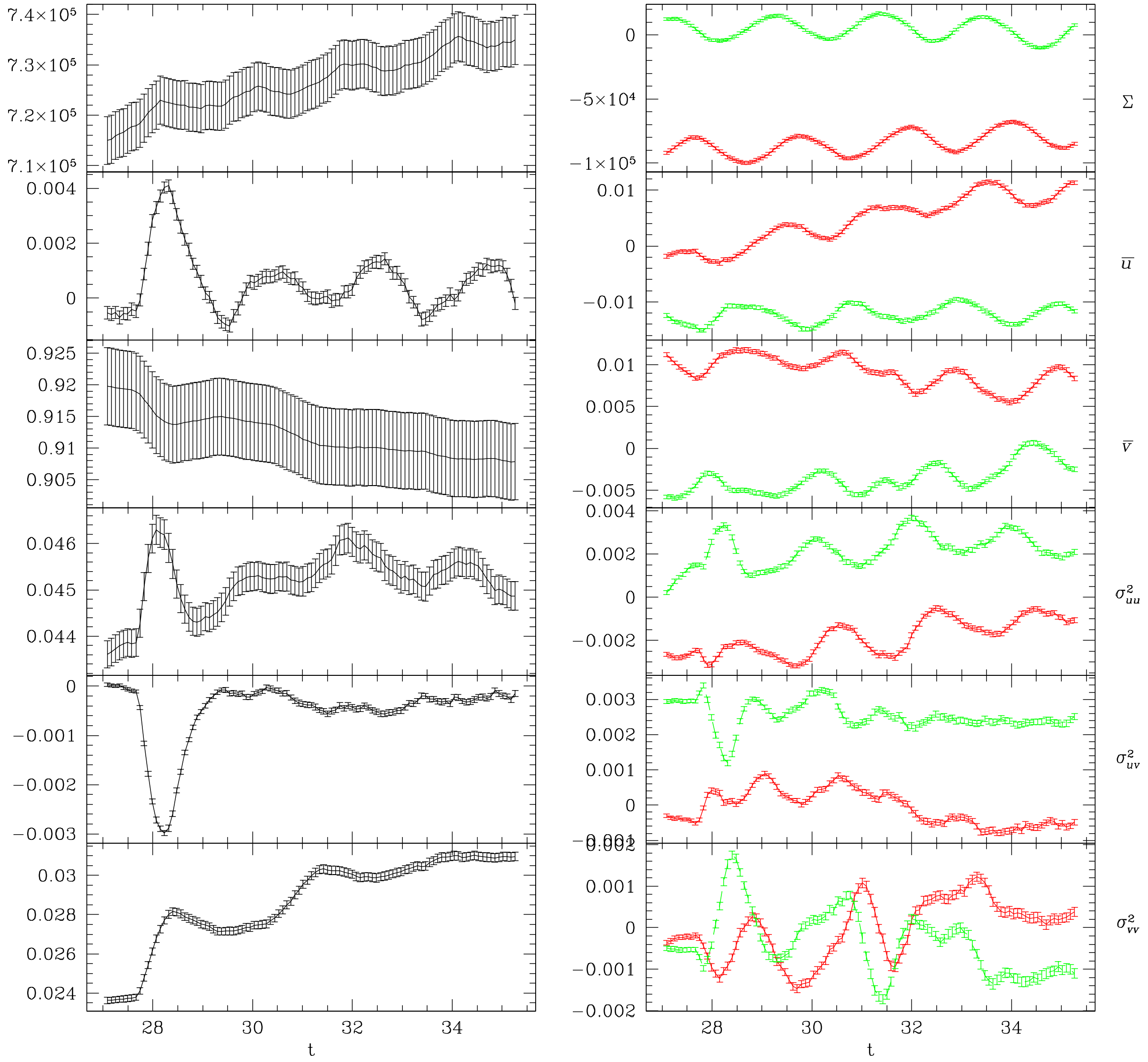

Figure 5.9: Same as Fig. 5.8, but for four-armed spiral, pitch angle of 12°.

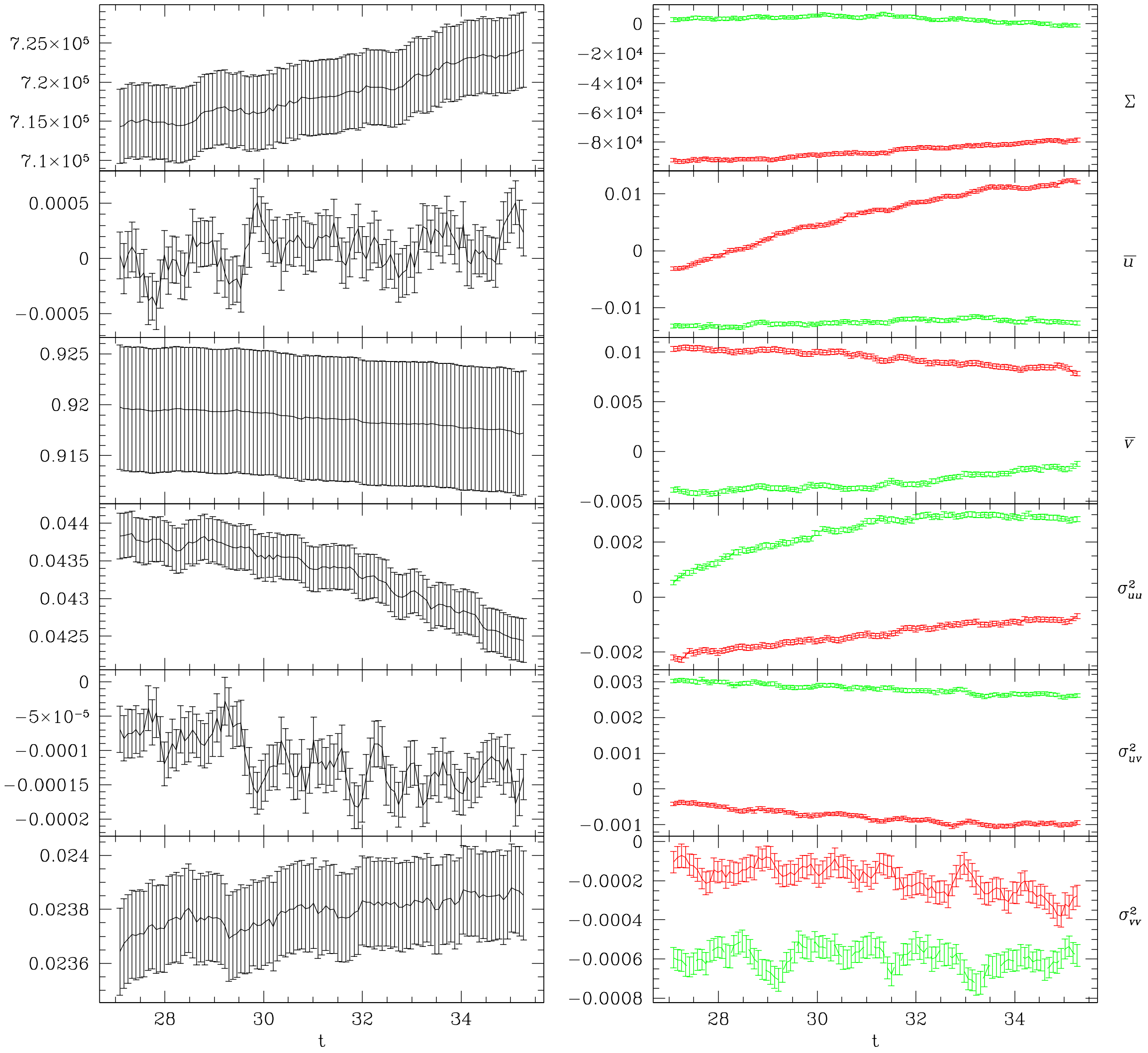

Figure 5.10: Same as Fig. 5.8, but without spiral.

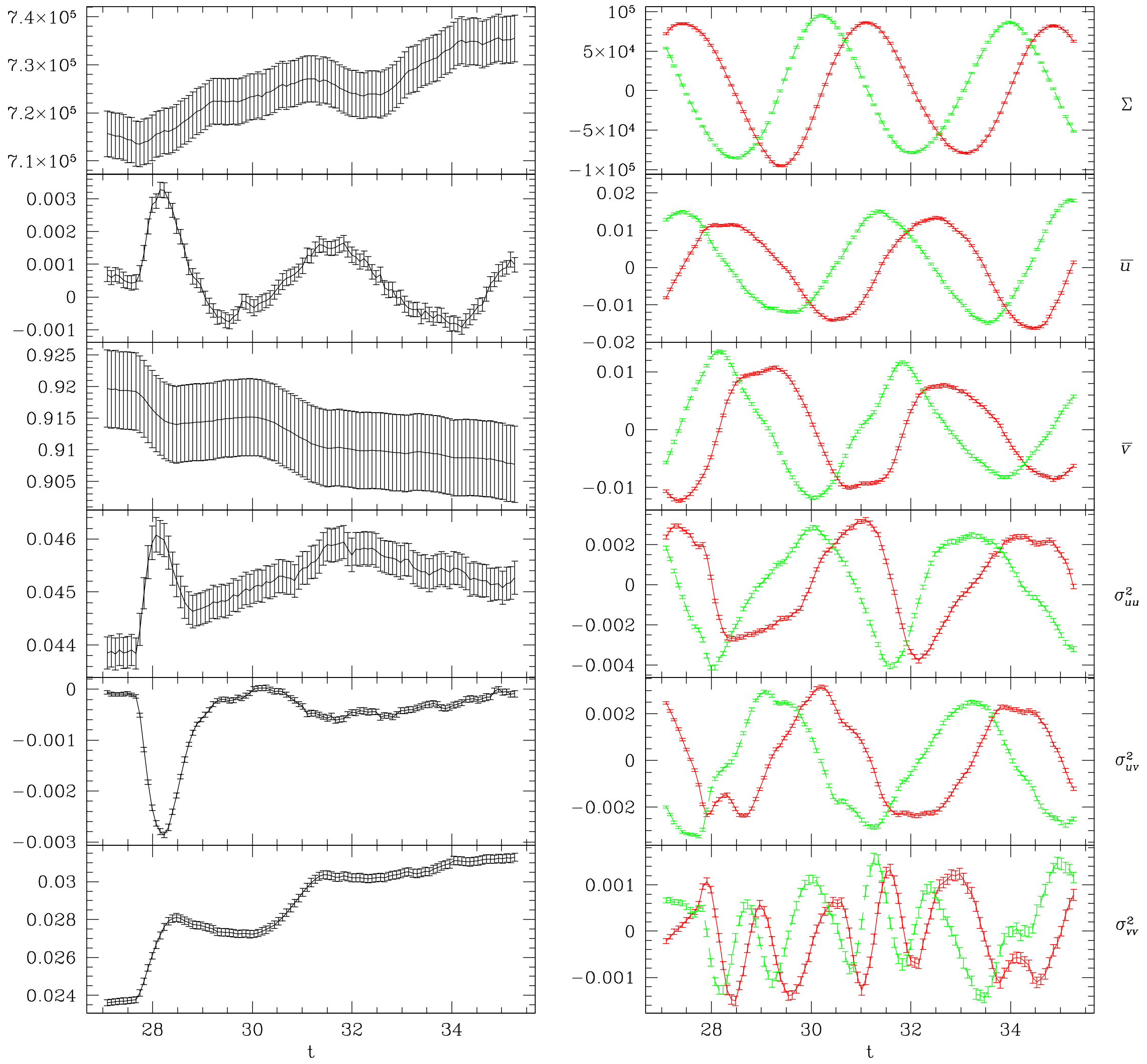

Figure 5.11: Same as Fig. 5.8, but in LSR-system.

for potential construction of $2\delta_{\text{spir}} = 0.02$, this matches more or less. However, self-consistency is not a thing we can expect from this kind of modelling.

Regarding the $m = 0$ components, it is not clear why we should see any oscillations at all (left panels in Figs. 5.8, 5.9, 5.11). However, there seem to be some in Σ and u. They might result from the interplay of the bar and spiral pattern, or perhaps they are merely transient phenomena as well.

5.3.3 Time evolution in the LSR frame

We repeated the analysis of section 5.3.2 in a system rotating with the LSR, in order to have a picture of the evolution of the solar neighbourhood over time (Fig. 5.11). Again we see oscillations, but this time the number of peaks is something more than 2. In this case the peaks are caused by the rotating bar, and they are a reflection of our former findings of the bar-induced perturbations. Because of the symmetry of the bar, we expect 2 peaks per bar period; the time considered is still one period of the relative rotation of bar and spiral, which amounts to approximately 1.11 bar periods. Hence we expect 2.22 peaks. The spiral pattern does not cause any peaks on the time-scale of Fig. 5.11, since we have chosen spiral CR to lie very near to the solar circle. It might, however, contribute to the drift seen in this figures.

Remarkably, the $m = 2$ component of σ^2_{vv} seems to oscillate at double frequency (see Fig. 5.11). First indications of this frequency doubling might already be seen in σ^2_{uu} and σ^2_{uv}. The phenomenon is related to the presence of spiral arms since it does not occur in a bar-only model. We have not found an explanation for this.

5.3.4 Variation of spiral parameters

Considering a two-armed model with a higher pitch angle (Figs. 5.12 – 5.14), we find the resulting density contrast to be largely enhanced. Obviously, it is easier for the particles in the more open spiral structure to accumulate in the potential minimum. Similarly, the amount of excitation of bar-symmetry forbidden modes, which we believe is due to spiral structure, seems to be larger for the higher pitch angle (compare Figs. 5.3 and 5.13).

Of course, the spiral induced perturbations also grow stronger with increasing strength of the spiral structure, however on a much smaller scale.

As we noted above, the number of spiral arms itself does not seem to have a great effect. Obviously, only local gradients are important for the kind of kinematic effects we are interested in, and these do not depend on the large-scale spiral pattern.

5.3.5 Vertex deviation and axis ratio

Reconstructing observables like the vertex deviation and the dispersion axis ratio, we get a picture very similar to the bar-only case, see Fig. 5.15. One difference is that the vertex deviation no longer vanishes for $\varphi = 0°$ and $\varphi = 90°$, which it had to in the bar-only case for symmetry reasons. However even in these cases, it is only in the outlying parts of the disk ($R \gtrsim 1.3R_0$) that the vertex deviation gets substantially different from zero, and we can guess that this holds for all the spiral effects on vertex deviation. The same is probably true for the axis ratio, which hardly shows any difference from the bar-only results except in the outermost parts of the disk.

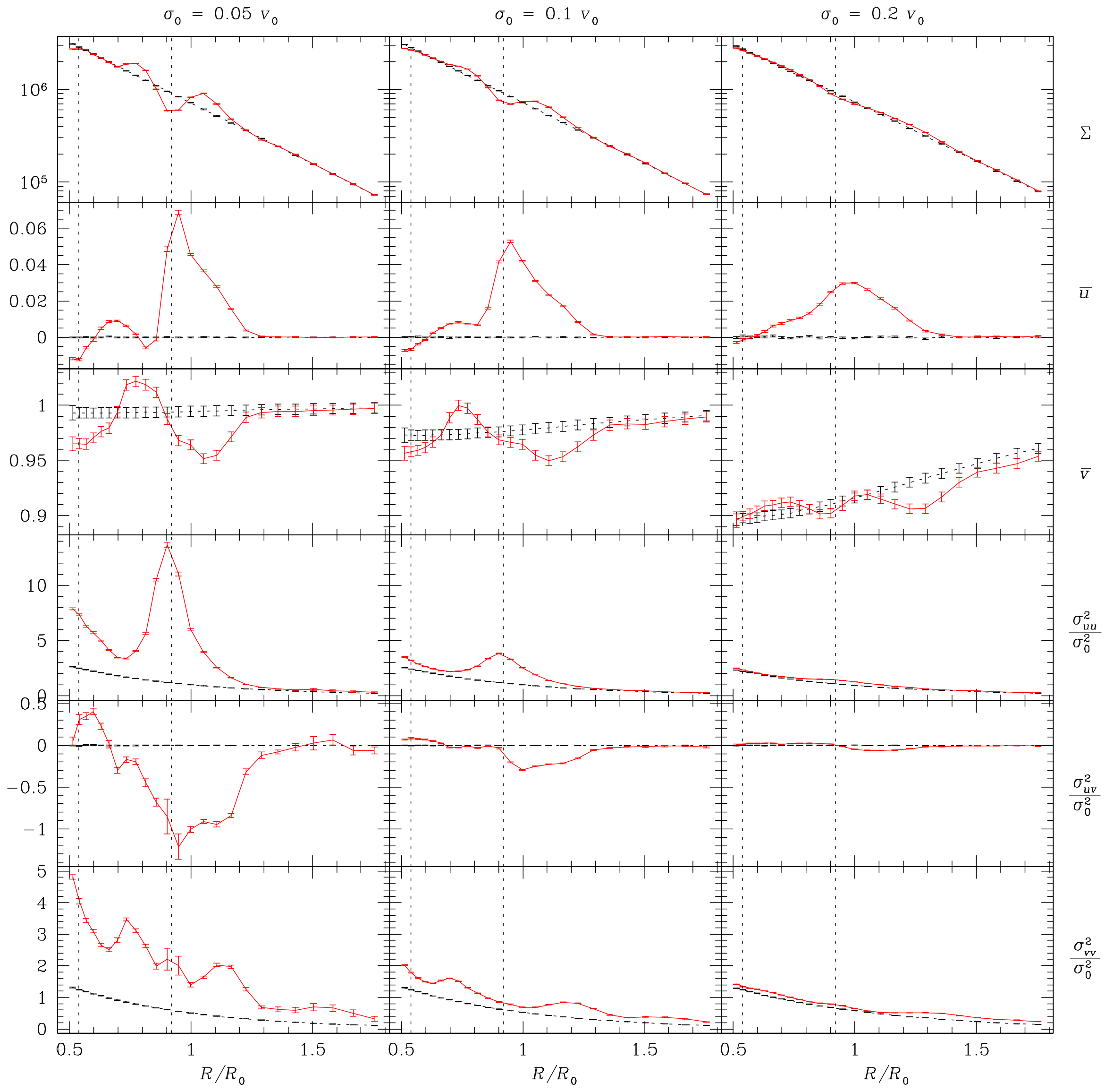

Figure 5.12: Same as Fig. 5.2, but for two-armed spiral with pitch angle of 16°. Spiral strength is still $\delta_{\text{spir}} = 0.1$.

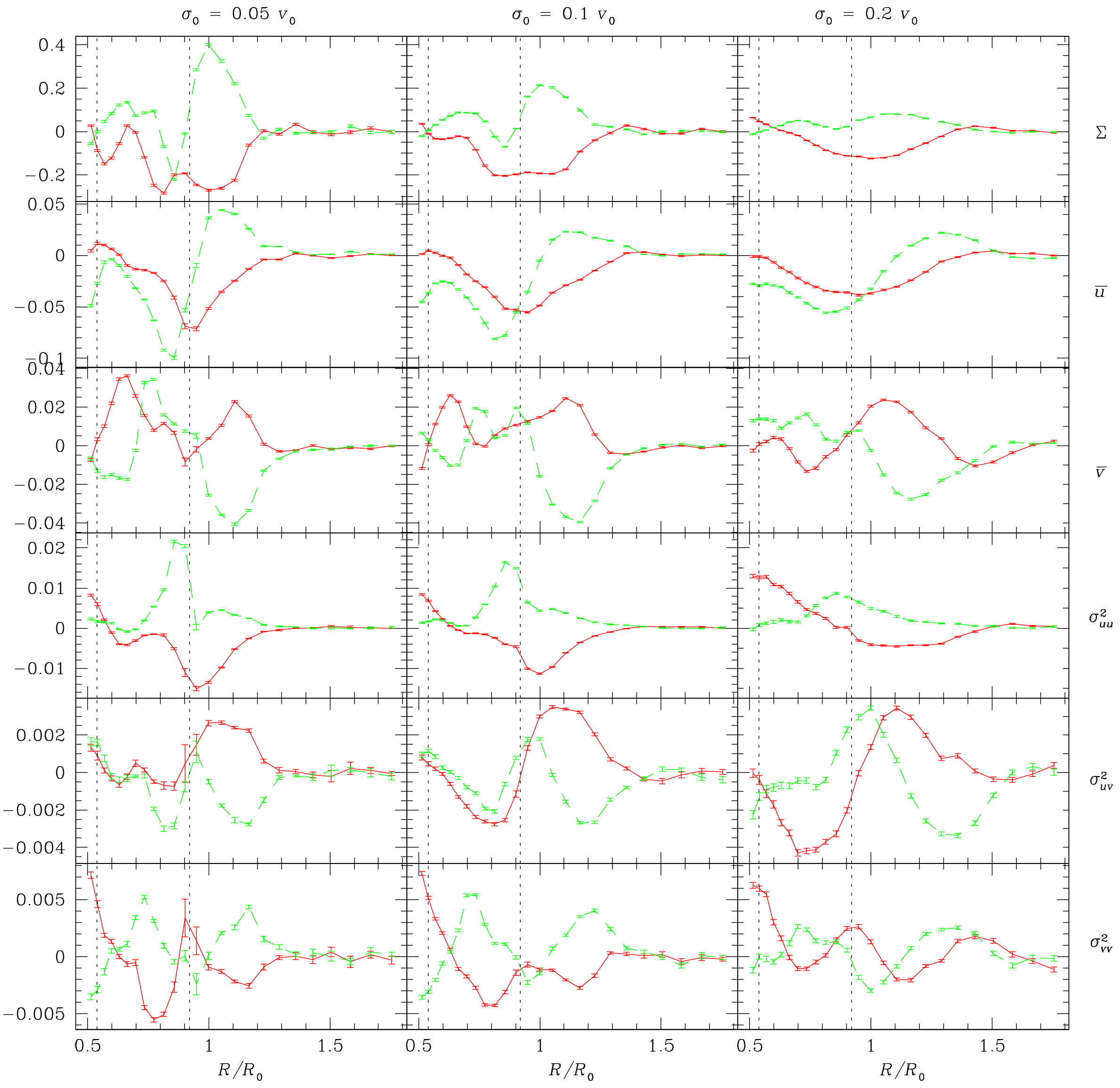

Figure 5.13: Same as Fig. 5.3, but for two-armed spiral with pitch angle of 16°. Spiral strength is still $\delta_{\rm spir} = 0.1$.

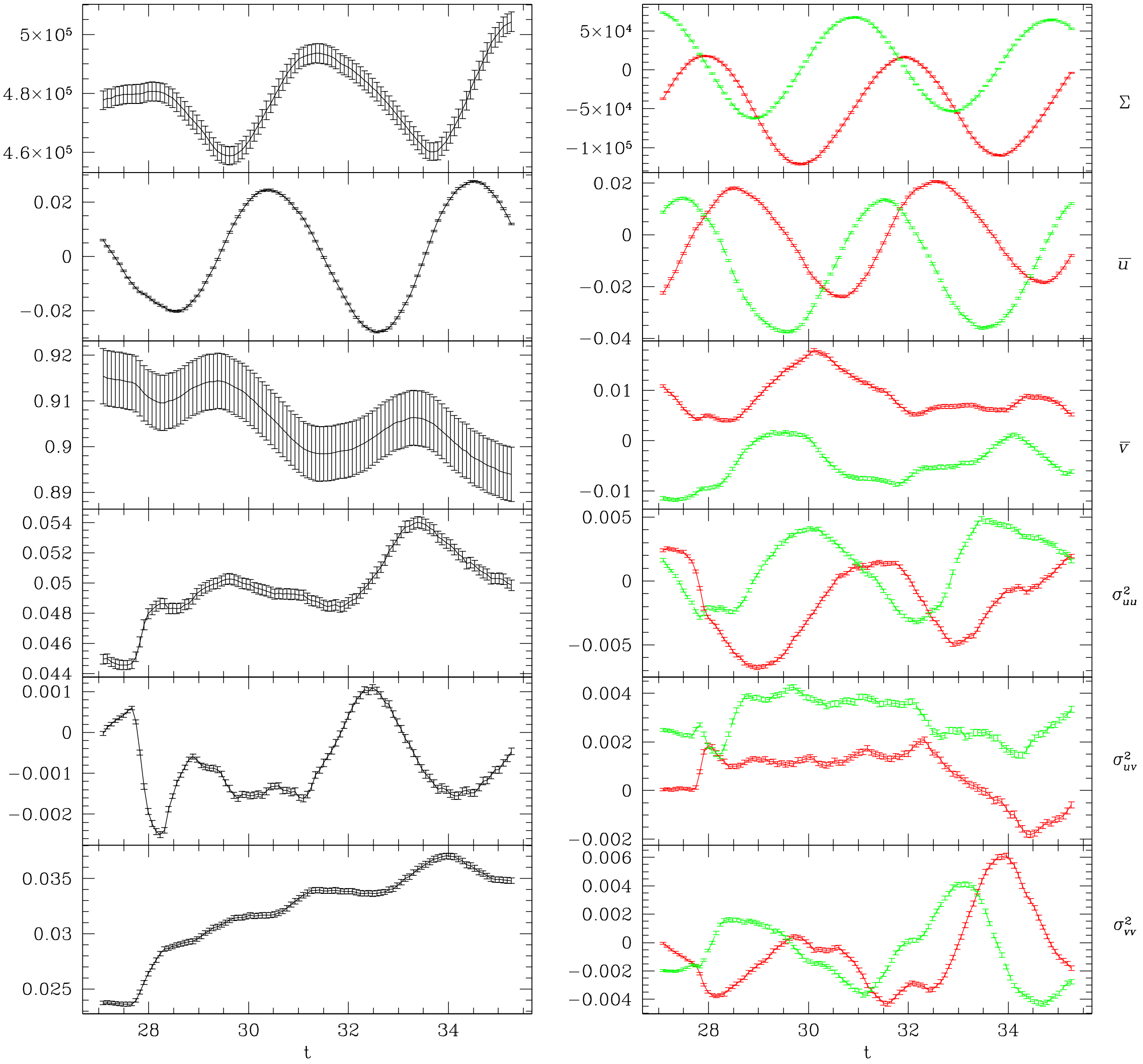

Figure 5.14: Same as Fig. 5.8, but for two-armed spiral with pitch angle of 16°. Spiral strength is still $\delta_{\rm spir} = 0.1$.

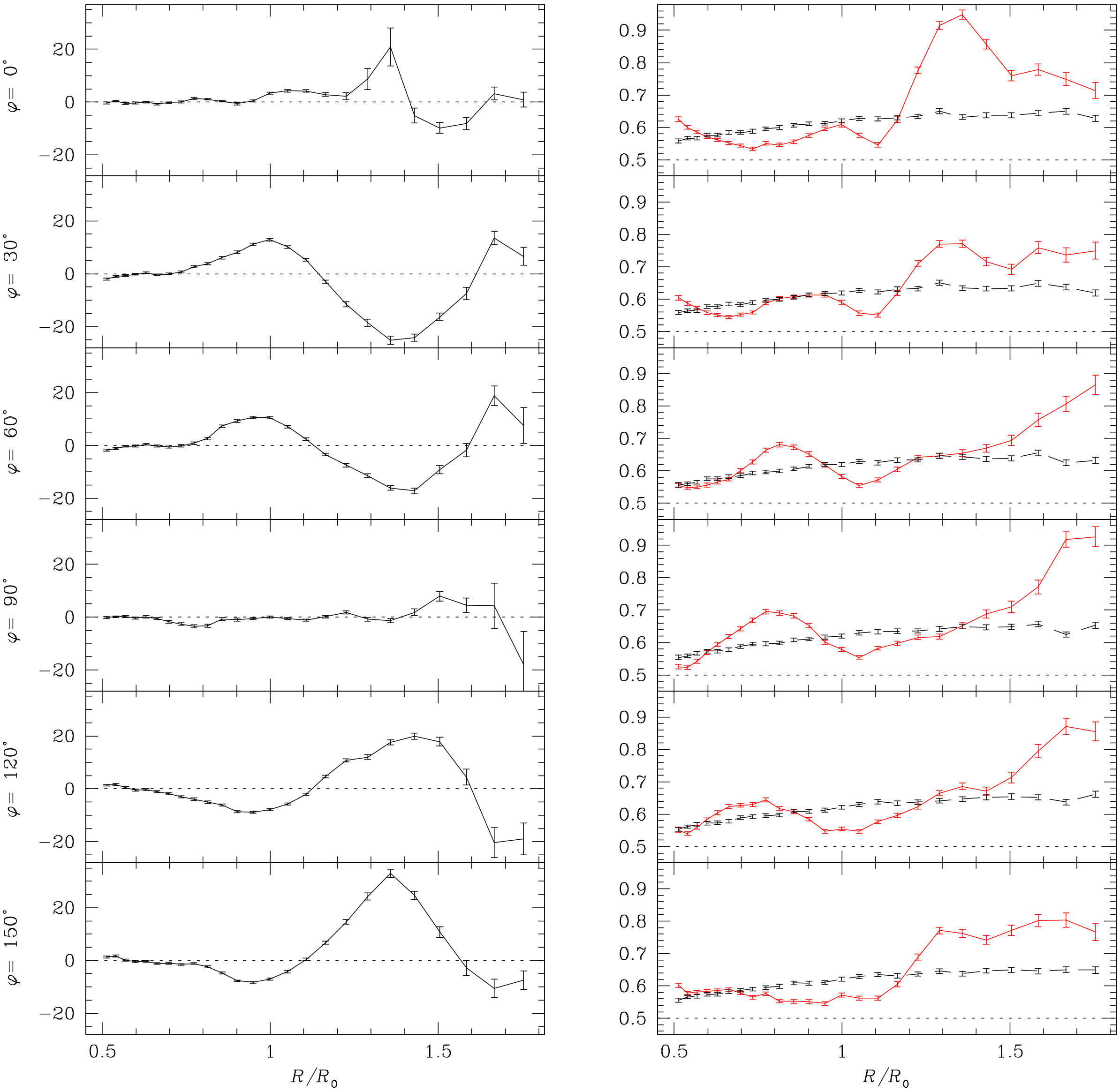

Figure 5.15: Vertex deviation (*left panels*) and dispersion axis ratio (*right panels*) for the spiral model of Figs. 5.2 and 5.3. Compare this to right panels of Figs. 3.7, 3.8, where also symbols are explained.

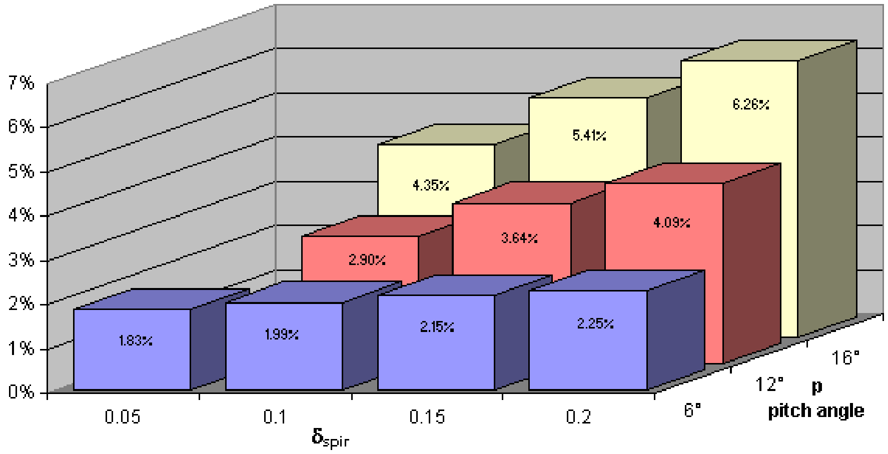

Figure 5.16: Relative importance of spiral and bar perturbations for various spiral stregths δ_{spir} and spiral pitch angles p. The values shown are some composite measure of the difference of various (two-armed) spiral models to the bar-only model, related to some unperturbed measures.

5.4 Discussion

With the spiral structure models, the most important question for us is under what circumstances the spiral-induced perturbations outweigh the ones caused by the bar. As we have seen, in some cases spiral effects seem to be rather small. However, they are growing with increasing spiral strength, and, in particular, they show a strong dependence on pitch angle. It seems that what is decisive for the kinematic impact of the spiral structure is the longer time-span in which particular stars, except at spiral co-rotation radius, feel an equal-sign gradient in the more open spiral structure of higher pitch angles.

We tried to be a bit more quantitative on that. For this purpose, we calculated the difference of various spiral models to our old bar-only model in the zeroth and second Fourier components of our usual quantities (i.e. Σ, $\bar{u}$, $\bar{v}$ and the σ's). It should be sufficient to record (within some interval in radius centered on the presumed position of the Sun) the range of the difference in every case, judged by eye. To get out some meaningful number, we relate these perturbation differences to appropriate unperturbed values of the respective quantities. For this, we take, in particular, $\Sigma(R_0)$ for all surface densities, v_0 for all velocities and v_0^2 for all dispersion components (which, since v_0 is our unit of velocities, amounts to doing nothing and taking the numbers as they are). Finally, in order to have only one number per model, we take a simple average over all these quantities. The result is shown in Fig. 5.16. As can be seen, the dependence on the pitch angle is dramatic while the increase with spiral strength is only modest. Roughly, the bar effects are still dominant, for example, in the spiral model with $p = 6°$, $\delta_{\mathrm{spir}} = 0.1$, where we get a value of 1.99 %. The spiral contributions start to get significant at about two or three times this value, i.e. at $3 - 5$ %. This is in accordance with our finding in section 3 that the bar-only effects are generally of this magnitude. For $\delta_{\mathrm{spir}} = 0.2$ and a pitch angle of $12°$, the bar and spiral perturbations are of similar magnitude, for example.

All this relates to our standard bar strength of $\alpha = 0.01$, which of course can vary as well.

Chapter 6

Conclusion and Outlook

In this thesis, we tried to estimate the amount to which the outer stellar disk of a galaxy is affected by a non-axisymmetric bar-like $m = 2$ perturbation. For this purpose, we did two-dimensional simulations of a sampled galactic distribution function in suitable model potentials with an adiabatically growing bar perturbation (and later additional spiral perturbations as well) and analysed the resulting velocity distribution.

The main conclusion of this work is that non-axisymmetries of the Galaxy, or a bar in particular, might be the true reason of otherwise unexplained findings. As such, we have the fact that the velocity dispersion axis ratio seems to be smaller than $1/2$ by measurement, whereas axisymmetric theory would indicate values larger than $1/2$. For a flat rotation curve, axisymmetric theory would also predict that the axis ratio should approach $1/2$ in the limit of small velocity dispersions. Our simulations show that the non-axisymmetric influence of a central bar may cause values of the axis ratio below $1/2$, and these deviations will not vanish with decreasing dispersion.

Another feature which might be due to the bar or spiral structure is the vertex deviation of the local velocity dispersion. The existence of a non-vanishing vertex deviation seems fairly established observationally, although its amount is seen to depend on the stellar population. While for the younger stars it may partly be due to non-equilibrium effects, we argued in section 3.3 that it is predominantly caused by non-axisymmetric influences as in our model. At any rate we are well able to reproduce the observed range of values for the vertex deviation.

As another feature amenable to observational verification, we mentioned a possible radial motion of the LSR (see section 3.3), which should not be to be too difficult to measure. But, as we have seen, the observational situation is not yet clear. In our model, radial motions occur frequently, but it seems that the Sun happens to lie near a zero point of the mean radial velocity. Negative results in observational searches for radial LSR motions (Gould 2003 [51]) would be in accordance with this.

In section 4, we elaborated on the difference between the velocity dispersion axis ratio and the expression $-b/(a-b)$ of the Oort constants. The so-called Oort relation claims that both are equal, at least for small velocity dispersions. We showed that, although in the axisymmetric case their difference does indeed get smaller with smaller dispersions, they are completely different things if any non-axisymmetries are involved.

We also constructed the Oort constants in our model. Since these are observationally not very well known, it is not easy to draw any conclusions from this. We did however find the possibility of a non-vanishing and negative c and k near the solar circle as an effect of the bar perturbation, which might also have been detected observationally in the solar neighbourhood by Olling & Dehnen 2003 [71].

In another set of simulations, we included spiral structure into the model. Here our prime objective was to find out whether our bar effects might be superseded by the perturbations caused by the spiral arms. We find that whether this is the case or not depends very much on the details of the spiral structure, which unfortunately are very poorly known. We find in particular, that the spiral pitch angle is of the utmost importance here, much more than the proper strength of the spiral structure as measured by the density contrast. With our standard value for the bar strength, which we think is realistic, the range of values considered in the literature for the spiral parameters yields spiral perturbations predominating over the bar's as well as the other way round.

Observational prospects

With regard to direct observations of velocity distributions, the most relevant data up to now are the results of the HIPPARCOS mission, i.e. the HIPPARCOS and TYCHO catalogues. As we mentioned, HIPPARCOS did not measure line-of-sight velocities, so reconstructing the velocity distribution is not straightforward, but involved some maximum-likelihood fitting (Dehnen 1998 [25]). There is now a ground-based project called RAVE ("RAdial Velocity Experiment") which will provide the missing line-of-sight velocities within the next decade (see the RAVE White Paper [91]).

While the future of a number of intermediate astrometric satellite missions (DIVA, FAME) is uncertain due to funding difficulties, there will certainly come a golden age of Galactic astrometry with the availability of the GAIA data. GAIA is a planned astrometric satellite which will measure positions and velocities of a very large number of stars with unprecedented accuracy (see the concept and technology study report by Perryman et al. 2001 [75]). Launch is planned for 2012, data will become available around 2015 to 2020. GAIA will be able to measure parallaxes with microarcsecond-accuracy. From repeated measurements over the expected lifetime of five years, proper motions of the stars will be determined with an accuracy in the range of a few to some ten μas/yr, depending on spectral type and apparent luminosity. In addition, GAIA will also measure line-of-sight velocities. Together with the distance, the primary product of parallax measurements, this gives a three-dimensional view of a large part of the Galaxy, and reconstructions of the actual velocity distribution appear possible not only locally, but also for nearby locations in the Galaxy. This should allow the identification of non-axisymmetric influences on the outer disk. Non-local measurements are essential for really matching our results to observations, and only GAIA will be able to provide these.

Variations in the tangential direction would seem most promising with respect to an experimental verification, since in the radial direction any bar induced effects are superseded by much stronger natural gradients. However, our effects are not really large. Our prediction based on the long-term bar-only model with standard bar strength would be a gradient along the tangential direction of about 0.3 %/kpc in surface density, and 0.9 km/s/kpc or 0.2 km/s/kpc for $\bar{u}$ and $\bar{v}$, respectively. Whether gradients like that will be detectable with GAIA remains to be seen, it will at any rate be close to the limit.

For the time being it is unclear what accuracies can be reached with GAIA for our purposes. In order to match the heliocentric observational data to a Galactic model, we must at some point convert the velocity data from a heliocentric to a galactocentric system. That means we have to perform some equivalent of transformation (H.14) in appendix H. Now these transformations inevitably involve the poorly known parameters v_0 and R_0, and the a priori high accuracy of the GAIA data will get lost. Recently, the uncertainties on these parameters are at least $\Delta R_0 \approx \pm 1$ kpc and $\Delta v_0 \approx \pm 30$ km/s, i.e. roughly 12% and 14%, respectively (cf. Dehnen 2002 [29]). Clearly, by the time of GAIA, these uncertainties will have diminished, with the help of the GAIA data themselves or from other sources. However, comparing the GAIA data to our predictions will probably require overall modelling and parameter fitting, and the accuracies which might be obtained in this process can hardly be foreseen today.

Judging from the accuracy of the GAIA data alone, we have a limit on the magnitude of the stars we can use for our analysis. In particular, the line-of-sight velocities determined by GAIA get very inaccurate for stars fainter than perhaps 12th or 14th magnitude (see Perryman et al. 2001 [75]). Since our effects are of a secular nature, the stellar population used for their detection must have a certain minimum age, and since bright stars have short lifespans, this puts a limit on the distance d from the Sun up to which such a program can be carried through. Assuming that we can use F stars with an intrinsic luminosity of $M \approx 2.5$, we can, however, certainly go out to distances of about 5 kpc from the Sun without getting an uncertainty in line-of-sight velocity greater than 5 km/s. Of course, this would still be too high in view of the above-mentioned gradients.

However, even before GAIA, there will certainly be major progress in our knowledge of Galactic structure. In particular, large-scale infrared surveys like the just completed 2MASS will have profound impact. The shape and extent of the bar will be clarified further, and also the fundamental Galactic constants R_0 and v_0 will be determined more accurately. A very interesting approach for the later is to measure the proper motion of Sgr A*, which gives a quite sharp but unfortunately degenerate constraint for these two parameters (see Reid et al. 2003 [83]). Our analysis of the combined influence of bar and spiral perturbations was especially handicapped by the very poor knowledge of almost all parameters pertaining to the spiral structure of the Galaxy. We expect that the infrared surveys will improve the situation here and allow a detailed picture of the spiral structure of the Milky Way to be constructed (see e.g. Quillen 2002 [80] as a first step). With increasing knowledge, our model could be revisited from time to time.

Appendix A

Lagrangian and Hamiltonian Mechanics in a Rotating Frame

Consider the motion of a particle of unity mass in a rotating potential. Obviously, we have two different sets of coordinates: coordinates $\mathbf{r}_I$ of an inertial frame on the one hand, coordinates $\mathbf{r}$ of the co-rotating frame on the other. Both are related by

$$\begin{pmatrix} x \\ y \\ z \end{pmatrix} = \begin{pmatrix} \cos\Omega t & -\sin\Omega t & 0 \\ \sin\Omega t & \cos\Omega t & 0 \\ 0 & 0 & 1 \end{pmatrix} \begin{pmatrix} x_I \\ y_I \\ z_I \end{pmatrix} \tag{A.1}$$

Instead of Cartesian coordinates we will use cylindrical coordinates (R, φ, z). We then have $R = R_I$ and $z = z_I$ and we will not distinguish between these. In case of a constant rotation speed, we would have $\varphi = \varphi_I - \Omega t$ for the relationship between inertial and co-rotating angle, but we will allow for time dependent rotation $\Omega = \Omega(t)$, so we only have $\dot\varphi = \dot\varphi_I - \Omega(t)$.

Inertial coordinates:

Lagrangian:

$$\mathcal{L}_I = \frac{1}{2}\left(\dot R^2 + R^2\dot\varphi_I^2 + \dot z^2\right) - \Phi(R, \varphi_I, z, t) \tag{A.2}$$

The canonically conjugate momenta are

$$p_R = \frac{\partial\mathcal{L}}{\partial\dot R} = \dot R \tag{A.3}$$

$$p_{\varphi_I} = \frac{\partial\mathcal{L}}{\partial\dot\varphi_I} = R^2\dot\varphi_I \tag{A.4}$$

$$p_z = \frac{\partial\mathcal{L}}{\partial\dot z} = \dot z \tag{A.5}$$

and the Euler-Lagrange equations of motion read:

$$0 = \ddot R - R\dot\varphi_I^2 + \frac{\partial\Phi}{\partial R} \tag{A.6}$$

$$0 = R^2\ddot\varphi_I + 2R\dot R\dot\varphi_I + \frac{\partial\Phi}{\partial\varphi_I} \tag{A.7}$$

$$0 = \ddot z + \frac{\partial\Phi}{\partial z} \tag{A.8}$$

By the usual procedure of a Legendre transformation we arrive at the Hamiltonian:

$$H_I = \frac{1}{2}\left(p_R^2 + \frac{1}{R^2}p_{\varphi I}^2 + p_z^2\right) + \Phi(R, \varphi_I, z, t) \tag{A.9}$$

The Hamiltonian equations of motion read

$$\begin{aligned}
\dot{R} &= p_R && \text{(A.10)}\\
\dot{\varphi}_I &= \frac{1}{R^2}p_{\varphi_I} && \text{(A.11)}\\
\dot{z} &= p_z && \text{(A.12)}\\
\dot{p}_R &= \frac{1}{R^3}p_{\varphi_I}^2 - \frac{\partial\Phi}{\partial R} && \text{(A.13)}\\
\dot{p}_{\varphi_I} &= -\frac{\partial\Phi}{\partial\varphi_I} && \text{(A.14)}\\
\dot{p}_z &= -\frac{\partial\Phi}{\partial z} && \text{(A.15)}
\end{aligned}$$

They are, of course, equivalent to the Euler-Lagrangian ones.

The Hamiltonian has the physical meaning of the energy of the system, but it is not conserved because of the time-varying potential:

$$\frac{dH_I}{dt} = \frac{\partial H_I}{\partial t} = \frac{\partial\Phi}{\partial t} \tag{A.16}$$

Co-rotating coordinates:

Note that the potential now does not have an explicit time dependence, but is fixed with respect to the coordinates.

Lagrangian:

$$\mathcal{L} = \frac{1}{2}\left(\dot{R}^2 + R^2(\dot{\varphi}+\Omega)^2 + \dot{z}^2\right) - \Phi(R, \varphi, z) \tag{A.17}$$

The canonically conjugate momenta are here

$$\begin{aligned}
p_R &= \frac{\partial\mathcal{L}}{\partial\dot{R}} = \dot{R} && \text{(A.18)}\\
p_\varphi &= \frac{\partial\mathcal{L}}{\partial\dot{\varphi}_I} = R^2(\dot{\varphi}+\Omega) && \text{(A.19)}\\
p_z &= \frac{\partial\mathcal{L}}{\partial\dot{z}} = \dot{z} && \text{(A.20)}
\end{aligned}$$

and the Euler-Lagrange equations:

$$\begin{aligned}
0 &= \ddot{R} - R(\dot{\varphi}+\Omega)^2 + \frac{\partial\Phi}{\partial R} && \text{(A.21)}\\
0 &= R^2(\ddot{\varphi}+\dot{\Omega}) + 2R\dot{R}(\dot{\varphi}+\Omega) + \frac{\partial\Phi}{\partial\varphi} && \text{(A.22)}\\
0 &= \ddot{z} + \frac{\partial\Phi}{\partial z} && \text{(A.23)}
\end{aligned}$$

The Hamiltonian in this case is as follows:

$$H = \frac{1}{2}\left(p_R^2 + \frac{1}{R^2}p_\varphi^2 - 2p_\varphi\Omega + p_z^2\right) + \Phi(R, \varphi, z) \tag{A.24}$$

and the Hamiltonian equations are

$$\dot{R} = p_R \tag{A.25}$$

$$\dot{\varphi} = \frac{1}{R^2} p_\varphi - \Omega(t) \tag{A.26}$$

$$\dot{z} = p_z \tag{A.27}$$

$$\dot{p}_R = \frac{1}{R^3} p_\varphi^2 - \frac{\partial \Phi}{\partial R} \tag{A.28}$$

$$\dot{p}_\varphi = -\frac{\partial \Phi}{\partial \varphi} \tag{A.29}$$

$$\dot{p}_z = -\frac{\partial \Phi}{\partial z} \tag{A.30}$$

Comparing these with eqs. (A.10) - (A.15), we see that the only equation which is formally different is (A.26).

The Hamiltonian in this frame is not the energy, but we see that for a uniform rotation $\Omega = \text{const}$, it is conserved:

$$\frac{dH}{dt} = \frac{\partial H}{\partial t} = -p_\varphi \dot{\Omega}(t) \tag{A.31}$$

We call it the Jacobi integral E_J. When working in the co-rotating frame, it can often be used as a substitute for the energy.

The physical angular momentum L is clearly the quantity p_{φ_I} from (A.4), but we can see that it is also identical to the canonical momentum in the co-rotating frame (A.19). So, writing $E := H_I$ for the energy of the system, we get from comparing (A.9) and (A.24) that

$$E_J := H = E - L\Omega \tag{A.32}$$

From the standpoint of Noether's theorem, it is not surprising that there should be some conserved combination of angular momentum and energy in the case of uniform rotation, where the potential is constant in an appropriately rotating frame.

To express the physical quantities in co-rotating coordinates, use $\dot{\varphi}_I = \dot{\varphi} + \Omega$ in (A.9):

$$E = \frac{1}{2}\left(\dot{R}^2 + R^2\dot{\varphi}^2\right) + \Phi + R^2\Omega\dot{\varphi} + \frac{1}{2}R^2\Omega^2 \tag{A.33}$$

The angular momentum is

$$L = R^2(\dot{\varphi} + \Omega) \tag{A.34}$$

and using this in Jacobi's integral yields

$$E_J = \frac{1}{2}\left(\dot{R}^2 + R^2\dot{\varphi}^2\right) + \Phi - \frac{1}{2}R^2\Omega^2, \tag{A.35}$$

which is formula (2.14).

Appendix B

Numerical Integration Techniques

For doing the orbit integrations, we first employed a standard Runge-Kutta technique. Later we changed to a symplectic integrator for greater speed.

Runge-Kutta integrator

We used an embedded fifth-order Runge-Kutta technique with adaptive stepsize according to Cash & Karp (see Press et al. 2002 [78]). In detail, this means that for a system of first order differential equations $d\mathbf{y}/dt = \mathbf{F}(t, \mathbf{y})$ six evaluations of $\mathbf{F}$ per time step τ are used to construct two different approximations $\mathbf{y}_1$ and $\mathbf{y}_2$ for $\mathbf{y}(t+\tau)$ correct to fifth or fourth order in τ respectively. The difference $\Delta := |\mathbf{y}_1 - \mathbf{y}_2|$ then gives a measure of the error and τ is adjusted after every timestep so that this error is smaller than some prescribed accuracy ϵ. This is achieved by setting

$$\tau' = \tau \left(\frac{\epsilon}{\Delta} \right)^{0.2} \tag{B.1}$$

In particular, we work in cylindrical coordinates in the co-rotating frame in a Hamiltonian framework, and we restricted ourselves to two dimensions. So the system of equations to be solved in this way is eqns. (A.25), (A.26), (A.28) and (A.29).

Symplectic integrator

Fundamentals of symplectic integration techniques

Symplectic integration algorithms are particularly designed for Hamiltonian systems, their distinctive feature is that they preserve the symplectic measure of phase space flows which otherwise manifests itself in Liouville's theorem and the Poincaré invariants. Although this conservation can partly get lost when adaptive timestep sizes are used (Preto & Tremaine 1999 [79]), this algorithms usually have other advantages. In particular, they can be arranged to be completely time-reversible.

The idea of symplectic integration is to split the Hamiltonian into two (or more) parts, $H = H_A + H_B$ say, and to use analytical solutions of either part to construct a solution to the entire Hamiltonian correct to higher order of the timestep τ.

The equation of motion for any dynamical variable ξ written with the help of the Poisson bracket $[.,.]$

$$\frac{d\xi}{dt} = [\xi, H] \tag{B.2}$$

has the formal solution

$$\xi(t+\tau) = e^{\tau P_H}\xi(t), \tag{B.3}$$

where the operator P_H means taking the Poisson bracket with H:

$$P_H = [\,.\,, H] \tag{B.4}$$

The operator

$$\begin{aligned} S(\tau) &:= e^{\tau P_H} \\ &= 1 + \tau P_H + \frac{1}{2}\tau^2 P_H^2 + \ldots \end{aligned} \tag{B.5}$$

can be called the time evolution operator. Defining $A := P_{H_A}, B := P_{H_B}$, this gives for our split Hamiltonian

$$\begin{aligned} S(\tau) &= e^{\tau(A+B)} \\ &= 1 + \tau(A+B) + \frac{1}{2}\tau^2(A^2 + AB + BA + B^2) + \ldots, \end{aligned} \tag{B.6}$$

whereas some variant of Baker-Campbell-Hausdorff formula yields

$$\begin{aligned} S_A(\tau)S_B(\tau) &= e^{\tau A}e^{\tau B} \\ &= 1 + \tau(A+B) + \frac{1}{2}\tau^2(A^2 + 2AB + B^2) + \ldots \end{aligned} \tag{B.7}$$

As can be seen, the difference is only second order in τ. By splitting into more than two parts, the error can be shifted to yet higher orders.

Typically, one would split the Hamiltonian into its kinetic and potential parts. For the latter, knowing the analytical solution is trivial since this part usually does not involve the canonical momenta. The motion due to the momentum-dependent part is called a "drift", the one due to the potential part a "kick". Finding an analytical solution to the drift part is crucial to the problem and determines if the method is applicable.

Now the calculation for a timestep is constructed out of kick and drift solutions. Algorithms of such kind are called "leapfrogs", because of the alternating use of kicks and drifts. Two varieties are in use: "KDK" and "DKD", see Table B.1.

KDK:

possible I/O	
kick by $\tau/2$	calculation step
drift by τ	
kick by $\tau/2$	
adapt τ	
possible I/O	

DKD:

possible I/O	
drift by $\tau/2$	calculation step
kick by $\tau/2$	
adapt τ	
kick by $\tau/2$	
drift by $\tau/2$	
possible I/O	

Table B.1: KDK- and DKD-variants of the leapfrog integration. In DKD, the last drift step may be contracted together with the first drift of the following calculation step, if no I/O occurs in between.

Adapting the size of the timestep requires some care. A safe way to retain the time-reversibility of the calculation is to obey the following form

$$s(\tau,\tau') = T(\mathbf{x},\mathbf{p},\Phi,\nabla\Phi) \tag{B.8}$$

with some suitable function T and a symmetrical function s of τ and the new timestep τ'. A possible choice is the geometric mean $s(\tau,\tau') = \sqrt{\tau\tau'}$.

Application to our problem

Since we work in the co-rotating system the relevant Hamiltonian is (A.24). We will use Cartesian coordinates here, though, so the drift equations are as follows:

$$\begin{aligned} \dot{p}_x &= p_y\Omega && \text{(B.9)}\\ \dot{p}_y &= -p_x\Omega && \text{(B.10)}\\ \dot{x} &= p_x + y\Omega && \text{(B.11)}\\ \dot{y} &= p_y - x\Omega && \text{(B.12)} \end{aligned}$$

Their solution for development in a time τ is

$$\begin{aligned} p'_x &= p_x\cos\Omega\tau + p_y\sin\Omega\tau && \text{(B.13)}\\ p'_y &= -p_x\sin\Omega\tau + p_y\cos\Omega\tau && \text{(B.14)}\\ x' &= (x+p_x\tau)\cos\Omega\tau + (y+p_y\tau)\sin\Omega\tau = \\ &= x\cos\Omega\tau + y\sin\Omega\tau + p'_x\tau && \text{(B.15)}\\ y' &= -(x+p_x\tau)\sin\Omega\tau + (y+p_y\tau)\cos\Omega\tau = \\ &= -x\sin\Omega\tau + y\cos\Omega\tau + p'_y\tau && \text{(B.16)} \end{aligned}$$

The kick equations

$$\dot{p}_x = -\frac{\partial\Phi}{\partial x}, \qquad \dot{p}_y = -\frac{\partial\Phi}{\partial y}, \tag{B.17}$$

$$\dot{x} = \dot{y} = 0 \tag{B.18}$$

have the obvious solution

$$p'_x = p_x - \frac{\partial\Phi}{\partial x}\tau, \qquad p'_y = p_y - \frac{\partial\Phi}{\partial y}\tau, \tag{B.19}$$

$$x' = x, \qquad y' = y \tag{B.20}$$

For adaptation of the timestep we take

$$T(R) = f\left(\frac{R}{R_0}\right)^{2-\frac{2}{\gamma}}, \tag{B.21}$$

where γ is the usual epicycle axis ratio (2.11) and f is a factor adjusted once for every sample point in such a way as to have a constant number N of timesteps per circulation:

$$f = \frac{2\pi}{Nv_c}R^{\frac{2}{\gamma}-1} \tag{B.22}$$

However, we restrict ourselves to change the step size by factors of 2 according to

$$\tau' = \begin{cases} 2\tau & \text{for } T > 2^{1/4}\tau \\ \tau/2 & T < \tau/2^{1/4} \\ \tau & \text{else} \end{cases} \tag{B.23}$$

Appendix C

Some Properties of the Bar Potential

In this appendix, we list some relations and some numerical values for the bar potential (formulae (3.4) and (3.5)) defined in section 3.1. Since our usual model parameter is the OLR radius, we express all other quantities through this. For the following define $\Omega_0 := \omega(R_0) = v_0/R_0$.

$$R_{\text{CR}} = R_{\text{OLR}} \left(1 + \sqrt{\frac{1+\beta}{2}}\right)^{\frac{-1}{1-\beta}} \tag{C.1}$$

$$R_{\text{ILR}} = R_{\text{CR}} \left(1 - \sqrt{\frac{1+\beta}{2}}\right)^{\frac{1}{1-\beta}} \tag{C.2}$$

$$\frac{\Omega_b}{\Omega_0} = \left(\frac{R_0}{R_{\text{CR}}}\right)^{1-\beta} = \left(1 + \sqrt{\frac{1+\beta}{2}}\right) \left(\frac{R_0}{R_{\text{OLR}}}\right)^{1-\beta} \tag{C.3}$$

Regarding the axisymmetric background alone, we can give epicycle frequency κ and axis ratio γ (cf. section 2.2.1), and the formal Oort constants A, B as in (2.24) and (2.25):

$$\kappa(R) = \sqrt{2(1+\beta)}\,\omega(R), \tag{C.4}$$

$$\gamma = \sqrt{\frac{2}{1+\beta}}, \tag{C.5}$$

$$A = \tfrac{1}{2}(1-\beta)\,\omega(R), \tag{C.6}$$

$$B = -\tfrac{1}{2}(1+\beta)\,\omega(R), \tag{C.7}$$

The radius R_E of circular orbits of energy E, which we need for the sampling, is determined via $E = \frac{1}{2}v_c^2(R_E) + \Phi(R_E)$, giving

$$R_E = \begin{cases} R_0 \left(\frac{2\beta E}{(1+\beta)v_0^2}\right)^{\frac{1}{2\beta}} & (\beta \neq 0) \\ R_0 \; e^{E/v_0^2 - \frac{1}{2}} & (\beta = 0) \end{cases} \tag{C.8}$$

The corresponding circular angular momentum $L_c(R_E) = R_E v_c(R_E)$ is

$$L_c(R_E) = \begin{cases} R_0 v_0 \left(\frac{2\beta E}{(1+\beta)v_0^2}\right)^{\frac{1+\beta}{2\beta}} & (\beta \neq 0) \\ R_0 v_0 \; e^{E/v_0^2 - \frac{1}{2}} & (\beta = 0) \end{cases} \tag{C.9}$$

For the numerics, we fix our system of units by setting $R_0 = 1$ and $v_0 = 1$. For the IAU recommended values $R_0 = 8.5$ kpc and $v_0 = 220$ km/s this implies that our unit of time is 37.8 Myr and our unit of angular velocities, like Ω_P or the Oort constants, is 25.88 km/s/kpc.

In the bar potential (3.5), we usually choose $R_b = 0.8 R_{\rm CR}$. Some numerical fix points of the effective potential (2.8) arising from this are listed in Table C.1 for our favorite choices of $R_{\rm OLR}$. Note the substantial spans between the L1 and L4 radii.

	$\beta = 0$		$\beta = 0.1$		$\beta = -0.1$	
$R_{\rm OLR}$	0.92	0.8	0.92	0.8	0.92	0.8
$R_{\rm CR}$	0.538924	0.468629	0.496663	0.431881	0.576932	0.50168
$R_{\rm ILR}$	0.157847	0.137258	0.110412	0.096011	0.2101	0.182696
Ω_P	1.85555	2.13388	1.87735	2.12898	1.83132	2.13565
for $R_b = 0.8 R_{\rm CR}$, $\alpha = 0.01$:						
R_b	0.431139	0.374903	0.39733	0.345505	0.461545	0.401344
$R_{\rm L4}$	0.338705	0.265997	0.271794	0.208608	0.4003	0.320437
$R_{\rm L1}$	0.635357	0.577576	0.61569	0.564951	0.65584	0.591277
$\Phi_{\rm eff}$(L4)	-0.649918	-0.446123	4.6157	4.99445	-5.81655	-5.74335
$\Phi_{\rm eff}$(L1)	-1.27848	-1.48142	3.72694	3.55219	-6.27957	-6.51261
for $R_b = 0.7 R_{\rm CR}$, $\alpha = 0.01$:						
R_b	0.377246	0.32804	0.347664	0.302317	0.403852	0.351176
$R_{\rm L4}$	0.276842	0.214385	0.216102	0.163722	0.335145	0.264435
$R_{\rm L1}$	0.635357	0.577576	0.61569	0.564951	0.65584	0.591277
$\Phi_{\rm eff}$(L4)	-0.419873	-0.0196512	4.99412	5.64215	-5.68734	-5.47262
$\Phi_{\rm eff}$(L1)	-1.27848	-1.48142	3.72694	3.55219	-6.27957	-6.51261
for $R_b = 0.9 R_{\rm CR}$, $\alpha = 0.01$:						
R_b	0.485031	0.421766	0.446997	0.388693	0.519239	0.451512
$R_{\rm L4}$	0.393325	0.31413	0.324317	0.252993	0.454348	0.369746
$R_{\rm L1}$	0.635357	0.577576	0.61569	0.564951	0.65584	0.591277
$\Phi_{\rm eff}$(L4)	-0.770978	-0.677596	4.4103	4.63199	-5.884	-5.88721
$\Phi_{\rm eff}$(L1)	-1.27848	-1.48142	3.72694	3.55219	-6.27957	-6.51261
for $R_b = 0.8 R_{\rm CR}$, $\alpha = 0.02$:						
R_b	0.431139	0.374903	0.39733	0.345505	0.461545	0.401344
$R_{\rm L4}$	0.284943	0.22101	0.22321	0.169354	0.343888	0.271784
$R_{\rm L1}$	0.685896	0.629223	0.670794	0.620605	0.70183	0.638782
$\Phi_{\rm eff}$(L4)	0.028357	0.6504	5.55374	6.48276	-5.3126	-4.91444
$\Phi_{\rm eff}$(L1)	-1.39353	-1.63228	3.60243	3.39322	-6.38571	-6.65521

Table C.1: Important numerical values of our barred potentials. For the definition of the various parameters cf. eqns. (3.3) to (3.5), α is the strength parameter of eqn. (3.7). The values of $\Phi_{\rm eff}$ and R at the Lagrange points L1 and L4 fix Figure 2.3 quantitatively.

Appendix D

Coordinate Systems and the Galaxy

A lot of trouble arises from the fact that the Milky Way is rotating in the mathematically negative sense. This came about by calling the Galactic pole on the northern hemisphere of the sky the north Galactic pole. When using local coordinate systems, especially in velocity space, this usually results in either accepting a left-handed coordinate system, or having one axis reversed from its natural direction. Needless to say that different authors usually choose different conventions. The long-term remedy would be to swap the naming of the Galactic poles.

Nearly all authors cling to the convention of measuring the tangential velocities $v_\varphi = v$ in the direction of Galactic rotation. One has the choice then, of putting the axis of radial velocity $v_R = u$ in the direction towards the Galactic center (i.e. $u = -dR/dt$), or leaving it to the outside, but having the axis of vertical velocity $v_z = w$ point towards negative z or having a left-handed coordinate system. Since we are usually not concerned about the third dimension, this last choice makes no difference to us. There is, however, one more choice to be made, regarding the Galactic azimuth angle. Whereas it seems natural to put its zero along the long axis of the bar, its direction can be with or against Galactic rotation.

We consider the following coordinate choices:

a) u-axis towards the Galactic center, azimuth φ in mathematical sense, but against Galactic rotation. The supposed position of the Sun of lagging behind the Galactic bar by about 30° then simply means $\varphi = 30^\circ$.

b) u-axis towards the Galactic center, azimuth φ against mathematical sense in direction of Galactic rotation. The supposed position of the Sun then corresponds to $\varphi = 150^\circ$.

c) u-axis towards Galactic anti-center, azimuth φ in mathematical sense.

d) u-axis towards Galactic anti-center, azimuth φ against mathematical sense.

Our favorite choice will be a), as already taken in Dehnen & Binney 1998 [31].

Note that in cases a) and c), angular momenta and angular velocities associated with Galactic rotation (such as $\omega(R)$ or Ω_b) should carry a negative sign. Conversely, in cases b) and d) the connection between co-rotating and inertial system azimuthal angles is $\varphi = \varphi_I + \Omega t$ instead of $\varphi = \varphi_I - \Omega t$.

Appendix E

Calculation of the Oort Constants

Given the local mean radial and tangential components $\bar{u}$ and $\bar{v}$ of the stellar velocity distribution in the Galactic disk as well as their derivatives w.r.t. R and φ, we want to calculate the Oort constants corresponding to that distribution. Apart from the change in the velocities themselves, we have to account for the shifts in the orientation of the coordinate axes at nearby points.

If $\mathbf{e}_x, \mathbf{e}_y$ denote unit vectors in the radial and tangential direction respectively, the relative velocity field $\mathbf{w}(R, \varphi; R_0, \varphi_0)$ as in eqn. (2.20) for an LSR at (R_0, φ_0) is

$$\begin{aligned}
&\mathbf{w}(R,\varphi;R_0,\varphi_0) = \\
&= \bar{u}(R,\varphi)\,\mathbf{e}_x(R,\varphi) + \bar{v}(R,\varphi)\,\mathbf{e}_y(R,\varphi) - \\
&\quad [\bar{u}(R_0,\varphi_0)\,\mathbf{e}_x(R_0,\varphi_0) + \bar{v}(R_0,\varphi_0)\,\mathbf{e}_y(R_0,\varphi_0)] \\
&= [\bar{u}(R,\varphi) - \bar{u}(R_0,\varphi_0)]\,\mathbf{e}_x(R,\varphi) + \\
&\quad \bar{u}(R_0,\varphi_0)\,[\mathbf{e}_x(R,\varphi) - \mathbf{e}_x(R_0,\varphi_0)] + \\
&\quad [\bar{v}(R,\varphi) - \bar{v}(R_0,\varphi_0)]\,\mathbf{e}_y(R,\varphi) + \\
&\quad \bar{v}(R_0,\varphi_0)\,[\mathbf{e}_y(R,\varphi) - \mathbf{e}_y(R_0,\varphi_0)]
\end{aligned} \tag{E.1}$$

Whereas we can easily set

$$[\bar{u}(R,\varphi) - \bar{u}(R_0,\varphi_0)] \approx \Delta R\,\left.\frac{\partial \bar{u}}{\partial R}\right|_{(R_0,\varphi_0)} + \Delta\varphi\,\left.\frac{\partial \bar{u}}{\partial \varphi}\right|_{(R_0,\varphi_0)}, \tag{E.2}$$

and similarly for $\bar{v}$, we have to be more careful with the basis vectors, since now we have to deal with the question of the coordinate system orientation, cf. appendix D. For the moment, we leave this choice open and take care of different coordinate systems by including sign variables $s_i = \pm 1$. So we can write:

$$[\mathbf{e}_x(R,\varphi) - \mathbf{e}_x(R_0,\varphi_0)] \approx s_1 \mathbf{e}_y(R_0,\varphi_0)\,\Delta\varphi \tag{E.3}$$

$$[\mathbf{e}_y(R,\varphi) - \mathbf{e}_y(R_0,\varphi_0)] \approx s_2 \mathbf{e}_x(R_0,\varphi_0)\,\Delta\varphi \tag{E.4}$$

$$x = s_3 \Delta R \tag{E.5}$$

$$y = s_4 R\,\Delta\varphi \tag{E.6}$$

Working out the geometry, we get the signs given in Table E.1 for the coordinate systems considered in appendix D.

	s_1	s_2	s_3	s_4
a)	$+$	$-$	$-$	$-$
b)	$-$	$+$	$-$	$+$
c)	$-$	$+$	$+$	$-$
d)	$+$	$-$	$+$	$+$

Table E.1: Sign variables for the coordinate systems considered in appendix D

Using this, we get

$$\begin{aligned}
&\mathbf{w}(R,\varphi;R_0,\varphi_0) = \\
&= \left[s_3 x\frac{\partial\bar{u}}{\partial R} + s_4 y\frac{1}{R}\frac{\partial\bar{u}}{\partial\varphi}\right]\mathbf{e}_x(R_0,\varphi_0) + s_1 s_4 y\frac{\bar{u}}{R}\mathbf{e}_y(R_0,\varphi_0) + \\
&\quad \left[s_3 x\frac{\partial\bar{v}}{\partial R} + s_4 y\frac{1}{R}\frac{\partial\bar{v}}{\partial\varphi}\right]\mathbf{e}_y(R_0,\varphi_0) + s_2 s_4 y\frac{\bar{v}}{R}\mathbf{e}_x(R_0,\varphi_0) = \\
&= \begin{pmatrix} s_3\dfrac{\partial\bar{u}}{\partial R} & s_4\dfrac{1}{R}\dfrac{\partial\bar{u}}{\partial\varphi} + s_2 s_4\dfrac{\bar{v}}{R} \\ s_3\dfrac{\partial\bar{v}}{\partial R} & s_4\dfrac{1}{R}\dfrac{\partial\bar{v}}{\partial\varphi} + s_1 s_4\dfrac{\bar{u}}{R} \end{pmatrix}\begin{pmatrix} x \\ y \end{pmatrix}
\end{aligned} \tag{E.7}$$

Comparing with eqn. (2.20) and solving, we obtain

$$a = \frac{1}{2}\left(s_2 s_4\frac{\bar{v}}{R} + s_3\frac{\partial\bar{v}}{\partial R} + s_4\frac{1}{R}\frac{\partial\bar{u}}{\partial\varphi}\right) \tag{E.8}$$

$$b = \frac{1}{2}\left(-s_2 s_4\frac{\bar{v}}{R} + s_3\frac{\partial\bar{v}}{\partial R} - s_4\frac{1}{R}\frac{\partial\bar{u}}{\partial\varphi}\right) \tag{E.9}$$

$$c = \frac{1}{2}\left(-s_1 s_4\frac{\bar{u}}{R} + s_3\frac{\partial\bar{u}}{\partial R} - s_4\frac{1}{R}\frac{\partial\bar{v}}{\partial\varphi}\right) \tag{E.10}$$

$$k = \frac{1}{2}\left(s_1 s_4\frac{\bar{u}}{R} + s_3\frac{\partial\bar{u}}{\partial R} + s_4\frac{1}{R}\frac{\partial\bar{v}}{\partial\varphi}\right) \tag{E.11}$$

For a circular velocity field, there is no radial velocity component $\bar{u}$ and no φ-dependence, so $k = c = 0$ and[1] a and b reduce to the forms of A and B in eqn. (2.24) and (2.25), at least for coordinate conventions a) and b). Note however, that A and B involve the circular velocity v_c, whereas a and b contain the true mean velocity $\bar{v}$, so there is still a difference because of the asymmetric drift.

---

[1] More precisely, whenever either one of $\bar{u} \equiv 0$ or $\partial/\partial\varphi \equiv 0$ holds, then a and b reduce to this forms already. If we have both $\bar{u} \equiv 0$ and $\partial/\partial\varphi \equiv 0$, then in addition $k = c = 0$. However, for a stationary velocity field, both conditions can only occur in conjunction.

Appendix F

Detailed Calculation of the Axis Ratio

Most derivations of the Oort relation, i.e. the equality of $\sigma_{vv}^2/\sigma_{uu}^2$ and $-B/(A-B)$, are obscured by implicit assumptions of axisymmetry, as in Binney & Tremaine 1987 [11] (section 4.2.1 (c)). So the actual prerequisites for this equality are not really clear. For this reason, we will start from scratch here, and carefully take note of every assumption we have to make.

The collisionless Boltzmann equation in cylindrical coordinates reads as follows

$$\begin{aligned}&\frac{\partial f}{\partial t} + v_R\frac{\partial f}{\partial R} + \frac{v_\varphi}{R}\frac{\partial f}{\partial \varphi} + v_z\frac{\partial f}{\partial z} + \\ &\quad + \left(\frac{v_\varphi^2}{R} - \frac{\partial \Phi}{\partial R}\right)\frac{\partial f}{\partial v_R} - \frac{1}{R}\left(v_R v_\varphi + \frac{\partial \Phi}{\partial \varphi}\right)\frac{\partial f}{\partial v_\varphi} - \frac{\partial \Phi}{\partial z}\frac{\partial f}{\partial v_z} = 0\end{aligned} \tag{F.1}$$

The Jeans equations are the zeroth and first velocity moments of this, so we have to integrate over all velocity coordinates, after having multiplied with v_R, v_φ or v_z as appropriate. This gives

$$\frac{\partial \rho}{\partial t} + \frac{1}{R}\frac{\partial (R\rho\bar{v}_R)}{\partial R} + \frac{1}{R}\frac{\partial (\rho\bar{v}_\varphi)}{\partial \varphi} + \frac{\partial (\rho\bar{v}_z)}{\partial z} = 0 \tag{F.2}$$

$$\frac{\partial (\rho\bar{v}_R)}{\partial t} + \frac{\partial (\rho\,\overline{v_R^2})}{\partial R} + \frac{1}{R}\frac{\partial (\rho\,\overline{v_R v_\varphi})}{\partial \varphi} + \frac{\partial (\rho\,\overline{v_R v_z})}{\partial z} + \rho\left(\frac{\overline{v_R^2} - \overline{v_\varphi^2}}{R} + \frac{\partial \Phi}{\partial R}\right) = 0 \tag{F.3}$$

$$\frac{\partial (\rho\bar{v}_\varphi)}{\partial t} + \frac{\partial (\rho\,\overline{v_R v_\varphi})}{\partial R} + \frac{1}{R}\frac{\partial (\rho\,\overline{v_\varphi^2})}{\partial \varphi} + \frac{\partial (\rho\,\overline{v_\varphi v_z})}{\partial z} + \frac{\rho}{R}\left(2\,\overline{v_R v_\varphi} + \frac{\partial \Phi}{\partial \varphi}\right) = 0 \tag{F.4}$$

$$\frac{\partial (\rho\bar{v}_z)}{\partial t} + \frac{\partial (\rho\,\overline{v_R v_z})}{\partial R} + \frac{1}{R}\frac{\partial (\rho\,\overline{v_\varphi v_z})}{\partial \varphi} + \frac{\partial (\rho\,\overline{v_z^2})}{\partial z} + \frac{\rho}{R}\,\overline{v_R v_z} + \rho\frac{\partial \Phi}{\partial z} = 0 \tag{F.5}$$

In the same manner, we take the $v_R v_\varphi$ moment:

$$\begin{aligned}&\frac{\partial (\rho\,\overline{v_R v_\varphi})}{\partial t} + \frac{\partial (\rho\,\overline{v_R^2 v_\varphi})}{\partial R} + \frac{1}{R}\frac{\partial (\rho\,\overline{v_R v_\varphi^2})}{\partial \varphi} + \frac{\partial (\rho\,\overline{v_R v_\varphi v_z})}{\partial z} + \\ &\qquad + \frac{\rho}{R}\left(2\,\overline{v_R^2 v_\varphi} - \overline{v_\varphi^3}\right) + \rho\left(\bar{v}_\varphi\frac{\partial \Phi}{\partial R} + \frac{\bar{v}_R}{R}\frac{\partial \Phi}{\partial \varphi}\right) = 0\end{aligned} \tag{F.6}$$

Now we regard a stationary disk, so we have no time dependencies. Eliminating the potential terms in (F.6) with the help of (F.3) and (F.4), we get

$$\frac{\partial (\rho\,\overline{v_R^2 v_\varphi})}{\partial R} + \frac{1}{R}\frac{\partial (\rho\,\overline{v_R v_\varphi^2})}{\partial \varphi} + \frac{\partial (\rho\,\overline{v_R v_\varphi v_z})}{\partial z}$$

$$
\begin{aligned}
&- \bar{v}_\varphi \frac{\partial(\rho\,\overline{v_R^2})}{\partial R} - \frac{1}{R}\bar{v}_\varphi \frac{\partial(\rho\,\overline{v_R v_\varphi})}{\partial \varphi} - \bar{v}_\varphi \frac{\partial(\rho\,\overline{v_R v_z})}{\partial z} \\
&- \bar{v}_R \frac{\partial(\rho\,\overline{v_R v_\varphi})}{\partial R} - \frac{1}{R}\bar{v}_R \frac{\partial(\rho\,\overline{v_\varphi^2})}{\partial \varphi} - \bar{v}_R \frac{\partial(\rho\,\overline{v_\varphi v_z})}{\partial z} \\
&+ \frac{\rho}{R}\left(2\,\overline{v_R^2 v_\varphi} - \overline{v_\varphi^3} - \overline{v_R^2}\bar{v}_\varphi + \overline{v_\varphi^2}\bar{v}_\varphi - 2\bar{v}_R\overline{v_R v_\varphi}\right) = 0 \qquad \text{(F.7)}
\end{aligned}
$$

If we restrict ourselves to the $z = 0$ plane and assume that our distribution function is symmetric about this plane, the z-derivatives have to vanish by symmetry, so we just leave these away. It is useful to rewrite the resulting equation in terms of the more familiar dispersion components (from now on, also write $\bar{u}$, $\bar{v}$ instead of $\bar{v}_R$ and $\bar{v}_\varphi$):

$$
\begin{aligned}
\sigma_{RR}^2 &= \overline{(v_R - \bar{u})^2} = \overline{v_R^2} - \bar{u}^2 && \text{(F.8)} \\
\sigma_{\varphi\varphi}^2 &= \overline{(v_\varphi - \bar{v})^2} = \overline{v_\varphi^2} - \bar{v}^2 && \text{(F.9)} \\
\sigma_{R\varphi}^2 &= \overline{(v_R - \bar{u})(v_\varphi - \bar{v})} = \overline{v_R v_\varphi} - \bar{u}\bar{v} && \text{(F.10)}
\end{aligned}
$$

We also define the third moment quantities

$$
\begin{aligned}
\Delta_{\varphi\varphi\varphi} = \overline{(v_\varphi - \bar{v})^3} &= \overline{v_\varphi^3} - 3\,\overline{v_\varphi^2}\,\bar{v} + 2\bar{v}^3 \\
&= \overline{v_\varphi^3} - 3\sigma_{\varphi\varphi}^2\bar{v} - \bar{v}^3 && \text{(F.11)} \\
\Delta_{R\varphi\varphi} = \overline{(v_R - \bar{u})(v_\varphi - \bar{v})^2} &= \overline{v_R v_\varphi^2} - 2\,\overline{v_R v_\varphi}\,\bar{v} - \overline{v_\varphi^2}\bar{u} + 2\bar{u}\bar{v}^2 \\
&= \overline{v_R v_\varphi^2} - 2\sigma_{R\varphi}^2\bar{v} - \sigma_{\varphi\varphi}^2\bar{u} - \bar{u}\bar{v}^2 && \text{(F.12)} \\
\Delta_{RR\varphi} = \overline{(v_R - \bar{u})^2(v_\varphi - \bar{v})} &= \overline{v_R^2 v_\varphi} - 2\,\overline{v_R v_\varphi}\,\bar{u} - \overline{v_R^2}\bar{v} + 2\bar{u}^2\bar{v} \\
&= \overline{v_R^2 v_\varphi} - 2\sigma_{R\varphi}^2\bar{u} - \sigma_{RR}^2\bar{v} - \bar{u}^2\bar{v} && \text{(F.13)}
\end{aligned}
$$

which are presumably small. Then eqn. (F.7) can be written as

$$
\begin{aligned}
\frac{\sigma_{\varphi\varphi}^2}{\sigma_{RR}^2} &= \frac{1}{2} + \frac{R}{2\bar{v}}\frac{\partial \bar{v}}{\partial R} - \frac{\Delta_{\varphi\varphi\varphi}}{2\bar{v}\sigma_{RR}^2} + \frac{\Delta_{RR\varphi}}{\bar{v}\sigma_{RR}^2} + \frac{\Delta_{RR\varphi}}{2\bar{v}\sigma_{RR}^2}\frac{R}{\rho}\frac{\partial\rho}{\partial R} + \frac{R}{2\bar{v}\sigma_{RR}^2}\frac{\partial\Delta_{RR\varphi}}{\partial R} + \\
&+ \frac{1}{2\bar{v}\sigma_{RR}^2}\left(\frac{\partial\Delta_{R\varphi\varphi}}{\partial\varphi} + \bar{v}\frac{\partial\sigma_{R\varphi}^2}{\partial\varphi} + \sigma_{\varphi\varphi}^2\frac{\partial\bar{u}}{\partial\varphi} + \right. \\
&\left. + 2\sigma_{R\varphi}^2\frac{\partial\bar{v}}{\partial\varphi} + \bar{u}\bar{v}\frac{\partial\bar{v}}{\partial\varphi} + \frac{\Delta_{R\varphi\varphi}}{\rho}\frac{\partial\rho}{\partial\varphi}\right) \qquad \text{(F.14)}
\end{aligned}
$$

Probably, some of the terms can be neglected for small non-axisymmetries, possibly all the φ-derivatives.

There is an additional correction arising from the vertex deviation if we take the axis ratio to be the one relating to the principal directions of the ellipsoid. The squares of the axes in these directions are

$$
\begin{aligned}
\sigma_1^2 &= \frac{\sigma_{RR}^2 + \sigma_{\varphi\varphi}^2}{2} + \frac{1}{2}\sqrt{(\sigma_{RR}^2 - \sigma_{\varphi\varphi}^2)^2 + (\sigma_{R\varphi}^2)^2} \\
&\approx \sigma_{RR}^2 + \frac{(\sigma_{R\varphi}^2)^2}{4(\sigma_{RR}^2 - \sigma_{\varphi\varphi}^2)} && \text{(F.15)} \\
\sigma_2^2 &= \frac{\sigma_{RR}^2 + \sigma_{\varphi\varphi}^2}{2} - \frac{1}{2}\sqrt{(\sigma_{RR}^2 - \sigma_{\varphi\varphi}^2)^2 + (\sigma_{R\varphi}^2)^2} \\
&\approx \sigma_{\varphi\varphi}^2 - \frac{(\sigma_{R\varphi}^2)^2}{4(\sigma_{RR}^2 - \sigma_{\varphi\varphi}^2)}, && \text{(F.16)}
\end{aligned}
$$

so we have a correction

$$\frac{\sigma_2^2}{\sigma_1^2} \approx \frac{\sigma_{\varphi\varphi}^2}{\sigma_{RR}^2} - \left(\frac{\sigma_{R\varphi}^2}{2\sigma_{RR}^2}\right)^2, \tag{F.17}$$

but it is only second order in the small quantity $\sigma_{R\varphi}^2$.

If we now assume axisymmetry, which in particular implies that

- there is no φ-dependence: $\partial/\partial\varphi\,(...) = 0$,
- there can be no mean radial velocities: $\bar{u} = 0$,
- there can be no vertex deviation, i.e. $\sigma_{R\varphi} = 0$

then we are left with the following (we can collect all the terms involving $\Delta_{RR\varphi}$ into a single derivative):

$$\frac{\sigma_{\varphi\varphi}^2}{\sigma_{RR}^2} = \frac{1}{2} + \frac{R}{2\bar{v}}\frac{\partial\bar{v}}{\partial R} - \frac{\Delta_{\varphi\varphi\varphi}}{2\bar{v}\sigma_{RR}^2} + \frac{1}{2\rho R\bar{v}\sigma_{RR}^2}\frac{\partial}{\partial R}(R^2\rho\Delta_{RR\varphi}) \tag{F.18}$$

This is to be compared with the Oort constant expression which in the axisymmetric case reduces to (cf. eqn. (E.8) and (E.9))

$$\frac{-b}{a-b} = \frac{1}{2} + \frac{R}{2\bar{v}}\frac{\partial\bar{v}}{\partial R} \tag{F.19}$$

We see that even in the axisymmetric case, we have the additional terms involving $\Delta_{\varphi\varphi\varphi}$ and $\Delta_{RR\varphi}$, which are measures of the asymmetry of the distribution in $v_\varphi - \bar{v}$ and v_R. One might have thought that at least $\Delta_{RR\varphi}$ would also need to vanish for symmetry reasons[1]. A sufficient condition for this would be that the distribution function in the axisymmetric case $f(R, v_R, v_\varphi)$ would factorize:

$$f(R, v_R, v_\varphi) = f_R(R, v_R) f_\varphi(R, v_\varphi), \tag{F.20}$$

and for many models in the literature this is indeed the case. Then all composite averages would factorize too: $\overline{v_R^2 v_\varphi} = \overline{v_R^2}\bar{v}_\varphi$, $\overline{v_R v_\varphi^2} = \bar{v}_R\overline{v_\varphi^2}$ and $\overline{v_R v_\varphi} = \bar{v}_R\bar{v}_\varphi$. This would imply that $\Delta_{RR\varphi} = \Delta_{R\varphi\varphi} = 0$. However, (F.20) is not really required by axisymmetry, and indeed, for our model distribution function (3.1) it is not true. What is required, however, is that

$$f(R, v_R, v_\varphi) = f(R, -v_R, v_\varphi) \tag{F.21}$$

This can be seen as follows: according to the Jeans theorem, the distribution function of a stationary system can only be a function of its integrals of motion. In our two-dimensional case we have a complete set of integrals, consisting of energy E and angular momentum L. Now $E = \frac{1}{2}(v_R^2 + v_\varphi^2) + \Phi(R)$ does not know about the sign of v_R, and $L = Rv_\varphi$ does not involve v_R anyway. As a consequence of (F.21), we have that every average involving an odd power of v_R will vanish:

$$\overline{...\,v_R^n} = 0 \quad \text{for } n \text{ odd} \tag{F.22}$$

and therefore $\bar{u} = \bar{v}_R = 0$, $\sigma_{R\varphi}^2 = 0$ and $\Delta_{R\varphi\varphi} = 0$, but not $\Delta_{RR\varphi}$ or $\Delta_{\varphi\varphi\varphi}$. The significance of the $\Delta_{RR\varphi}$- and $\Delta_{\varphi\varphi\varphi}$-terms is already discussed by Cuddeford & Binney 1994 [20], where also formula (F.18) for the axisymmetric case is given.

---

[1] This is expressed in the left part of eqn. (4-48a) of Binney & Tremaine 1987 [11], but is not correct.

Appendix G

Calculating Spiral Structure

The potential (5.2) of the spiral structure (5.4)[1] reads

$$\begin{aligned}\sqrt{R}\Phi \;=\; & -G\int_{-\infty}^{\infty} du' \int_{0}^{2\pi} d\varphi' K(u-u',\varphi-\varphi') \times \\ & e^{3u'/2}\delta_{\text{spir}}\Sigma_0 e^{-R(u')/R_\Sigma} f\left(R(u')\right) \Re\left\{e^{i(ku'+m\varphi')}\right\} \\ = & -\frac{G\delta_{\text{spir}}\Sigma_0}{\sqrt{2}} \Re\left\{\int_{-\infty}^{\infty} du' e^{3u'/2} e^{-R(u')/R_\Sigma} f(R(u')) e^{iku'} \times \right. \\ & \left. \int_{0}^{2\pi} d\varphi' \frac{e^{im\varphi'}}{\sqrt{\cosh(u-u')-\cos(\varphi-\varphi')}}\right\},\end{aligned} \tag{G.1}$$

where $R(u) = e^{u}$. For the following, define

$$F(u) := e^{3u/2} e^{-R(u)/R_\Sigma} f\left(R(u)\right) \tag{G.2}$$

as an abbreviation. By substituting $\varphi'' = \varphi' - \varphi$ and $u'' = u' - u$, and by noting that the kernel $K(u, \varphi)$ is symmetric in u, we get

$$\begin{aligned}\sqrt{R}\Phi \;=\; & -\frac{G\delta_{\text{spir}}\Sigma_0}{\sqrt{2}} \Re\left\{e^{im\varphi}\int_{-\infty}^{\infty} du'' F(u+u'') e^{ik(u+u'')} \times \right. \\ & \left. \int_{0}^{2\pi} d\varphi'' \frac{e^{im\varphi''}}{\sqrt{\cosh(u'')-\cos(\varphi'')}}\right\} \\ = & -\frac{G\delta_{\text{spir}}\Sigma_0}{\sqrt{2}} \Re\left\{e^{im\varphi}\int_{0}^{\infty} du'' \times \right. \\ & \left[F(u+u'')e^{ik(u+u'')} + F(u-u'')e^{ik(u-u'')}\right] \times \\ & \left. \int_{0}^{2\pi} d\varphi'' \frac{e^{im\varphi''}}{\sqrt{\cosh(u'')-\cos(\varphi'')}}\right\} \\ = & -\frac{G\delta_{\text{spir}}\Sigma_0}{\sqrt{2}} \Re\left\{e^{im\varphi}\int_{0}^{\infty} du'' \times \right. \\ & \left.\left[F(u+u'')e^{ik(u+u'')} + F(u-u'')e^{ik(u-u'')}\right]\right\} \times \\ & \int_{0}^{2\pi} d\varphi'' \frac{\cos(m\varphi'')}{\sqrt{\cosh(u'')-\cos(\varphi'')}},\end{aligned} \tag{G.3}$$

---

[1] In this appendix φ is taken along the direction of Galactic rotation, unlike our usual convention (convention a) in appendix D). Therefore, the sign in eqn. 5.4 has to be changed to $\ldots + m\varphi$.

where the last equality follows because the imaginary part of the φ''-integral vanishes for symmetry reasons.

The integral over φ'' can be expressed in terms of elliptic integrals ($C := \cosh(u'') \geq 1$):

$$\int_0^{2\pi} d\varphi'' \frac{\cos(m\varphi'')}{\sqrt{C - \cos(\varphi'')}} =$$

$$\text{for } m = 2\text{:} = -\frac{4}{3\sqrt{C-1}} \times \left(4C(C-1)E\left(\frac{-2}{C-1}\right) - (4C^2-1)K\left(\frac{-2}{C-1}\right)\right) \tag{G.4}$$

$$\text{for } m = 3\text{:} = -\frac{4}{15\sqrt{C-1}} \left((32C^2-9)(C-1)E\left(\frac{-2}{C-1}\right) + + (32C^2-17)CK\left(\frac{-2}{C-1}\right)\right) \tag{G.5}$$

$$\text{for } m = 4\text{:} = -\frac{4}{105\sqrt{C-1}} \left(16C(C-1)(24C^2-13)E\left(\frac{-2}{C-1}\right) - - (384C^4 - 304C^2 + 25)K\left(\frac{-2}{C-1}\right)\right) \tag{G.6}$$

Here, K and E denote some slight generalization of the complete elliptic integrals of the first and second kind. They are defined in the follwing way

$$K(x) = \int_0^{\pi/2} \frac{d\theta}{\sqrt{1 - x\sin^2\theta}}, \tag{G.7}$$

$$E(x) = \int_0^{\pi/2} \sqrt{1 - x\sin^2\theta}\, d\theta, \tag{G.8}$$

which differs from the common definition of these functions by the substitution $k^2 \to x$ to allow for negative values of x as needed here. However, they are accessible through the same kind of numerics (see e.g. Press et al. 2002 [78]).

Regarding this integral as a function of u, which we will denote by $A_m(u)$, we see that it has a logarithmic singularity at $u = 0$. Using this, and additionally defining

$$I_1(u) := \int_0^\infty du' \left\{F(u+u')\cos k(u+u') + F(u-u')\cos k(u-u')\right\} A_m(u') \tag{G.9}$$

$$I_2(u) := \int_0^\infty du' \left\{F(u+u')\sin k(u+u') + F(u-u')\sin k(u-u')\right\} A_m(u') \tag{G.10}$$

$$I_3(u) := \int_0^\infty du' \left\{F'(u+u')\cos k(u+u') + F'(u-u')\cos k(u-u')\right\} A_m(u') \tag{G.11}$$

$$I_4(u) := \int_0^\infty du' \left\{F'(u+u')\sin k(u+u') + F'(u-u')\sin k(u-u')\right\} A_m(u') \tag{G.12}$$

$$I_5(u) := \int_0^\infty du' \left\{F''(u+u')\cos k(u+u') + F''(u-u')\cos k(u-u')\right\} A_m(u') \tag{G.13}$$

$$I_6(u) := \int_0^\infty du' \left\{F''(u+u')\sin k(u+u') + F''(u-u')\sin k(u-u')\right\} A_m(u') \tag{G.14}$$

where all derivatives of $F(u)$ are with respect to its argument, we can finally write for the potential and its first and second derivatives:

$$\Phi(R,\varphi) = -\frac{G\delta_{\text{spir}}\Sigma_0}{\sqrt{2R}} \left\{\cos(m\varphi) I_1(u(R)) - \sin(m\varphi) I_2(u(R))\right\} \tag{G.15}$$

$$\begin{aligned}\frac{\partial\Phi}{\partial R} = &-\frac{1}{2R}\Phi(R,\varphi) + \\ &+ \frac{G\delta_{\text{spir}}\Sigma_0}{\sqrt{2R}} \left\{ \frac{k}{R}\left[\cos(m\varphi) I_2(u(R)) + \sin(m\varphi) I_1(u(R))\right] + \right. \\ &\qquad \left. + \frac{1}{R}\left[\cos(m\varphi) I_3(u(R)) + \sin(m\varphi) I_4(u(R))\right] \right\}\end{aligned} \tag{G.16}$$

$$\frac{\partial\Phi}{\partial\varphi} = m\frac{G\delta_{\text{spir}}\Sigma_0}{\sqrt{2R}} \left\{\sin(m\varphi) I_1(u(R)) + \cos(m\varphi) I_2(u(R))\right\} \tag{G.17}$$

$$\begin{aligned}\frac{\partial^2\Phi}{\partial R^2} = &\left(\frac{1}{2R^2} - \frac{k^2}{R^2}\right)\Phi(R,\varphi) - \frac{1}{2R}\frac{\partial\Phi}{\partial R} + \\ &+ \frac{G\delta_{\text{spir}}\Sigma_0}{\sqrt{2R}} \left\{ -\frac{3k}{2R^2}\left[\cos(m\varphi) I_2(u(R)) + \sin(m\varphi) I_1(u(R))\right] \right. \\ &\qquad - \frac{3}{2R^2}\left[\cos(m\varphi) I_3(u(R)) + \sin(m\varphi) I_4(u(R))\right] \\ &\qquad + \frac{k-1}{R^2}\left[\cos(m\varphi) I_4(u(R)) + \sin(m\varphi) I_3(u(R))\right] \\ &\qquad \left. + \frac{1}{R^2}\left[\cos(m\varphi) I_5(u(R)) + \sin(m\varphi) I_6(u(R))\right] \right\}\end{aligned} \tag{G.18}$$

$$\begin{aligned}\frac{\partial^2\Phi}{\partial R\partial\varphi} = &-\frac{1}{2R}\frac{\partial\Phi}{\partial R} - \frac{mk}{R}\Phi(R,\varphi) + \\ &+ \frac{m}{R}\frac{G\delta_{\text{spir}}\Sigma_0}{\sqrt{2R}} \left\{-\sin(m\varphi) I_3(u(R)) + \cos(m\varphi) I_4(u(R))\right\}\end{aligned} \tag{G.19}$$

$$\frac{\partial^2\Phi}{\partial\varphi^2} = -m^2\Phi(R,\varphi) \tag{G.20}$$

The actual handling of the potential is such that we calculate the integrals $I_1, \ldots, I_6$ by numerical integration beforehand, and tabulate them. Values of the potential and its derivatives during the simulation are then obtained from formulae (G.15) - (G.20).

Appendix H

Transformation between Galactocentric and Heliocentric Velocity Components

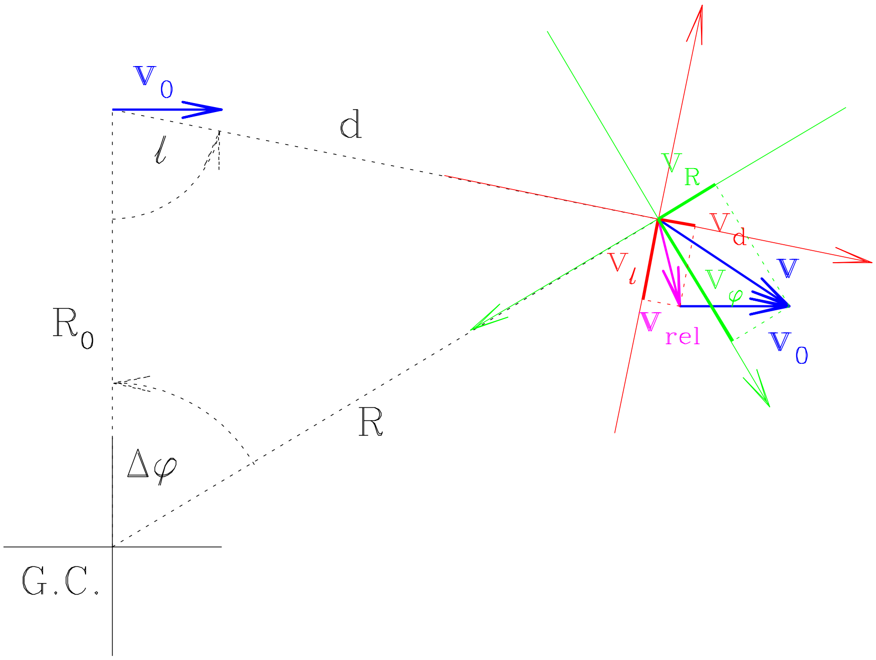

Figure H.1: Geometry of the transformation problem from heliocentric, relative velocity components (v_d, v_ℓ) as measured by astrometric missions to Galactocentric velocity components (v_R, v_φ) at rest.

Our numerical model used Galactocentric velocity components v_R, v_φ (see appendix D for the sign convention problems associated with this). On various occasions, we need to transform these into the velocity components that the obervers know, relative to a supposed position of the Sun (R_0, φ_0). These are heliocentric components, namely the line-of-sight velocity v_d and the proper motion of the star on the sky. Since we always restrict ourselves to the Galactic plane, the latter corresponds to only one velocity component which we will call v_ℓ.

The geometry of the problem is shown in Fig. H.1. We regard the components v_d and v_ℓ of the relative velocity $\mathbf{v}_{\rm rel} = \mathbf{v} - \mathbf{v}_0$ to relate to the LSR, so the motion of the Sun reltive to the LSR is either neglected or already corrected out. From geometry, we note some useful identities:

$$R^2 = R_0^2 + d^2 - 2R_0 d \cos \ell, \tag{H.1}$$

$$\sin \Delta\varphi = \frac{d}{R} \sin \ell \tag{H.2}$$

$$\tan \ell = \frac{R \sin \Delta\varphi}{R_0 - R \cos \Delta\varphi} \tag{H.3}$$

$$R_0 - R \cos \Delta\varphi = d \cos \ell \tag{H.4}$$

Writing $\mathbf{v} = v_R \mathbf{e}_R(\mathbf{r}) + v_\varphi \mathbf{e}_\varphi(\mathbf{r})$, $\mathbf{v}_0 = v_R \mathbf{e}_\varphi(\mathbf{r}_0)$ and $\mathbf{v}_{\text{rel}} = v_d \mathbf{e}_d + v_\ell \mathbf{e}_\ell$ with appropriate unit vectors (pointing in the directions of the coordinate axes in Fig. H.1 respectively), we can solve for v_R and v_φ by projection. For the arising scalar products, we find by evaluating them in some coordinate system:

$$\mathbf{e}_d \cdot \mathbf{e}_R(\mathbf{r}) = -\frac{R - R_0 \cos \Delta\varphi}{d} \tag{H.5}$$

$$\mathbf{e}_d \cdot \mathbf{e}_\varphi(\mathbf{r}) = \frac{R_0}{d} \sin \Delta\varphi \tag{H.6}$$

$$\mathbf{e}_d \cdot \mathbf{e}_\varphi(\mathbf{r}_0) = \frac{R}{d} \sin \Delta\varphi \tag{H.7}$$

$$\mathbf{e}_\ell \cdot \mathbf{e}_R(\mathbf{r}) = -\frac{R_0}{d} \sin \Delta\varphi \tag{H.8}$$

$$\mathbf{e}_\ell \cdot \mathbf{e}_\varphi(\mathbf{r}) = -\frac{R - R_0 \cos \Delta\varphi}{d} \tag{H.9}$$

$$\mathbf{e}_\ell \cdot \mathbf{e}_\varphi(\mathbf{r}_0) = -\frac{R \cos \Delta\varphi - R_0}{d} \tag{H.10}$$

$$\mathbf{e}_R(\mathbf{r}) \cdot \mathbf{e}_\varphi(\mathbf{r}_0) = -\sin \Delta\varphi \tag{H.11}$$

$$\mathbf{e}_\varphi(\mathbf{r}) \cdot \mathbf{e}_\varphi(\mathbf{r}_0) = \cos \Delta\varphi \tag{H.12}$$

Hence, we find a conversion formula as follows:

$$\begin{aligned} \begin{pmatrix} v_d \\ v_\ell \end{pmatrix} &= -\frac{R}{d} \begin{pmatrix} v_R \\ v_\varphi \end{pmatrix} - \frac{R_0}{d} \begin{pmatrix} 0 \\ v_0 \end{pmatrix} \\ &\quad + \frac{R_0}{d} \begin{pmatrix} \cos \Delta\varphi & -\sin \Delta\varphi \\ \sin \Delta\varphi & \cos \Delta\varphi \end{pmatrix} \begin{pmatrix} v_R \\ v_\varphi \end{pmatrix} \\ &\quad + \frac{R}{d} \begin{pmatrix} \cos \Delta\varphi & \sin \Delta\varphi \\ -\sin \Delta\varphi & \cos \Delta\varphi \end{pmatrix} \begin{pmatrix} 0 \\ v_0 \end{pmatrix} \end{aligned} \tag{H.13}$$

For the inverse conversion, we obtain

$$\begin{pmatrix} v_R \\ v_\varphi \end{pmatrix} = -\frac{R}{d} \begin{pmatrix} v_d \\ v_\ell \end{pmatrix} + \begin{pmatrix} \cos \Delta\varphi & -\sin \Delta\varphi \\ \sin \Delta\varphi & \cos \Delta\varphi \end{pmatrix} \begin{pmatrix} \frac{R_0}{d} v_d \\ v_0 + \frac{R_0}{d} v_\ell \end{pmatrix}, \tag{H.14}$$

Bibliography

[1] L. H. Amaral and J. R. D. Lepine. A self-consistent model of the spiral structure of the Galaxy. *MNRAS*, 286:885–894, April 1997.

[2] E. Athanassoula. The spiral structure of galaxies. *Physics Reports*, 114:321–403, 1984.

[3] E. Athanassoula. What determines the strength and the slowdown rate of bars? *MNRAS*, 341:1179–1198, June 2003.

[4] E. Athanassoula and L. Martinet. A correlation between the lengths of bars and the sizes of bulges. *A&A*, 87:L10+, July 1980.

[5] G. Bertin and C. C. Lin. *Spiral structure in galaxies a density wave theory*. Spiral structure in galaxies a density wave theory, Publisher: Cambridge, MA MIT Press, 1996 Physical description x, 271 p. ISBN0262023962, 1996.

[6] J. Binney. Secular Evolution of the Galactic Disk. In *ASP Conf. Ser. 230: Galaxy Disks and Disk Galaxies*, pages 63–3, 2001.

[7] J. Binney, W. Dehnen, and G. Bertelli. The age of the solar neighbourhood. *MNRAS*, 318:658–664, November 2000.

[8] J. Binney, O. E. Gerhard, A. A. Stark, J. Bally, and K. I. Uchida. Understanding the kinematics of Galactic centre gas. *MNRAS*, 252:210–218, September 1991.

[9] J. Binney, J. Kormendy, and S. D. M. White, editors. *Morphology and dynamics of galaxies*, 1982.

[10] J. Binney and M. Merrifield. *Galactic astronomy*. Galactic astronomy / James Binney and Michael Merrifield. Princeton, NJ : Princeton University Press, 1998. (Princeton series in astrophysics) QB857 .B522 1998 ($35.00), 1998.

[11] J. Binney and S. Tremaine. *Galactic dynamics*. Princeton, NJ, Princeton University Press, 1987, 747 p., 1987.

[12] L. Blitz and D. N. Spergel. Direct evidence for a bar at the galactic center. *ApJ*, 379:631, 1991.

[13] L. Blitz and D. N. Spergel. The shape of the galaxy. *ApJ*, 370:205, 1991.

[14] R. Bottema. The Stellar Kinematics of Galactic Disks. *A&A*, 275:16–+, August 1993.

[15] R. G. Carlberg and J. A. Sellwood. Dynamical evolution in galactic disks. *ApJ*, 292:79–89, May 1985.

[16] J. L. Caswell and R. F. Haynes. Southern H II regions - an extensive study of radio recombination line emission. *A&A*, 171:261–276, January 1987.

[17] A. A. Cole and M. D. Weinberg. An Upper Limit to the Age of the Galactic Bar. *ApJ*, 574:L43–L46, July 2002.

[18] G. Contopoulos. How far do bars extend? *A&A*, 81:198–209, January 1980.

[19] G. Contopoulos and P. Grosbol. Orbits in barred galaxies. *Astron. Astrophys. Rev.*, 1:261–289, November 1989.

[20] P. Cuddeford and J. Binney. Modified Moments and the Oort Constants. *MNRAS*, 266:273–+, January 1994.

[21] T. M. Dame, D. Hartmann, and P. Thaddeus. The Milky Way in Molecular Clouds: A New Complete CO Survey. *ApJ*, 547:792–813, February 2001.

[22] G. de Vaucouleur. In *The Galaxy and the Magellanic Clouds*, IAU Symp. 20, pages 195+, 1964.

[23] V. P. Debattista, O. Gerhard, and M. N. Sevenster. The pattern speed of the OH/IR stars in the Milky Way. *MNRAS*, 334:355–368, August 2002.

[24] V. P. Debattista and J. A. Sellwood. Dynamical Friction and the Distribution of Dark Matter in Barred Galaxies. *ApJ*, 493:L5+, January 1998.

[25] W. Dehnen. The Distribution of Nearby Stars in Velocity Space Inferred from HIPPARCOS Data. *AJ*, 115:2384–2396, June 1998.

[26] W. Dehnen. Simple Distribution Functions for Stellar Disks. *AJ*, 118:1201–1208, September 1999.

[27] W. Dehnen. The Pattern Speed of the Galactic Bar. *ApJ*, 524:L35–L38, October 1999.

[28] W. Dehnen. The Effect of the Outer Lindblad Resonance of the Galactic Bar on the Local Stellar Velocity Distribution. *AJ*, 119:800–812, February 2000.

[29] W. Dehnen. Our Galaxy. In *Disks of Galaxies: Kinematics, Dynamics and Perurbations, ASP Conference Proceedings, Vol. 275. Edited by E. Athanassoula, A. Bosma, and R. Mujica. ISBN: 1-58381-117-6. San Francisco: Astronomical Society of the Pacific, 2002, pp. 105-116*, pages 105–116, December 2002.

[30] W. Dehnen and J. Binney. Dynamical Models of the Milky Way. In *ASP Conf. Ser. 92: Formation of the Galactic Halo...Inside and Out*, pages 393–+, April 1996.

[31] W. Dehnen and J. Binney. Local stellar kinematics from HIPPARCOS data. *MNRAS*, 298:387–394, August 1998.

[32] D. Downes, T. L. Wilson, J. Bieging, and J. Wink. H110-alpha and H2CO survey of galactic radio sources. *A&AS*, 40:379–394, June 1980.

[33] R. Drimmel. Evidence for a two-armed spiral in the Milky Way. *A&A*, 358:L13–L16, June 2000.

[34] R. Drimmel and D. N. Spergel. Three-dimensional Structure of the Milky Way Disk: The Distribution of Stars and Dust beyond $0.35R_{solar}$. *ApJ*, 556:181–202, July 2001.

[35] E. Dwek, R. G. Arendt, M. G. Hauser, T. Kelsall, C. M. Lisse, S. H. Moseley, R. F. Silverberg, T. J. Sodroski, and J. L. Weiland. Morphology, near-infrared luminosity, and mass of the Galactic bulge from COBE DIRBE observations. *ApJ*, 445:716–730, June 1995.

[36] O. J. Eggen. Star Streams and Galactic Structure. *AJ*, 112:1595–+, October 1996.

[37] O. J. Eggen. The Stellar Content of Star Stream I. *AJ*, 111:1615–+, April 1996.

[38] D. M. Elmegreen, F. R. Chromey, B. A. Bissell, and K. Corrado. K'-Band Observations of Underlying Symmetric Structure in Flocculent Galaxies. *AJ*, 118:2618–2624, December 1999.

[39] D. M. Elmegreen and B. G. Elmegreen. Blue and near-infrared surface photometry of spiral structure in 34 nonbarred grand design and flocculent galaxies. *ApJS*, 54:127–149, January 1984.

[40] P. Englmaier and O. Gerhard. Gas dynamics and large-scale morphology of the Milky Way galaxy. *MNRAS*, 304:512–534, April 1999.

[41] N. W. Evans and J. L. Collett. Simple discs with flat roatation curves. *MNRAS*, 264:353–374, September 1993.

[42] M. Feast and P. Whitelock. Galactic kinematics of Cepheids from HIPPARCOS proper motions. *MNRAS*, 291:683–+, November 1997.

[43] K. C. Freeman. On the Disks of Spiral and S0 Galaxies. *ApJ*, 160:811–+, June 1970.

[44] H. T. Freudenreich. A COBE Model of the Galactic Bar and Disk. *ApJ*, 492:495+, January 1998.

[45] B. Fuchs, C. Dettbarn, H. Jahreiß, and R. Wielen. The Evolution of the Milky Way Monitored in the Solar Neighbourhood. In *ASP Conf. Ser. 228: Dynamics of Star Clusters and the Milky Way*, pages 235–+, 2001.

[46] R. Fux. Order and chaos in the local disc stellar kinematics induced by the Galactic bar. *A&A*, 373:511–535, July 2001.

[47] Y. M. Georgelin and Y. P. Georgelin. The spiral structure of our Galaxy determined from H II regions. *A&A*, 49:57–79, May 1976.

[48] J. Gerssen, K. Kuijken, and M. R. Merrifield. The shape of the velocity ellipsoid in NGC 488. *MNRAS*, 288:618–622, July 1997.

[49] J. Gerssen, K. Kuijken, and M. R. Merrifield. Model independent measurements of bar pattern speeds. *American Astronomical Society Meeting*, 201:0–+, December 2002.

[50] G. Gilmore and N. Reid. New light on faint stars. III - Galactic structure towards the South Pole and the Galactic thick disc. *MNRAS*, 202:1025–1047, March 1983.

[51] A. Gould. Stellar Halo Parameters from 4588 Subdwarfs. *ApJ*, 583:765–775, February 2003.

[52] H. J. Habing. IRAS edge-on view of our Galaxy - The disk. *A&A*, 200:40–50, July 1988.

[53] D. Hartmann and W. B. Burton. *Atlas of galactic neutral hydrogen*. Cambridge; New York: Cambridge University Press, ISBN 0521471117, 1997.

[54] A. J. Kalnajs. Dynamics of Flat Galaxies. I. *ApJ*, 166:275+, June 1971.

[55] F. J. Kerr and D. Lynden-Bell. Review of galactic constants. *MNRAS*, 221:1023–1038, August 1986.

[56] T. Kranz, A. Slyz, and H. Rix. Probing for Dark Matter within Spiral Galaxy Disks. *ApJ*, 562:164–178, November 2001.

[57] T. Kranz, A. Slyz, and H. Rix. Dark Matter within High Surface Brightness Spiral Galaxies. *ApJ*, 586:143–151, March 2003.

[58] Th. Kranz. *Dark matter in spiral galaxies.* PhD thesis, Max-Planck-Institut für Astronomie, Heidelberg, 2002.

[59] K. Kuijken. Is There a Bulge Distinct from the Bar? In *IAU Symp. 169: Unsolved Problems of the Milky Way*, volume 169, pages 71–+, 1996.

[60] K. Kuijken and S. Tremaine. Large-scale Oscillations of the Galaxy and the Kinematics of the Solar Neighbourhood. In *Dynamics of Disc Galaxies*, pages 71+, 1991.

[61] K. Kuijken and S. Tremaine. On the ellipticity of the Galactic disk. *ApJ*, 421:178–194, January 1994.

[62] C. G. Lacey. The influence of massive gas clouds on stellar velocity dispersions in galactic discs. *MNRAS*, 208:687–707, June 1984.

[63] J. R. Lewis. Faint stars and Oort's constants. *MNRAS*, 244:247–253, May 1990.

[64] C. C. Lin and F. H. Shu. On the Spiral Structure of Disk Galaxies. *ApJ*, 140:646–+, August 1964.

[65] C. C. Lin and F. H. Shu. On the Spiral Structure of Disk Galaxies, II. Outline of a Theory of Density Waves. *Proceedings of the National Academy of Science*, 55:229–234, February 1966.

[66] G. Mühlbauer and W. Dehnen. Kinematic response of the outer stellar disk to a central bar. *A&A*, 401:975–984, April 2003.

[67] M. R. Metzger and P. L. Schechter. Whither the LSR: Anticenter carbon star velocities. *ApJ*, 420:177–182, January 1994.

[68] F. Mignard. Local galactic kinematics from Hipparcos proper motions. *A&A*, 354:522–536, February 2000.

[69] Y. N. Mishurov and I. A. Zenina. Yes, the Sun is located near the corotation circle. *A&A*, 341:81–85, January 1999.

[70] D. K. Ojha. Radial scalelengths of the galactic thin and thick disc with 2MASS data. *MNRAS*, 322:426–432, April 2001.

[71] R. P. Olling and W.. Dehnen. The Oort constants measured from proper motions. *ApJ*, submitted.

[72] J. H. Oort. Investigations concerning the rotational motion of the galactic system together with new determinations of secular parallaxes, precession and motion of the equinox (Errata: 4 94). *Bull. Astron. Inst. Neth.*, 4:79–+, September 1927.

[73] J. H. Oort. Observational evidence confirming Lindblad's hypothesis of a rotation of the galactic system. *Bull. Astron. Inst. Neth.*, 3:275–+, April 1927.

[74] B. Paczynski, K. Z. Stanek, A. Udalski, M. Szymanski, J. Kaluzny, M. Kubiak, M. Mateo, and W. Krzeminski. Are the OGLE microlenses in the galactic bar? *ApJ*, 435:L113–LL116, November 1994.

[75] M. A. C. Perryman, K. S. de Boer, G. Gilmore, E. Høg, M. G. Lattanzi, L. Lindegren, X. Luri, F. Mignard, O. Pace, and P. T. de Zeeuw. GAIA: Composition, formation and evolution of the Galaxy. *A&A*, 369:339–363, April 2001.

[76] W. L. Peters. Models for the inner regions of the Galaxy. I. *ApJ*, 195:617–629, February 1975.

[77] D. Pfenniger. Stability of the Lagrangian points in stellar bars. *A&A*, 230:55–66, April 1990.

[78] W. H. Press, S. A. Teukolsky, W. T. Vetterling, and B. P. Flannery. *Numerical Recipes in C++*. Cambridge University Press, Cambridge, 2002.

[79] M. Preto and S. Tremaine. A Class of Symplectic Integrators with Adaptive Time Step for Separable Hamiltonian Systems. *AJ*, 118:2532–2541, November 1999.

[80] A. C. Quillen. Prospecting for Spiral Structure in the Flocculent Outer Milky Way Disk with Color-Magnitude Star Counts from the Two Micron All Sky Survey. *AJ*, 124:924–930, August 2002.

[81] A. C. Quillen. Chaos Caused by Resonance Overlap in the Solar Neighborhood: Spiral Structure at the Bar's Outer Lindblad Resonance. *AJ*, 125:785–793, February 2003.

[82] D. Raboud, M. Grenon, L. Martinet, R. Fux, and S. Udry. Evidence for a signature of the galactic bar in the solar neighbourhood. *A&A*, 335:L61–L64, July 1998.

[83] M. J. Reid, K. M. Menten, R. Genzel, T. Ott, R. Schödel, and A. Eckart. The Position of Sagittarius A*. II. Accurate Positions and Proper Motions of Stellar SiO Masers near the Galactic Center. *ApJ*, 587:208–220, April 2003.

[84] H. Rix and D. Zaritsky. Nonaxisymmetric Structures in the Stellar Disks of Galaxies. *ApJ*, 447:82+, July 1995.

[85] K. Schwarzschild. *Göttinger Nachr.*, page 614, 1907.

[86] M. S. Seigar and P. A. James. The structure of spiral galaxies - II. Near-infrared properties of spiral arms. *MNRAS*, 299:685–698, September 1998.

[87] J. A. Sellwood and A. Wilkinson. Dynamics of barred galaxies. *Reports of Progress in Physics*, 56:173–256, February 1993.

[88] N. J. Shaviv. The spiral structure of the Milky Way, cosmic rays, and ice age epochs on Earth. *New Astronomy*, 8:39–77, January 2003.

[89] L. J. Spitzer and M. Schwarzschild. The Possible Influence of Interstellar Clouds on Stellar Velocities. II. *ApJ*, 118:106–+, July 1953.

[90] K. Z. Stanek, A. Udalski, M. Szymanski, J. Kaluzny, M. Kubiak, M. Mateo, and W. Krzeminski. Modeling the Galactic Bar Using Red Clump Giants. *ApJ*, 477:163+, March 1997.

[91] M. Steinmetz and the RAVE science working group. RAVE - The Radial Velocity Experiment. 2002. Available at http://www.aip.de/RAVE/.

[92] J. H. Taylor and J. M. Cordes. Pulsar distances and the galactic distribution of free electrons. *ApJ*, 411:674–684, July 1993.

[93] J. P. Vallée. Metastudy of the Spiral Structure of Our Home Galaxy. *ApJ*, 566:261–266, February 2002.

[94] P. C. van der Kruit and L. Searle. Surface photometry of edge-on spiral galaxies. I - A model for the three-dimensional distribution of light in galactic disks. II - The distribution of light and colour in the disk and spheroid of NGC 891. *A&A*, 95:105–126, February 1981.

[95] P. C. van der Kruit and L. Searle. Surface photometry of edge-on spiral galaxies. III - Properties of the three-dimensional distribution of light and mass in disks of spiral galaxies. *A&A*, 110:61–78, June 1982.

[96] M. D. Weinberg. Detection of a large-scale stellar bar in the milky way. *ApJ*, 384:81–94, 1992.

[97] R. Wielen. The diffusion of stellar orbits derived from the observed age-dependence of the velocity dispersion. *A&A*, 60:263–275, September 1977.

[98] H. Zhao, D. N. Spergel, and R. M. Rich. Microlensing by the galactic bar. *ApJ*, 440:L13–LL16, February 1995.

Danksagung

Ich danke ...

zuerst dem ursprünglichen Betreuer meiner Arbeit, Dr. Walter Dehnen, für seinen Ideenreichtum, seine Geduld und die ständige Bereitschaft, mit mir den Fortgang der Arbeit zu diskutieren. Nicht zuletzt danke ich ihm für die Überlassung einer großen Menge exzellent geschriebenen C++-Codes, der als Starthilfe für meine Simulationen diente.

Prof. Dr. Hans-Walter Rix für seine Bereitschaft, mich als Doktorand zu übernehmen und nach dem Fortgang von Dr. Dehnen meine Betreuung in weiten Teilen selbst zu tragen. Seine Fähigkeit komplexe Sachverhalte in klarer Sprache darzustellen habe ich stets bewundert. Ich danke ihm insbesondere auch dafür, mir überhaupt die Möglichkeit gegeben zu haben, am MPIA zu promovieren.

Prof. Dr. Roland Wielen für seine Bereitschaft, diese Arbeit zu begutachten.

Helmut, Bernd, Angela, Markus, Michael, Markus, Roland, Sadegh, Steffi, Thorsten für das soziale Element am Nachmittag; Robert für erhellende Gespräche über Gott und die Welt.

vielen weiteren Angehörigen des Instituts für interessante wissenschaftliche Diskussionen.

den Mitarbeitern der EDV-Abteilung des Institutes, besonders den Herren Ulrich Hiller und Frank Richter, die mich stets untestützt haben, wenn ich mit großen oder kleinen Problemen zu ihnen kam. Ebenso Herrn Walter Rauh für das offene Ohr in Hardware-Angelegenheiten.

meinen Zimmergenossen für die stete Bereitschaft, meine Probleme während ihrer Arbeitszeit zu diskutieren.

der übrigen Schöpfung für all den Fisch.

Großer Dank gilt auch meinen Eltern, deren Unterstützung und Wohlwollen mich durch diese Doktorarbeit in gleicher Weise begleitet haben wie schon durch mein Studium; ebenso meiner Tante Berta Benner, die sich die akademischen Weihen ihres Neffen zu erleben gewünscht hätte.

Und ganz besonderen Dank schulde ich ... – Anca.